

# LINK<sub>pipe</sub> Theory Manual



*<http://www.linkftr.com>*

*Revision: v3.0.1, August 2012*

# Preface

Welcome to the LINK<sub>pipe</sub> theory manual.

Contact LINK<sub>ftr</sub> AS:

Visitor address:	LINKftr AS Richard Birkelands vei 2B Trondheim
Mail address:	LINKftr AS Richard Birkelands vei 2B 7465 Trondheim Norway
Voice:	+47 922 73 033
E-mail:	Vidar Osen: <i>Vidar.Osen@linkftr.com</i> Dag Olav Kjellemo: <i>Dag-Olav.Kjellemo@linkftr.com</i> Christian Thaulow: <i>Christian.Thaulow@sintef.no</i> Bjørn Skallerud: <i>Bjorn.Skallerud@ntnu.no</i> Kjell Holthe: <i>Kjell.Holthe@ntnu.no</i> Support: <i>support@linkftr.com</i>
Web:	<a href="http://www.linkftr.com">http://www.linkftr.com</a>

# Contents

<b>1</b>	<b>Introduction</b>	<b>1</b>
<b>2</b>	<b>Finite elements</b>	<b>3</b>
2.1	Line-spring finite element . . . . .	3
2.1.1	Introduction . . . . .	3
2.1.1.1	Generalised displacements and interpolation functions . . .	4
2.1.1.2	Generalised forces . . . . .	4
2.1.1.3	Generalised forces and nodal forces . . . . .	5
2.1.2	Linear elastic line-spring . . . . .	5
2.1.3	Elastic-plastic line-spring . . . . .	9
2.1.4	Non linear kinematic hardening . . . . .	11
2.1.5	Contact formulation - crack closure . . . . .	16
2.1.6	Ductile crack growth . . . . .	17
2.1.7	Fatigue tearing . . . . .	17
2.1.8	Two-parameter fracture assessment . . . . .	18
2.1.9	Circumferential crack growth . . . . .	20
2.1.10	Residual stress . . . . .	22
2.1.10.1	Implementation of relaxation of residual stress . . . . .	22
2.1.11	Different materials . . . . .	23
2.1.12	Split line-spring - another mismatch approach . . . . .	24
2.1.13	Embedded defects . . . . .	26
2.2	Shell finite element . . . . .	27
2.2.1	Linear shell finite element . . . . .	27
2.2.1.1	The membrane element . . . . .	27
2.2.1.2	The bending element . . . . .	28
2.2.2	Co-rotated shell element . . . . .	29
2.2.2.1	Equilibrium and tangent stiffness . . . . .	32
2.2.3	Plasticity modelling for shell element . . . . .	35
2.2.3.1	Stress resultant plasticity . . . . .	35
2.2.3.2	Through the thickness integration . . . . .	37
2.2.3.3	Stress update and isotropic strain hardening . . . . .	39
2.2.3.4	Non linear kinematic hardening . . . . .	40
2.2.3.5	Different material properties through the thickness . . . . .	41
2.3	Beam finite element . . . . .	45
<b>3</b>	<b>Solution algorithm</b>	<b>48</b>
3.1	Introduction . . . . .	48
3.2	A load increment . . . . .	48
3.3	Equilibrium iterations . . . . .	49

---

3.4	How to avoid large load increments . . . . .	49
<b>4</b>	<b>Linear dependencies</b>	<b>52</b>
4.1	Rotations . . . . .	52
4.2	Translations . . . . .	53
<b>A</b>	<b>Connection between co-rotational degree of freedom and global degree of freedom</b>	<b>54</b>
<b>B</b>	<b>Consistent geometrical tangent stiffness contributions</b>	<b>56</b>

# Chapter 1

## Introduction

Surface cracked shell structures occur in many industrial applications, e.g. pressure vessels, pipelines, tubular frame structures. Two main facts cause the occurrence of defects: the shell segments that the structure are fabricated from are usually joined with welds, and most structures are subjected some cyclic loading that promote fatigue crack growth. Although welding procedures have improved significantly over the years, some initial defects have to be expected and accounted for. In some applications the structure is subjected to very high loads.

Traditional design rules for defect assessment often state that no defect can be accepted at all under loading conditions causing significant inelasticity. Hence, more advanced numerical assessment is the only way out of this dilemma.

Traditionally, three-dimensional solid finite elements are employed in discretising the shell structure in order to account for the crack. Fig. 1.1 illustrates a typical mesh. This puts high demands on both pre- and post-processing in addition to long CPU times. An alternative is to use shell finite elements. Then the challenge is to account for the crack. This may be done using line-spring finite elements at the crack location. Fig. 1.1 also illustrate such a mesh. For the meshes shown, a typical solid finite element mesh will have some 30000 degrees of freedom (utilising two symmetry planes), whereas the shell model will have some 1000 degrees of freedom (using symmetry). A factor of 10 in reduced CPU is typical. But the main benefit of using shell/line-spring elements is the reduced time spent in pre- and post-processing.

Using line-spring finite elements, the crack is modelled as nonlinear springs between the shell elements, with a varying compliance as a function of crack depth and plastic deformations. The accuracy of the predicted fracture mechanics quantities such as crack tip opening displacement (CTOD) and J-integral is crucial for such an approach. The line-spring element has a long history (see e.g. Rice and Levy [36], Rice [35], Parks and White [49] and Skallerud [42]), and is implemented in some commercial codes. However, some limitations still exist, e.g. how to treat short cracks and large deformations. Short cracks are the most relevant in practical situations, that is cracks of depths less than about 25% of the shell thickness. In many applications there also is a need to account for large displacements and rotations, and simultaneously assess the criticality of the defect. In the present study these aspects are accounted for and implemented in a new commercial code denoted LINK. It is a general nonlinear shell finite element program accounting for large rigid body motion and plasticity. The shell element is a rectangular ANDES element in a co-rotated formulation

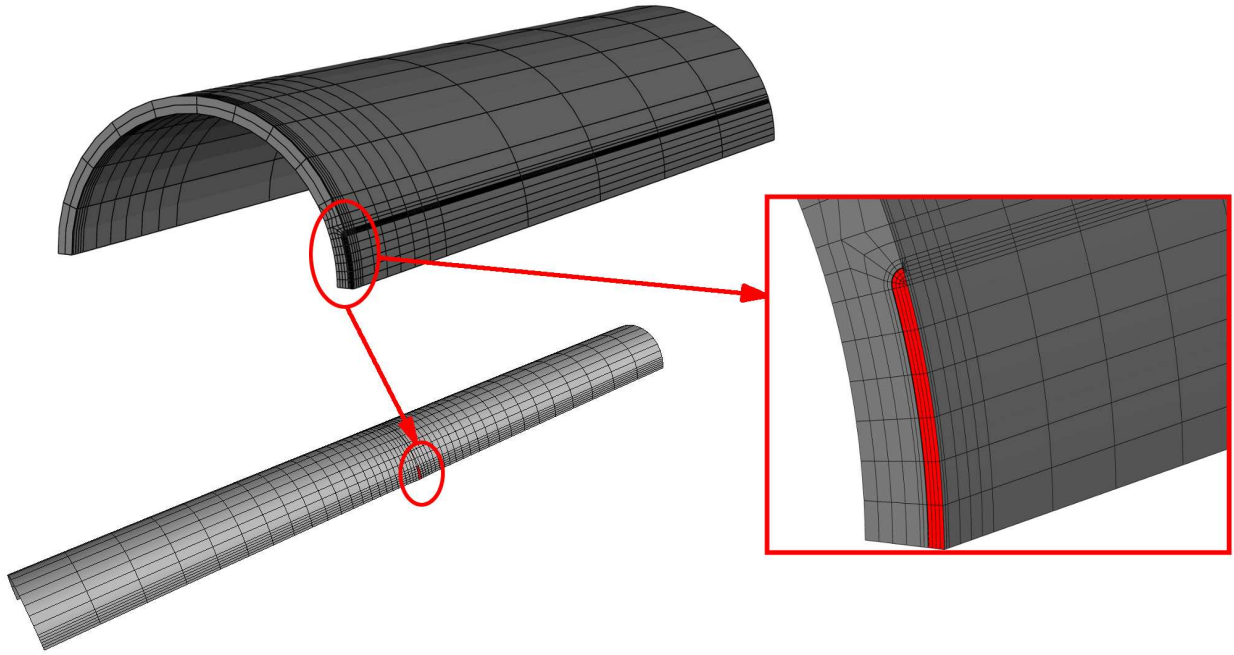


Figure 1.1: Solid and shell/line-spring modelling of surface cracked shells

(see Haugen [17] and Skallerud and Haugen [43]). The local strains are assumed small. Within this formulation an improved line-spring finite element is implemented. With this, one has a tool that can account for cracks and global/local buckling in the same simulation. One important industrial case where this is relevant is in laying of pipelines by means of reeling, with nominal strains that reach about 2% (both in tension and compression).

# Chapter 2

## Finite elements

### 2.1 Line-spring finite element

#### 2.1.1 Introduction

The part-through surface crack is originally a three dimensional problem. The three dimensional problem is formulated within the context of two-dimensional plate or shell theory with the part-cracked section represented as a line-spring finite element. The line-springs take into account the additional flexibility due to the surface crack. The line-spring element can be schematically represented by two straight lines connected to each other by a series of springs. At zero deformation the lines lie upon each other. When a Mode I (crack opening) deformation takes place each line displaces in opposite direction. The displacement and rotation are constrained by the springs. As the shell element used herein is 4-node, the line-spring element is 4-noded with linear interpolation polynomials. A 2-point Gauss integration is employed. Hence, the line-spring element has 8 degrees of freedom (four in-plane displacements and four rotations with axis along the element), see Fig. 2.1.

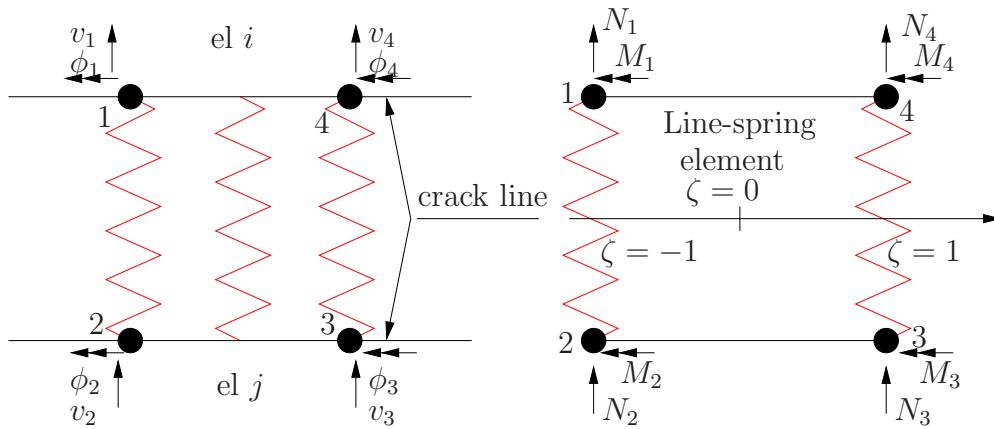


Figure 2.1: Line-spring element

### 2.1.1.1 Generalised displacements and interpolation functions

Gauss quadrature is chosen as numerical interpolation between nodal displacements/forces and generalised displacements/forces. Linear interpolation functions are used where the integration points are located at the following positions according to Fig. 2.1:

$$\zeta_A = -\frac{1}{\sqrt{3}} \quad , \quad \zeta_B = \frac{1}{\sqrt{3}} \quad (2.1)$$

The generalised displacements in the line-spring element at  $\zeta = \mp 1$  respectively are expressed as

$$\mathbf{q}_A = \begin{bmatrix} \delta_A \\ \theta_A \end{bmatrix} \quad , \quad \mathbf{q}_B = \begin{bmatrix} \delta_B \\ \theta_B \end{bmatrix} \quad (2.2)$$

and the relation between the nodal displacements  $(v_i, \phi_i)$  and the generalised displacements reads

$$\delta^* = \mathbf{N}^* v_e \quad (2.3)$$

where

$$\delta^* = \begin{bmatrix} \delta_A \\ \theta_A \\ \delta_B \\ \theta_B \end{bmatrix} \quad \mathbf{N}^* = \begin{bmatrix} 1 & 0 & -1 & 0 & 0 & 0 & 0 & 0 \\ 0 & 1 & 0 & -1 & 0 & 0 & 0 & 0 \\ 0 & 0 & 0 & 0 & -1 & 0 & 1 & 0 \\ 0 & 0 & 0 & 0 & 0 & -1 & 0 & 1 \end{bmatrix} \quad v_e = \begin{bmatrix} v_1 \\ \phi_1 \\ v_2 \\ \phi_2 \\ v_3 \\ \phi_3 \\ v_4 \\ \phi_4 \end{bmatrix} \quad (2.4)$$

The generalised displacements at an arbitrary point  $|\zeta| \leq 1$  is expressed as

$$\mathbf{q} = \mathbf{N} \delta^* \quad (2.5)$$

where

$$\mathbf{q} = \begin{bmatrix} \delta(\zeta) \\ \theta(\zeta) \end{bmatrix} \quad \mathbf{N} = \begin{bmatrix} \hat{N}_1 & 0 & \hat{N}_2 & 0 \\ 0 & \hat{N}_1 & 0 & \hat{N}_2 \end{bmatrix} \quad \delta^* = \begin{bmatrix} \delta_A \\ \theta_A \\ \delta_B \\ \theta_B \end{bmatrix} \quad (2.6)$$

The quantities  $\hat{N}_1$  and  $\hat{N}_2$  are expressed as

$$\hat{N}_1 = \frac{1 - \zeta}{2} \quad \hat{N}_2 = \frac{1 + \zeta}{2} \quad (2.7)$$

### 2.1.1.2 Generalised forces

The generalised forces (or internal forces) in the line-spring element is computed from the generalised displacements,  $\mathbf{q}$  at a generic point  $|\zeta| \leq 1$  as

$$\mathbf{Q} = \mathbf{D} \mathbf{q} \quad (2.8)$$

where  $\mathbf{D}$  is the stiffness matrix of the line-spring element. Inserting Eq. 2.3 and Eq. 2.5 into Eq. 2.8 gives the following relation for the generalised forces in the line-spring element:

$$\mathbf{Q} = \mathbf{D} \mathbf{N} \mathbf{N}^* v_e \quad (2.9)$$

The matrix multiplication  $\mathbf{N} \mathbf{N}^*$  equals  $\mathbf{N}^{**} = ([\mathbf{N}], -[\mathbf{N}])$ .



### 2.1.1.3 Generalised forces and nodal forces

The nodal forces from the line-spring element is computed from the generalised forces. The nodal forces can be expressed as

$$\begin{bmatrix} N_1 \\ M_1 \\ N_4 \\ M_4 \end{bmatrix} = - \begin{bmatrix} N_2 \\ M_2 \\ N_3 \\ M_3 \end{bmatrix} = \int_{LS} \begin{bmatrix} \hat{N}_1 & 0 \\ 0 & \hat{N}_1 \\ \hat{N}_2 & 0 \\ 0 & \hat{N}_2 \end{bmatrix} \begin{bmatrix} N \\ M \end{bmatrix} ds \quad (2.10)$$

where  $[N, M]^T$  are the generalised forces,  $\mathbf{Q}$ . The total nodal force vector from the line-spring element is then expressed as  $\mathbf{F}_e = [N_1, M_1, N_2, M_2, N_3, M_3, N_4, M_4]^T$ . Matrix multiplication expression reads

$$\mathbf{F}_e = \int_{LS} \begin{bmatrix} [\mathbf{N}^T] \\ -[\mathbf{N}^T] \end{bmatrix} \begin{bmatrix} N \\ M \end{bmatrix} ds \quad (2.11)$$

Substituting Eq. 2.9 into Eq. 2.11 gives

$$\mathbf{F}_e = \int_{LS} \mathbf{N}^{**T} \mathbf{D} \mathbf{N}^{**} ds v_e \quad (2.12)$$

### 2.1.2 Linear elastic line-spring

In the elastic domain, the work conjugates (generalised displacements and generalised forces) are connected through the elastic compliance matrix as

$$\mathbf{q} = \mathbf{C} \mathbf{Q} \quad (2.13)$$

where  $\mathbf{C}$  is the elastic compliance matrix:

$$\mathbf{C} = \begin{bmatrix} C_{NN} & C_{NM} \\ C_{MN} & C_{MM} \end{bmatrix} \quad (2.14)$$

$\mathbf{C}$  is symmetric, thus  $C_{MN} = C_{NM}$ . The terms  $C_{ij}$  are determined from the stress intensity calibrations of SEN specimens using the energy/compliance relationship proposed by Rice [35].

In the load controlled situation the energy release rate is

$$\mathcal{G} = \frac{1}{2} \mathbf{Q} \frac{\partial \mathbf{q}}{\partial a} \quad (2.15)$$

$$\mathbf{Q} = [N, M]^T \quad (2.16)$$

$$\mathbf{q} = [\delta, \theta]^T \quad (2.17)$$

Now writing the generalised forces and displacements connected by the compliance as

$$\delta = C_{NN}N + C_{NM}M \quad (2.18)$$

$$\theta = C_{MN}N + C_{MM}M \quad (2.19)$$

$$C_{NM} = C_{MN} \quad (2.20)$$

Now combining Eq. 2.15 and Eq. 2.20 to write the energy release rate as

$$\mathcal{G} = \frac{1}{2} \left( N^2 \frac{\partial C_{NN}}{\partial a} + 2NM \frac{\partial C_{MN}}{\partial a} + M^2 \frac{\partial C_{MM}}{\partial a} \right) \quad (2.21)$$

Additionally, one has from fracture mechanics theory the connection between  $\mathcal{G}$  and stress intensity factors. This leads to the elastic compliances in the following way:

$$K_{I,N} = \frac{N}{t} \sqrt{\pi a} \cdot f_N = \sigma_N \sqrt{\pi a} f_N \quad (2.22)$$

$$K_{I,M} = \frac{M}{\frac{1}{6}t} \sqrt{\pi a} \cdot f_M = \sigma_M \sqrt{\pi a} f_M \quad (2.23)$$

where  $f_N$  and  $f_M$  are polynomials of crack depth to thickness ratio. The polynomials  $f_N$  and  $f_M$  are found from stress intensity handbooks, e.g. Tada et al. [46]. The following polynomials are used in the finite element code:

$$f_N = 1.122 - 0.231 \left(\frac{a}{t}\right) + 10.550 \left(\frac{a}{t}\right)^2 - 21.710 \left(\frac{a}{t}\right)^3 + 30.382 \left(\frac{a}{t}\right)^4 \quad (2.24)$$

$$f_M = 1.122 - 1.40 \left(\frac{a}{t}\right) + 7.33 \left(\frac{a}{t}\right)^2 - 13.08 \left(\frac{a}{t}\right)^3 + 14.0 \left(\frac{a}{t}\right)^4 \quad (2.25)$$

For a range of crack depth to thickness ratios from 0.0 to 1.0, the polynomials are plotted in Fig. 2.2.

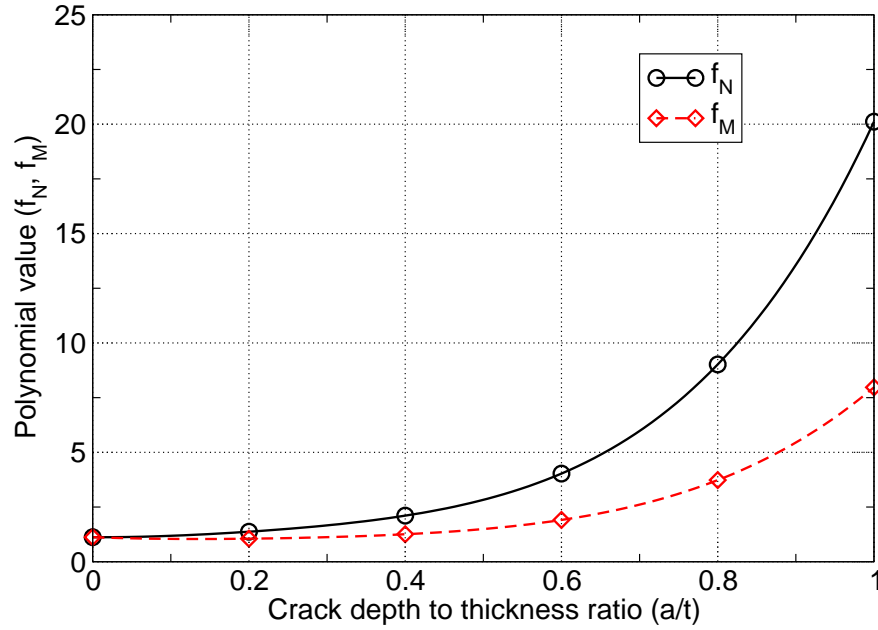


Figure 2.2: Polynomials ( $f_N$  and  $f_M$ ) for the elastic compliance in the line-spring element

The energy release rate by means of the stress intensity factor is expressed as

$$\mathcal{G} = \frac{K_I^2}{E'} = \frac{\pi a}{E'} (\sigma_N^2 f_N^2 + 2\sigma_N \sigma_M f_N f_M + \sigma_M^2 f_M^2) \quad (2.26)$$

By combining Eqs. 2.21-2.26 the expressions for the elastic compliances are found as

$$C_{NN} = \frac{2\pi}{E't^2} \int_0^a a f_N^2 da \quad (2.27)$$

$$C_{MN} = \frac{2\pi}{E'\frac{1}{6}t^3} \int_0^a a f_N f_M da \quad (2.28)$$

$$C_{MM} = \frac{2\pi}{E'\frac{1}{36}t^4} \int_0^a a f_M^2 da \quad (2.29)$$

Using the generalised forces, the Mode-I stress intensity factor is given by

$$K_I = \sqrt{t} \left( \frac{N}{t} k_N + \frac{6M}{t^2} k_M \right) \quad (2.30)$$

where  $k_N$  and  $k_M$  are functions from Gross and Srawley [14] (can also be obtained from handbook, e.g. Tada et al [46]). They are expressed in Eqs. 2.31-2.32 and plotted as functions of crack depth to thickness ratios in Fig. 2.3.

$$k_N = \sqrt{\frac{a}{t}} \left( 1.99 - 0.41 \left( \frac{a}{t} \right) + 18.70 \left( \frac{a}{t} \right)^2 - 38.48 \left( \frac{a}{t} \right)^3 + 53.85 \left( \frac{a}{t} \right)^4 \right) \quad (2.31)$$

$$k_M = \sqrt{\frac{a}{t}} \left( 1.99 - 2.47 \left( \frac{a}{t} \right) + 12.97 \left( \frac{a}{t} \right)^2 - 23.17 \left( \frac{a}{t} \right)^3 + 24.80 \left( \frac{a}{t} \right)^4 \right) \quad (2.32)$$

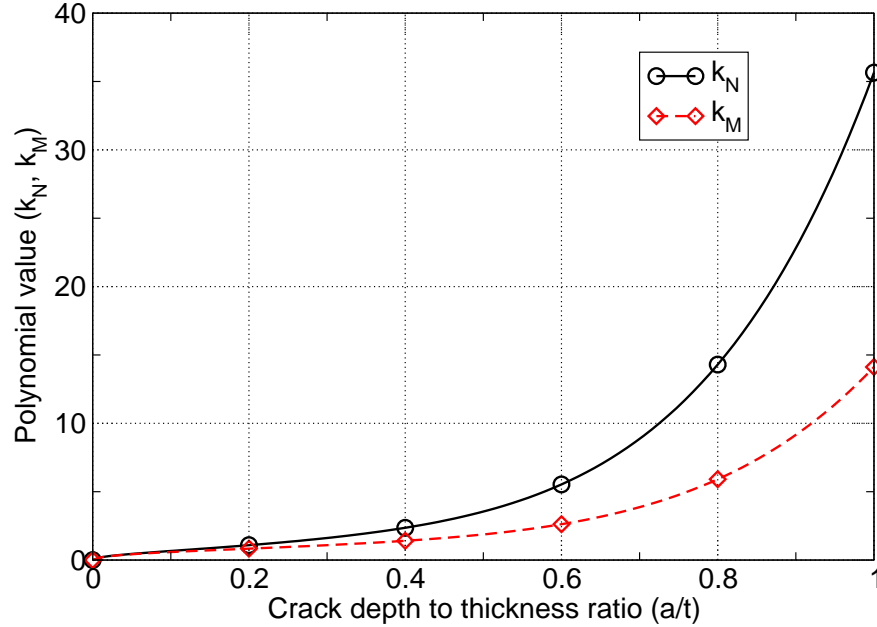


Figure 2.3: The polynomials ( $k_N$  and  $k_M$ ) used in the computation of the mode I stress intensity factor

Due to local plasticity ahead of the crack tip even at elastic load levels, the crack depth behaves as if it was deeper than what it is (see Irwin [20]). Hauf et al. [16] and Lee and

Parks [24] presented a modified effective crack depth formulation for the line-spring element as

$$a_{eff} = a_0 + 0.0195 \left( \frac{K_I(a_{eff})}{\sigma_0} \right)^2 \quad (2.33)$$

A Newton-Raphson iteration scheme is used to compute  $a_{eff}$  which is used in the subsequent computations of the line-spring element.

The J-integral is related to the stress intensity factor, in the case of plane strain, through,

$$J_{el} = (1 - \nu^2) \frac{K_I^2}{E} \quad (2.34)$$

Wang and Parks [48] reasoned that arguments similar to those used in the derivation of stress intensity factor can also be applied for the  $T$ -stress evaluation in surface cracked plates and shell structures. Hence, the  $T$ -stress is the summation of the contributions from the generalised forces. Thus, the  $T$ -stress at any point along the crack front can be expressed as

$$T = \frac{N}{t} t_N + \frac{6M}{t^2} t_M \quad (2.35)$$

where functions  $t_N$  and  $t_M$  are calibration factors for  $T$  in a SEN specimen with the same crack depth to thickness ratio, under unit membrane and bending loads. Sham [38] tabulated these functions for a range of crack depth using second order weight functions. A polynomial fit of the tabulated data from Sham [38] was derived by Wang and Parks [48] as expressed in Eqs. 2.36-2.37. These functions are used in the present line-spring model. The polynomials are plotted in Fig. 2.4.

$$t_N = -0.501 - 1.842 \left( \frac{a}{t} \right) + 14.48 \left( \frac{a}{t} \right)^2 - 45.03 \left( \frac{a}{t} \right)^3 + 47.42 \left( \frac{a}{t} \right)^4 \quad (2.36)$$

$$t_M = -0.505 + 0.906 \left( \frac{a}{t} \right) + 3.637 \left( \frac{a}{t} \right)^2 - 10.73 \left( \frac{a}{t} \right)^3 + 14.08 \left( \frac{a}{t} \right)^4 \quad (2.37)$$

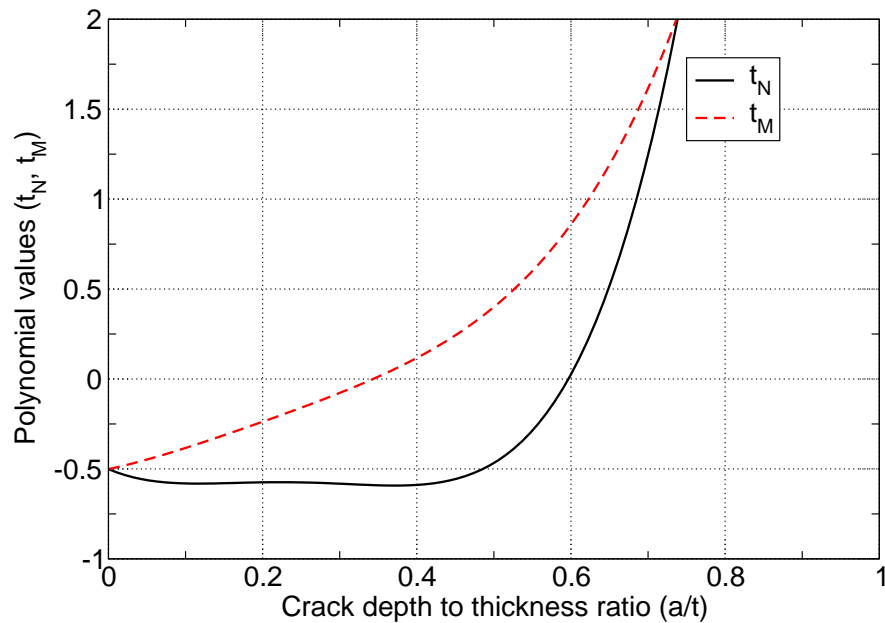


Figure 2.4: The polynomials ( $t_N$  and  $t_M$ ) used in the computation of the  $T$ -stress

Wang and Parks [48] derived their polynomials for the crack depth to thickness range of 0.1 to 0.8. They further show a significant deviation between the line-spring model and 3D continuum models for crack depth to thickness ratios above 0.6. The implementation in  $\text{LINK}_{\text{pipe}}$  follows the same limitations.

### 2.1.3 Elastic-plastic line-spring

The plastic line-spring response is based on a pointwise convex yield surface and an associated flow rule with isotropic hardening. Mode I (normal crack opening) is the only fracture mode in the current implementation. Skallerud [41] demonstrated the applicability of a combined mode I/II line-spring formulation, but this enhancement is not used herein.

The yield surface,  $\Phi(Q_i, a, t, \sigma(\varepsilon^{\text{pl}}))$ , is based on the work of Lee and Parks [24] who presented a set of tabulated points to describe the yield surfaces for a range of crack depth to thickness ratios. Berg et al. [5] expanded the number of tabulated yield surfaces to refine the transition between crack depth to thickness ratios. The yield surfaces are constructed in the stress resultant space where the  $x$ -axis is the normalised bending moment and the  $y$ -axis is the normalised membrane force. A linear interpolation between the tabulated surfaces is used to calculate the intermediate surfaces. Tabulated yield surfaces for a range of crack depth to thickness ratios are shown in Fig. 2.5.

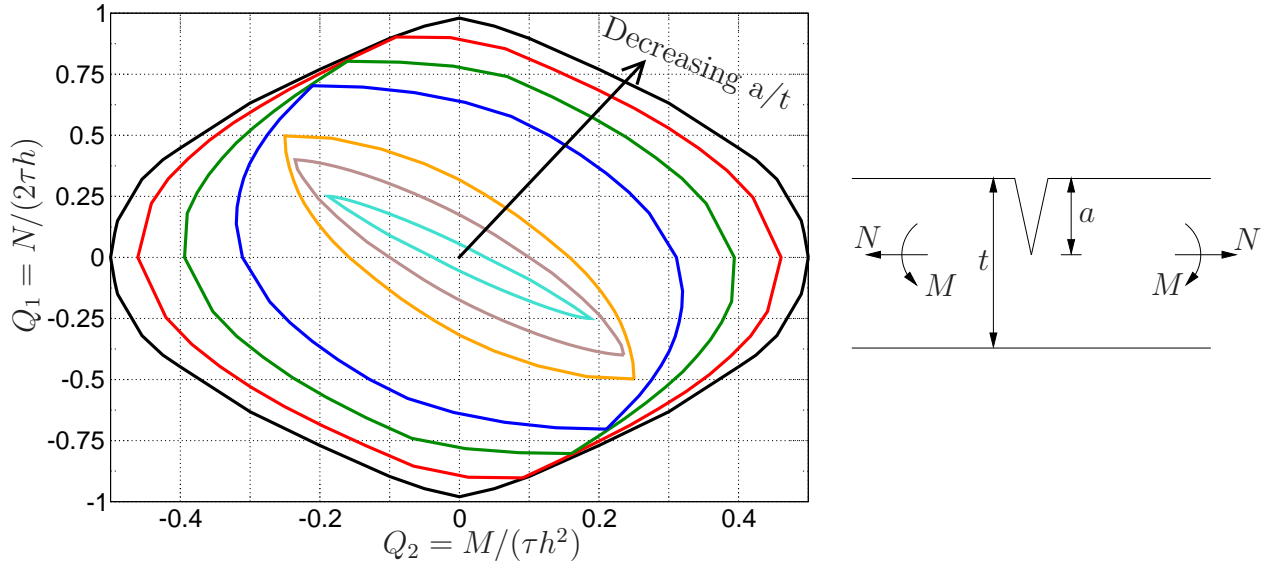


Figure 2.5: Tabulated yield surfaces for a range of crack depth to thickness ratios

The formulation assumes an additive decomposition of the incremental generalised displacements into an elastic and plastic part as shown in Eq. 2.38.

$$dq_i = dq_i^{\text{el}} + dq_i^{\text{pl}} \quad (2.38)$$

If the product of incremental generalised displacements and the normal vector of the yield surface is greater than zero, i.e.  $dq_i \dot{\Phi}_Q > 0$ , plastic deformation occurs. The plastic part of the generalised displacement increment is assumed to follow the normality rule, which means that it can be expressed as the product of the normal vector of the yield surface and

a positive scalar as shown in Eq. 2.39.

$$dq_i^{pl} = \Lambda \dot{\Phi}_Q = \Lambda \frac{\partial \Phi}{\partial Q_j} \quad (2.39)$$

The plastic multiplier,  $\Lambda$  is computed from the consistency condition (see Eq. 2.40) during plastic loading. This forces the updated stress point to be located on the yield surface at the end of the load step.

To account for work hardening of the material a hardening law is introduced using the average equivalent plastic strain over the ligament. The material's uniaxial stress strain curve is employed as user input which gives a non-linear material response as demonstrated by Jayadevan et al. [22].

$$d\Phi = \frac{\partial \Phi}{\partial Q_i} dQ_i + \frac{\partial \Phi}{\partial \sigma} d\sigma = 0 \quad (2.40)$$

where  $d\sigma$  is found using the slope,  $h$ , of the uniaxial stress strain curve as expressed in Eq. 2.41.

$$d\sigma = h d\varepsilon^{pl} \quad (2.41)$$

To relate the plastic part of the generalised displacement increment to the average plastic strain over the remaining ligament, the incremental plastic work per unit length over the ligament is used. The incremental plastic work over the ligament can be written in two ways as proposed by Parks [34] and Parks and White [49]. Following classical plasticity theory, the incremental plastic work using generalised field quantities is given as

$$dW^{pl} = Q_i dq_i^{pl} = \Lambda Q_i \frac{\partial \Phi}{\partial Q_i} \quad (2.42)$$

Parks and White [49] argues that the incremental plastic work can be written as the integral of the continuum over the area,  $A$ , of the surface cracked structure as

$$dW^{pl} = \int_A \sigma_{ij} d\varepsilon_{ij}^{pl} dA \quad (2.43)$$

where the area  $A$  is a characteristic area of the edge-cracked problem. It is assumed that the yielding only occurs in the remaining ligament,  $c = t - a$  (see also Fig. 2.6). Hence the area,  $A$ , is defined as the square of the remaining ligament. Using this in the integral in Eq. 2.43, the equation of the incremental plastic work can be approximated to

$$dW^{pl} = f \cdot \sigma_y(\varepsilon^{pl}) \cdot d\varepsilon^{pl} \cdot (t - a)^2 \quad (2.44)$$

where  $f$  is a non-dimensional scalar which is called the “strain hardening factor” which is expected to be of order unity.

The incremental stress increment is written as

$$dQ_i = C_{ij} dq_j = C_{ij} (dq_j - dq_j^{pl}) \quad (2.45)$$

Combining Eq. 2.42 and Eq. 2.44 gives the following expression for the plastic strain:

$$d\varepsilon^{pl} = \Lambda Q_i \frac{\partial \Phi}{\partial Q_i} \cdot \frac{1}{f c^2 \sigma} \quad (2.46)$$

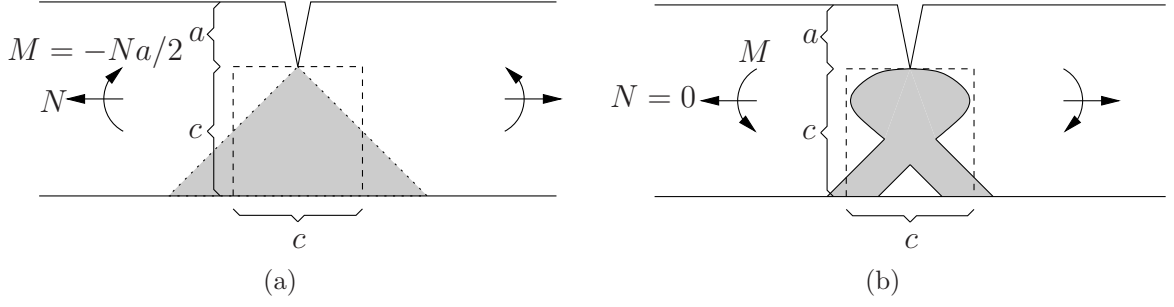


Figure 2.6: Slip line field approximation in the  $kc$ -zone for (a) pure tension and (b) pure bending

Now combining Eqs. 2.38, 2.39, 2.40, 2.45 and 2.46 the expression for  $\Lambda$  is found as

$$\Lambda = \frac{\frac{\partial \Phi}{\partial Q_i} C_{ij}}{\frac{\partial \Phi}{\partial Q_m} C_{mn} \frac{\partial \Phi}{\partial Q_n} - \frac{\partial \Phi}{\partial \sigma} \frac{\partial \Phi}{\partial Q_k} Q_k \frac{h}{f c^2 \sigma}} dq_j \quad (2.47)$$

Inserting Eq. 2.47 into Eq. 2.45 gives the tangent stiffness for as integration point of the line-spring element:

$$C_{ij}^{pl} = C_{ij} - \frac{C_{ik} \frac{\partial \Phi}{\partial Q_k} \frac{\partial \Phi}{\partial Q_l} C_{lj}}{\frac{\partial \Phi}{\partial Q_m} C_{mn} \frac{\partial \Phi}{\partial Q_n} - \frac{\partial \Phi}{\partial \sigma} \frac{\partial \Phi}{\partial Q_o} Q_o \frac{h}{f c^2 \sigma}} \quad (2.48)$$

The crack driving force  $J$  or CTOD are readily available from the line-spring element. As for the generalised displacements, the  $J$  or CTOD also follows an additive decomposition of an elastic and a plastic part. The incremental plastic part of the  $CTOD$  is expressed as

$$d\delta^{pl} = C_N(Q_N, \sigma_y, a, t) d\Delta^{pl} + C_M(Q_M, \sigma_y, a, t) t d\theta^{pl} \quad (2.49)$$

where the functions  $C_N$  and  $C_M$  are dimensionless functions presented by Lee and Parks [24].

As described in Sec. 2.1.2, the constraint level in the line-spring element is computed using the  $T$ -stress. This quantity is based on elastic assumptions, but Lee and Parks [24] proposed to extend the use of Eq. 2.35 from the elastic-plastic line-spring behaviour using the current values of the generalised forces,  $M$  and  $N$ . Under linear-elastic conditions the ratio between the generalised forces is constant, but for elastic-plastic conditions, the ratio is varying with the loading and this is immediately taken care of in the computation of the  $T$ -stress. Jayadevan et al. [22] showed the applicability of using this “elastic-plastic  $T$ -stress” for the line-spring element.

### 2.1.4 Non linear kinematic hardening

The previous line-spring element implementation was based on incremental isotropic hardening where the yield surface expands according to the equivalent plastic strain. The new implementation makes use of a Ziegler-like kinematic translation rule in addition to the already existing isotropic hardening model. The stiffness matrix is a relation between the

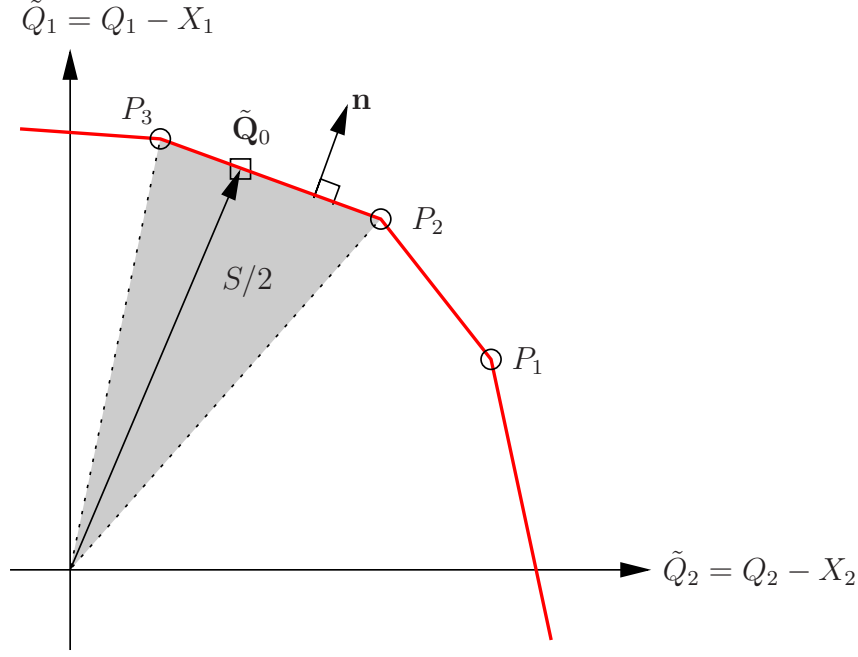


Figure 2.7: Definitions for the normal vector to a line segment

generalised displacements (elongation and rotation), and the generalised forces (membrane force and bending moment).

In the following, the generalised forces,  $\mathbf{Q}$ , the back stress vector,  $\mathbf{X}$ , and the elastic stiffness matrix,  $\mathbf{C}$ , in the line-spring element are normalised according to the axes definitions in Fig. 2.5. Considering a line segment from point number  $P_2$  to  $P_3$  on the pointwise yield surface as shown in Fig. 2.7 where the normalised stress resultant vector from last equilibrium is denoted  $\tilde{\mathbf{Q}}_0$ . The vector,  $\mathbf{n}$ , orthogonal to line segment  $P_2 - P_3$  in Fig. 2.7 is defined as

$$\mathbf{n} = \frac{1}{S} \begin{bmatrix} \tilde{Q}_{1,P3} - \tilde{Q}_{1,P2} \\ -(\tilde{Q}_{2,P3} - \tilde{Q}_{2,P2}) \end{bmatrix} = \frac{1}{S} \mathbf{b} \quad (2.50)$$

$$S = \tilde{Q}_{2,P2} \cdot \tilde{Q}_{1,P3} - \tilde{Q}_{2,P3} \cdot \tilde{Q}_{1,P2} \quad (2.51)$$

where  $S$  is twice the area of the stapled, shaded triangle in Fig. 2.7. Note that  $\mathbf{n}$  is not a unit vector. The yield function can be expressed as the product of the normalised stress resultant vector,  $\tilde{\mathbf{Q}} = \mathbf{Q} - \mathbf{X}$ , and the normal vector,  $\mathbf{n}$ , as

$$f^n = \mathbf{n}^T (\mathbf{Q}^n - \mathbf{X}^n) - 1 = 0 \quad (2.52)$$

The superscript  $n$  denotes configuration from last equilibrium.

In a load increment the yield surface is first expanded isotropically (see Fig. 2.9b) and then translated according to the back stress vector (Fig. 2.9c). Fig. 2.8 shows schematically both the numerical expansion and the translation of the yield surface for the proposed kinematic hardening model.

The modified yield function for the isotropically expanded yield surface now reads

$$\tilde{f}^{n+1} = (\mathbf{n}^{n+1})^T (\mathbf{Q}^{n+1} - \mathbf{X}^n) - \left( \frac{\Delta\sigma^{n+1}}{\sigma_0} + 1 \right) = 0 \quad (2.53)$$



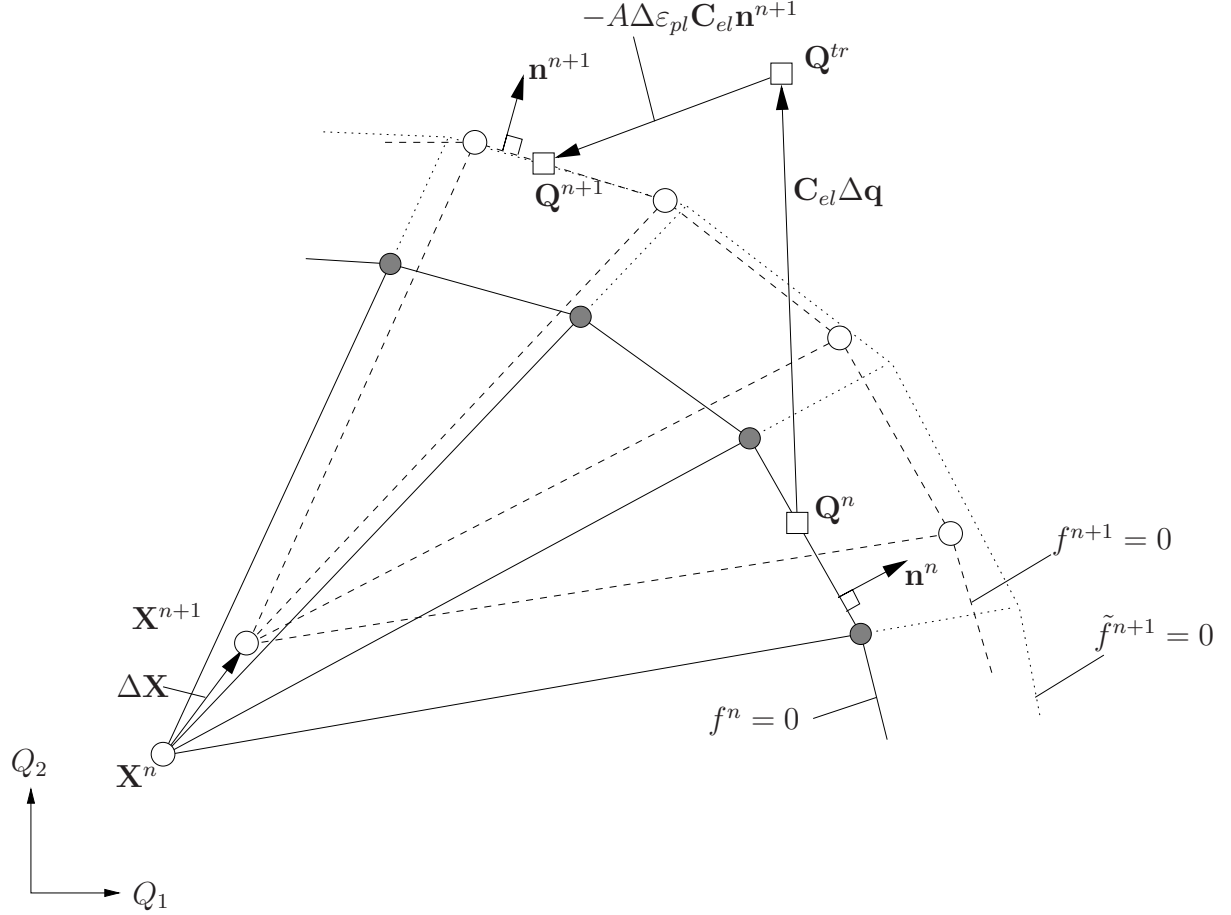


Figure 2.8: Proposed kinematic translation rule for line-spring element

where  $\sigma^{n+1}$  is the updated stress level,  $\sigma^n$  is the stress level from last equilibrium and  $\sigma_0$  is the yield stress. The trial point is expressed as

$$\mathbf{Q}^{tr} = \mathbf{Q}^n + \mathbf{C}_{el} \Delta \mathbf{q} \quad (2.54)$$

where  $\mathbf{C}_{el}$  is the elastic stiffness matrix and  $\Delta \mathbf{q}$  are the normalised generalised displacements. The flow rule reads

$$\Delta \mathbf{q}_{pl} = \Delta \lambda \mathbf{n}^{n+1} \quad (2.55)$$

A plastic work equation for the line-spring element was proposed by Lee and Parks [1995] and is expressed as shown in Eq. 2.56 for combined hardening.

$$(\mathbf{Q}^{n+1} - \mathbf{X}^{n+1})^T \Delta \mathbf{q}_{pl} = k \cdot \left(1 - \frac{a}{t}\right)^2 \sigma_0 \Delta \varepsilon_{pl} = A \cdot \Delta \varepsilon_{pl} \quad (2.56)$$

where  $k$  is dimensionless scalar which Lee and Parks [1995] named *the strain hardening factor* and  $\Delta \varepsilon_{pl}$  is the equivalent plastic strain. Now combining Eqs. 2.55 and 2.56, the plastic multiplier is expressed as

$$\Delta \lambda = A \cdot \Delta \varepsilon_{pl} \quad (2.57)$$

Combining Eqs. 2.54 and 2.55 the updated stress resultants at the end of the load increment reads

$$\begin{aligned} \mathbf{Q}^{n+1} &= \mathbf{Q}^n + \mathbf{C}_{el} \Delta \mathbf{q}_{el}^{n+1} \\ &= \mathbf{Q}^n + \mathbf{C}_{el} \Delta \mathbf{q}^{n+1} - \mathbf{C}_{el} \Delta \mathbf{q}_{pl}^{n+1} \\ &= \mathbf{Q}^{tr} - A \Delta \varepsilon_{pl} \mathbf{C}_{el} \mathbf{n}^{n+1} \end{aligned} \quad (2.58)$$

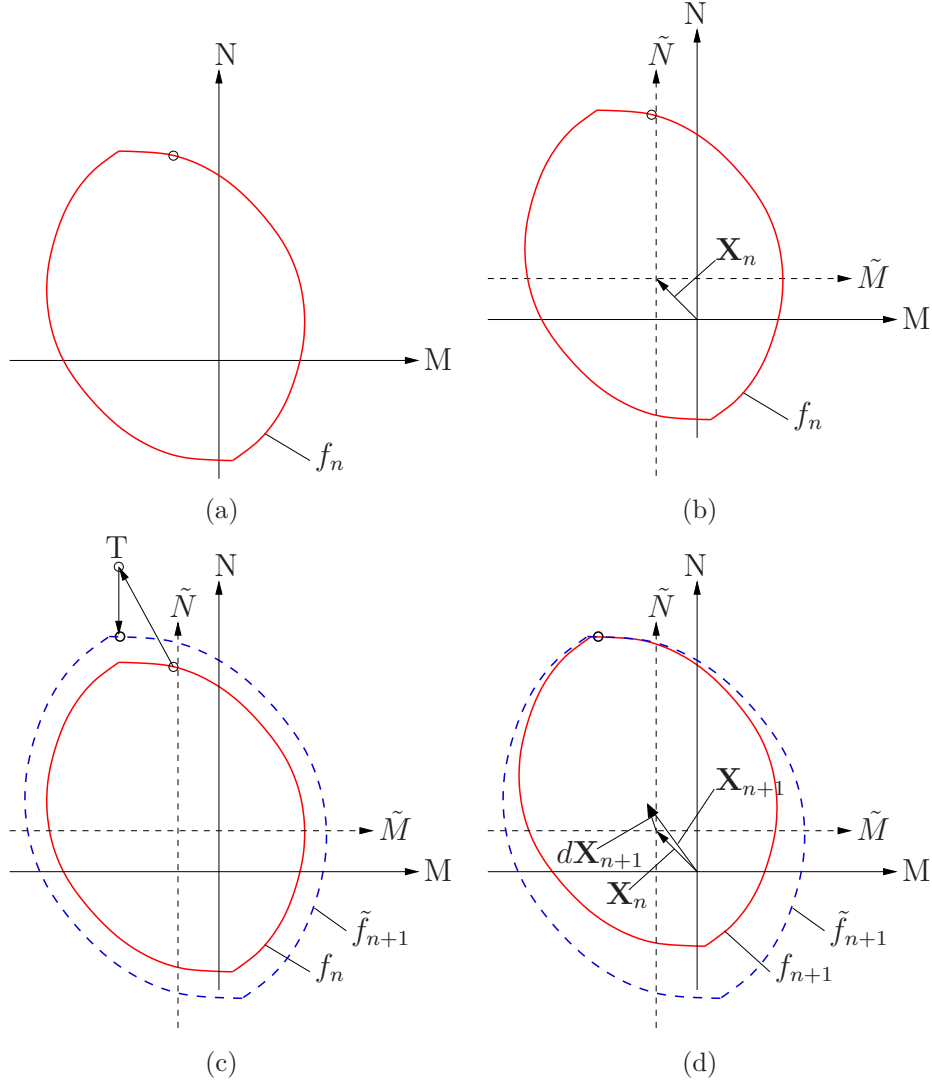


Figure 2.9: (a) Initial yield surface followed by (b) an incremental isotropic expansion due to hardening. The initial yield surface (c) is translated according to the method shown in Fig. 2.8, thus the yield surface position at the end of the load increment is shown in (d).

Premultiplying Eq. 2.58 with the normal vector of the yield surface and combining with the updated yield function (Eq. 2.53), the result is

$$A\Delta\varepsilon_{pl} (\mathbf{n}^{n+1})^T \mathbf{C}_{el} \mathbf{n}^{n+1} + \left( \frac{\Delta\sigma^{n+1}}{\sigma_0} + 1 \right) = (\mathbf{n}^{n+1})^T (\mathbf{Q}^{tr} - \mathbf{X}^n) \quad (2.59)$$

Solving Eq. 2.59 for equivalent plastic strain, a Newton-Raphson iteration process is used. The iteration stops when the expression  $|\Delta\varepsilon_{pl}^{(i+1)} - \Delta\varepsilon_{pl}^{(i)}|$  is less than some tolerance. The quantity  $i$  is here the local iteration number. Now the updated stress resultant point is located on the isotropically expanded yield surface (dashed surface on Fig. 2.9b). The updated back stress vector is defined as the difference vector between the updated stress resultant point and the back stress from last equilibrium as shown in Eq. 2.60.

$$\Delta\mathbf{X} = \Delta\beta (\mathbf{Q}^{n+1} - \mathbf{X}^n) \quad (2.60)$$

where  $\Delta\beta$  is still an unknown scalar. Premultiplication with  $\mathbf{n}^{n+1}$  in Eq. 2.60 and inserting

into yield function (Eq. 2.53) Eq. 2.60 is transformed to

$$(\mathbf{n}^{n+1})^T \Delta \mathbf{X} = \Delta \beta (\mathbf{n}^{n+1})^T (\mathbf{Q}^{n+1} - \mathbf{X}^n) = \Delta \beta \left( \frac{\Delta \sigma^{n+1}}{\sigma_0} + 1 \right) \quad (2.61)$$

The yield function for the updated yield surface (Fig. 2.9c) is zero at the end of the stress update, and is now expressed as

$$f^{n+1} = (\mathbf{n}^{n+1})^T (\mathbf{Q}^{n+1} - \mathbf{X}^{n+1}) - 1 = 0 \quad (2.62)$$

Combining Eqs. 2.53 and 2.62 gives

$$\begin{aligned} (\mathbf{n}^{n+1})^T (\mathbf{Q}^{n+1} - \mathbf{X}^{n+1}) - 1 &= (\mathbf{n}^{n+1})^T (\mathbf{Q}^{n+1} - \mathbf{X}^n) - \left( \frac{\Delta \sigma^{n+1}}{\sigma_0} + 1 \right) \\ \Rightarrow (\mathbf{n}^{n+1})^T (\mathbf{X}^{n+1} - \mathbf{X}^n) &= \frac{\Delta \sigma^{n+1}}{\sigma_0} \\ \Rightarrow (\mathbf{n}^{n+1})^T \Delta \mathbf{X} &= \frac{\Delta \sigma^{n+1}}{\sigma_0} \end{aligned} \quad (2.63)$$

Now inserting Eq. 2.63 into Eq. 2.60, the scalar  $\Delta \beta$  is expressed as

$$\Delta \beta = \frac{\Delta \sigma^{n+1}}{\Delta \sigma^{n+1} + \sigma_0} \quad (2.64)$$

Using the result from Eq. 2.64, the updated back stress vector for the line-spring element is expressed as

$$\begin{aligned} \mathbf{X}^{n+1} &= \mathbf{X}^n + \Delta \mathbf{X} \\ &= \mathbf{X}^n + \Delta \beta (\mathbf{Q}^{n+1} - \mathbf{X}^n) \end{aligned} \quad (2.65)$$

When the updated stress point and the updated back stress vector is found, the incremental elastic-plastic stiffness relation is found by introducing the consistency condition and applying the result from Eq. 2.55 as shown in the following.

The incremental stress resultant change,  $\Delta \mathbf{Q}$  is expressed as

$$\Delta \mathbf{Q} = \mathbf{C}_{el} \Delta \mathbf{q}_{el} \quad (2.66)$$

where  $\Delta \mathbf{q}_{el} = \Delta \mathbf{q} - \Delta \mathbf{q}_{pl}$  and  $\Delta \mathbf{q}_{pl}$  is found from the flow rule in Eq. 2.55. Differentiation of Eq. 2.66 gives the infinitesimal stress resultant change as

$$d\mathbf{Q} = \mathbf{C}_{el} d\mathbf{q} - d\lambda \mathbf{C}_{el} \mathbf{n}^{n+1} - \Delta \lambda \mathbf{C}_{el} \frac{\partial \mathbf{n}}{\partial \mathbf{Q}} d\mathbf{Q} \quad (2.67)$$

Since the yield function is linear between two points, the second derivative vanishes, hence the infinitesimal stress resultant change can be expressed as

$$d\mathbf{Q} = \mathbf{C}_{el} d\mathbf{q} - d\lambda \mathbf{C}_{el} \mathbf{n}^{n+1} \quad (2.68)$$

The consistency condition based on the modified yield surface (Eq. 2.53) reads

$$(\mathbf{n}^{n+1})^T d\mathbf{Q} - \frac{1}{\sigma_0} \frac{\partial \sigma}{\partial \varepsilon_{pl}} d\varepsilon_{pl} = 0 \quad (2.69)$$

where  $\partial \sigma / \partial \varepsilon_{pl}$  is the current slope of the stress-strain curve. Combining the consistency condition and the infinitesimal stress change from Eq. 2.68, the incremental line-spring tangent stiffness matrix is written as

$$\begin{aligned} d\mathbf{Q} &= \mathbf{C}_{ct} d\mathbf{q} \\ &= \left[ \mathbf{C}_{el} - \frac{(\mathbf{n}^T \mathbf{C}_{el})^T (\mathbf{n}^T \mathbf{C}_{el})}{\mathbf{n}^T \mathbf{C}_{el} \mathbf{n} + \frac{\partial \sigma}{\partial \varepsilon_{pl}} \frac{1}{\sigma_0 k \cdot \left(1 - \frac{a}{t}\right)^2}} \right] d\mathbf{q} \end{aligned} \quad (2.70)$$

### 2.1.5 Contact formulation - crack closure

The concept of crack closure is challenging to manage. Here a simple methodology to account for crack closure for the line-spring element is presented.

To avoid material merging at the location of the crack mouth, an elastic spring with very large stiffness is used (see Fig. 2.10a). When the crack mouth points from each crack face get in contact due to reversed loading, the spring is activated to avoid further relative displacement. The same methodology is used to prevent material crossing in the cracked ligament. An elastic spring is positioned at mid-ligament position (see Fig. 2.10b). These springs will be a contribution to the stiffness matrix in the integration point as expressed in Eq. 2.71. The expression of the stiffness matrix of the springs are relative to the centre-line of the thickness, thus eccentric terms in the stiffness matrices occur as shown in the two last matrices in Eq. 2.71. Fig. 2.10 shows the location of the two springs.

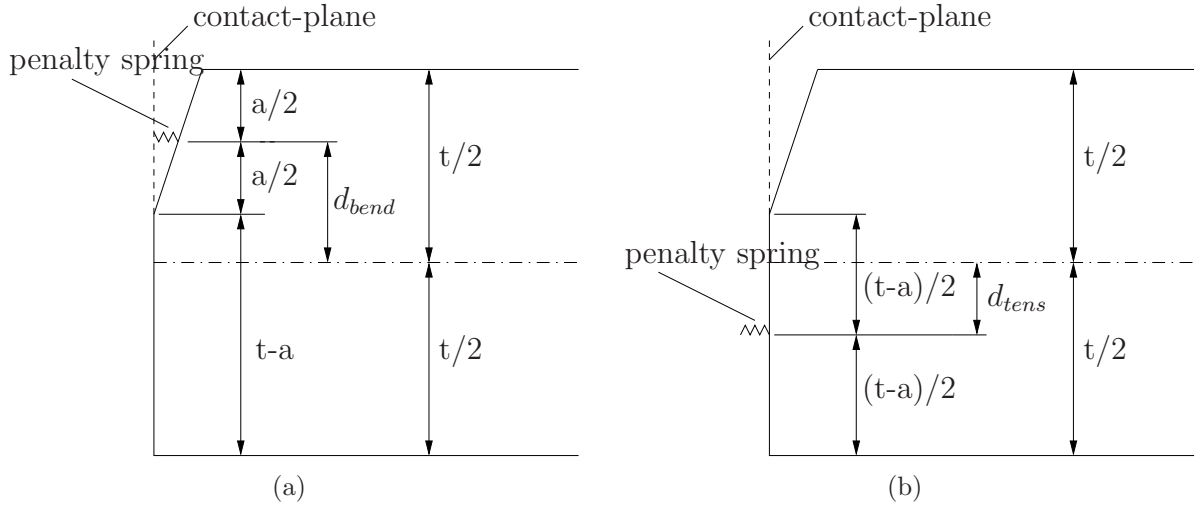


Figure 2.10: Schematic views of the high stiffness elastic contact springs illustrated for an open crack for (a) bending and (b) tensile situations

$$\begin{aligned}
 k_s &= \alpha \frac{Ea}{l} \\
 \mathbf{K} &= \mathbf{K}_{mat} + \mathbf{K}_{s,bend} + \mathbf{K}_{s,tens} \\
 \begin{bmatrix} K_{11} & K_{12} \\ K_{21} & K_{22} \end{bmatrix} &= \begin{bmatrix} K_{11}^{mat} & K_{12}^{mat} \\ K_{21}^{mat} & K_{22}^{mat} \end{bmatrix} + \begin{bmatrix} k_s & d_{bend} \cdot k_s \\ d_{bend} \cdot k_s & d_{bend}^2 \cdot k_s \end{bmatrix} + \begin{bmatrix} k_s & -d_{tens} \cdot k_s \\ -d_{tens} \cdot k_s & d_{tens}^2 \cdot k_s \end{bmatrix} \quad (2.71)
 \end{aligned}$$

where  $\alpha$  is a high value scalar, e.g.  $10^7$ , to ensure sufficient high axial stiffness.  $E$  is the Young's modulus for the material,  $a$  is the crack depth and  $l$  is the axial length of the spring (small number).  $d_{tens}$  is the distance from the spring to the centre line of the thickness. For the temporary spring for bending situation, the value of  $d_{bend}$  is  $(t-a)/2$ . The terms  $K_{ij}^{mat}$  in Eq. 2.71 are the terms from the tangent stiffness matrix in Eq. 2.48.

The high stiffness elastic spring introduced in membrane situations is similar to the one in bending situations. The main difference lies in the measure for when the spring should be activated, i.e. when the crack faces are in contact. The axial elongation of the line-spring element is used as a measure. When the axial elongation is reduced back to zero due to compressive loading, the elastic spring is activated. The formulation is equal to the

formulation of the spring at bending situation. The eccentricity quantity,  $d_{tens}$ , is equal to half the crack depth,  $a/2$ . Fig. 2.10b shows the location of the spring.

When the crack faces are not in contact, the springs shown in Fig. 2.10 are not active. The springs are activated separately when they satisfy the contact conditions expressed in Eq. 2.72.

$$k_{s,bend} = \begin{cases} k_s & v_{bend} \leq 0 \\ 0 & v_{bend} > 0 \end{cases}, \quad k_{s,tens} = \begin{cases} k_s & v_{tens} \leq 0 \\ 0 & v_{tens} > 0 \end{cases} \quad (2.72)$$

where  $v_{bend}$  and  $v_{tens}$  are expressed in Eq. 2.73.

$$v_{bend} = \Delta + \frac{t-a}{t}\theta, \quad v_{tens} = \Delta - \frac{a}{2}\theta \quad (2.73)$$

where  $\Delta$  and  $\theta$  are the accumulated generalised line-spring displacement and rotation in the integration point.

### 2.1.6 Ductile crack growth

Ductile crack growth is implemented in the line-spring element for fully plastic conditions. Jayadevan et al. [21] showed the applicability of using the crack growth resistance curve which is in accordance with the established use as defined in BS7910:1999 [8]. The crack growth resistance curve employed in  $LINK_{pipe}$  follows the form in Eq. 2.74.

$$CTOD = CTOD_i + C_1(\Delta a)^{C_2} \quad (2.74)$$

where  $CTOD_i$  is the critical CTOD-value at onset of ductile tearing.  $C_1$  and  $C_2$  are fitting constants. The updated crack depth at the end of a load increment is expressed as

$$a^{(i+1)} = a^{(i)} + da^{(i)} \quad (2.75)$$

### 2.1.7 Fatigue tearing

Ductile crack growth or tearing is accounted for by employing the crack growth resistance curve. When the crack opens the tearing is computed from the crack growth resistance curve. The crack closes when the local load is reversed. When the distance between the crack faces is reduced, the crack tip opening displacement also decreases and the crack does not grow.

When the crack faces come into contact, the crack is closed and the springs from Fig. 2.10 become active to prevent material crossing. When the load again reverses the crack starts to open again.

It is assumed that the crack depth has increased according to the accumulated tearing from the last crack opening. Fig. 2.11a shows one load cycle with indications of where crack opening occurs and how the crack depth update is handled. Fig. 2.11b shows an example of a crack growth resistance curve where the tearing intervals are marked. In the example in Fig. 2.11a, the initial crack depth is  $a_O$ . At point  $P1$ , the crack growth is  $\Delta a_{P1}$  as marked on Fig. 2.11b. The load is reversed at  $P1$ . During the unloading sequence, the crack is gradually closing and no further tearing occurs. When the compressive load is completed

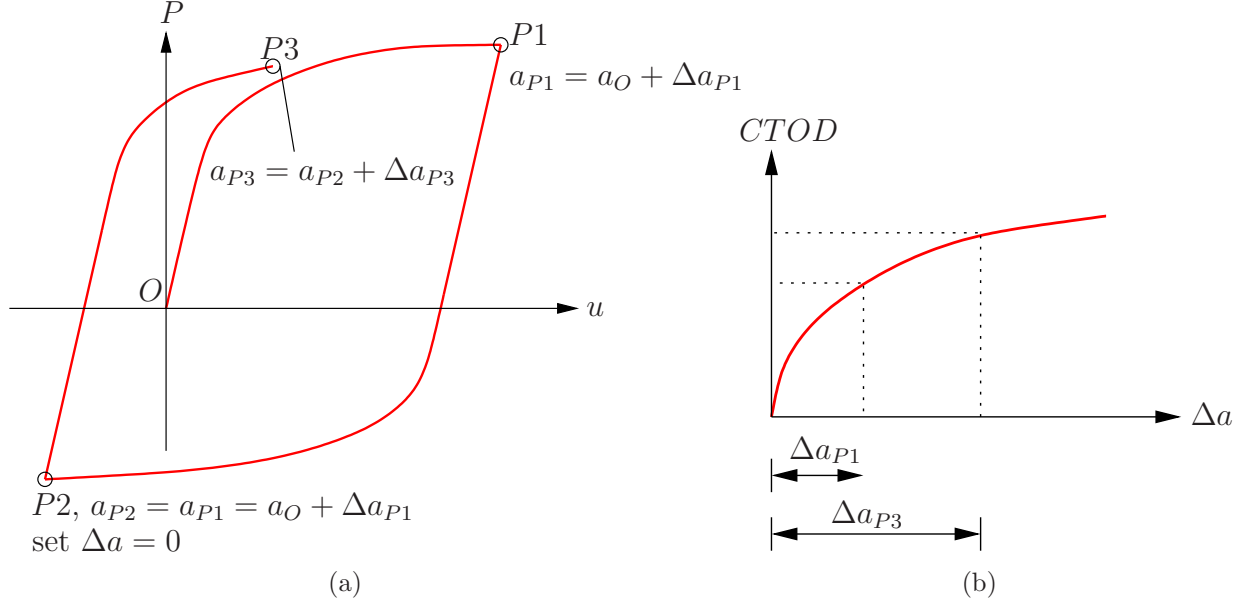


Figure 2.11: (a) an example of a load cycle with ductile tearing and (b) a crack growth resistance curve with tearing contributions from the load cycle in (a) are marked

(point  $P2$  in Fig. 2.11a), the crack depth is updated as  $a_{P2} = a_O + \Delta a_{P1}$  and the ductile tearing is set as zero. When the opening load from  $P2$  to  $P3$  starts, the crack growth starts at zero on the crack growth resistance curve in Fig. 2.11b. At load completion (point  $P3$  on Fig. 2.11a) the ductile crack growth from point  $P2$  to  $P3$  is marked as  $\Delta a_{P3}$  on Fig. 2.11b. If now the load is again reversed, the updating procedure is repeated.

### 2.1.8 Two-parameter fracture assessment

It is well known that the stress field ahead of the crack tip is not only influenced by the loading conditions, but it also depends highly upon the crack geometry. This effect is called constraint. Since the crack initiation of a structure depends upon the stress field in the crack tip region, the fracture parameters depend on the geometry as well as load. Due to this fact, the fracture toughness ( $K_{Ic}$ ,  $J_c$  or  $CTOD$ ) is not a unique material parameter, but also a geometry dependent parameter. The  $T$ -stress is used as a constraint measurement in  $LINK_{pipe}$ .

The  $T$ -stress is the first non-singular term in William's solution of the stress field (Larsson and Carlsson [23] and Du and Hancock [11]), as shown in Eq. 2.76. The  $T$ -stress characterises the local crack tip stress field for materials with the restriction of small-scale yielding (SSY) conditions.

$$[\sigma_{ij}] = \frac{K_I}{\sqrt{2\pi r}} [f_{ij}(\theta)] + \begin{bmatrix} T & 0 & 0 \\ 0 & 0 & 0 \\ 0 & 0 & \nu T \end{bmatrix} \quad (2.76)$$

The  $T$ -stress theory assumes that the  $T$ -stress corresponds to elastic conditions. Most published data on the  $T$ -stress is based on plate solutions, whereas few studies are carried out for the pipe geometry. Jayadevan et al. [22] have provided a  $T$ -stress compendium for surface cracked pipes where the Line-spring element is used. Although the  $T$ -stress is based on elastic assumptions, several studies are performed to extend the use of the  $T$ -stress under large scale

plasticity. Betegon and Hancock [7] and Hancock et al. [15] have shown the applicability of the  $T$ -stress for large scale yielding. In these studies, the  $T$ -stress is computed by employing the elastic biaxiality parameter ( $\beta = T\sqrt{\pi a}/K_I$ ), which is a constant for a given geometry and load. In large-scale yielding conditions, the stress field surrounding the crack tip will change with deformation. The  $T$ -stress in the line-spring element is based on the local membrane force and bending moment, hence the local loading modes are taken into account when computing the “elastic-plastic”  $T$ -stress. This is expected to give a better constraint estimate compared to the one derived from the elastic biaxiality parameter (Jayadevan et al. [22]).

The constraint level for different standard fracture mechanics test specimens are reported by O’Dowd and Shih [32] and Thaulow et al. [47]. These data shows the fracture toughness as a function of the constraint level. This is illustrated as a two-parameter failure locus in Fig. 2.12. It is seen that the widely used three point bend specimen has a high constraint, which yields a low fracture toughness compared to the lower constrained tensile specimen with the same physical geometry. Crack initiation is expected to occur when the driving force cuts the failure curve. For a low constraint geometry, the intersection of the driving force curve and the experimentally derived resistance will allow for higher driving forces than for a high-constrained geometry. Hence, the need for an efficient and accurate constraint procedure arises, such as  $T$ -stress calculated by line-springs.

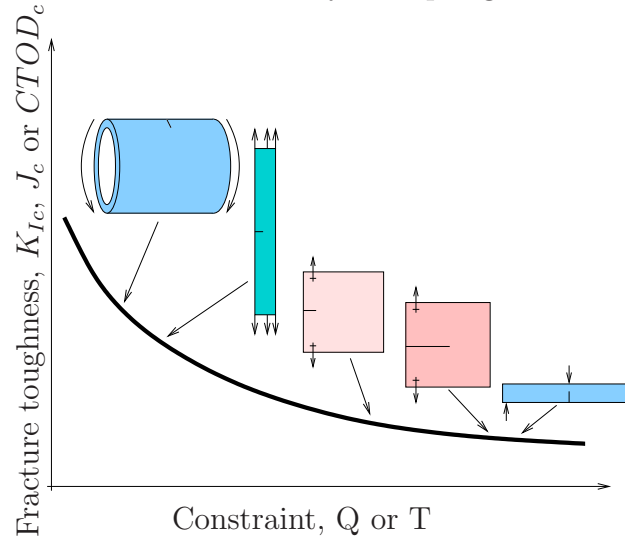


Figure 2.12: Two parameter fracture assessment, failure locus.

The computation of  $T$ -stress from the line-spring element is described in Sec. 2.1.2.

The crack growth resistance curve does not uniquely characterise the material’s crack growth resistance. It also depends on the current geometry and the stress triaxiality ahead of the crack tip as shown by Nyhus et al. [31]. The crack growth resistance curves for two single edge notched bend specimens and one tension specimen are plotted. These results demonstrate the effect of constraint, and the crack growth resistance curve can not be treated directly as a material parameter. Nyhus et al. [31] have shown that the resistance curves can be normalised by employing the  $T$ -stress. They proposed that the resistance curves derived from different test specimens can be corrected for constraint based on a reference crack growth curve as

$$CTOD^{corr} = CTOD^{ref} g(T) \quad (2.77)$$

where  $CTOD^{corr}$  is the constraint corrected resistance curve and  $CTOD^{ref}$  is the reference

curve. One of the crack growth resistance curves should be treated as the reference curve, whereas the other curves are treated as slave curves. The dimensionless function  $g(T)$ , after Ainsworth and O'Dowd [1], is a geometry dependent function which also may depend on the material:

$$g(T) = \begin{cases} \left[ 1 + \alpha \left( -\frac{T(\Delta a)}{\sigma_0} \right)^m \right]^2 & T \leq 0 \\ 1 & T > 0 \end{cases} \quad (2.78)$$

where  $\alpha$  and  $m$  are two fitting parameters.  $T$  is the current  $T$ -stress at any integration point along the crack  $\Delta a$  is the current ductile tearing at any integration point along the crack and  $\sigma_0$  is the material's yield stress. The usage of this methodology has been demonstrated by Berg et al. [4].

### 2.1.9 Circumferential crack growth

In a surface cracked pipe with semi-elliptical surface cracks oriented in the circumferential direction, some amount of circumferential crack growth will occur in addition to the growth in the thickness direction. This crack growth will contribute to the reduction of stiffness in the model.

One benefit of the line-spring model is that it is not necessary to do re-meshing regarding the crack growth in the thickness direction. A procedure to account for crack growth in the circumferential direction is now presented.

The circumferential crack growth is controlled by the initial crack geometry, the loading conditions and the structural geometry.

$$\Delta c = f(a, c, t) \quad (2.79)$$

The initial aspect ratio for the crack geometry is denoted  $a/2c$ , where  $a$  is the initial crack depth and  $2c$  is the total initial crack length.

By the end of each time increment, the crack depth and the crack length is updated.

$$c^{(i+1)} = c^{(i)} + \Delta c^{(i)} \quad (2.80)$$

$$a^{(i+1)} = a^{(i)} + \Delta a^{(i)} \quad (2.81)$$

The quantities in Eq. 2.80 and Eq. 2.81 are shown in Fig. 2.13.

The four nodes at the crack ends is moved along at the end of a time increment, thus increasing the length of the end-elements. The approach is illustrated in Fig. 2.14. Note that in  $\text{LINK}_{\text{pipe}}$ , the line-spring element is given a small transverse extension to achieve a defined local coordinate system in space to fit with the co-rotated formulation. The extension in Fig. 2.14 is artificially large, but used here to clarify the symbols in the figure.

The method showed in Fig. 2.14 is based on nodal movement. The nodes at the crack ends are moved in the circumferential direction to perform ductile tearing in the circumferential direction. In this way, four nodes will be moved, thus 10 shell-elements are altered due to change in local geometry. One should note that if the circumferential crack growth is larger than (almost) the size of the neighbour shell element, a re-meshing is required. In the subsequent analyses, this was not necessary.



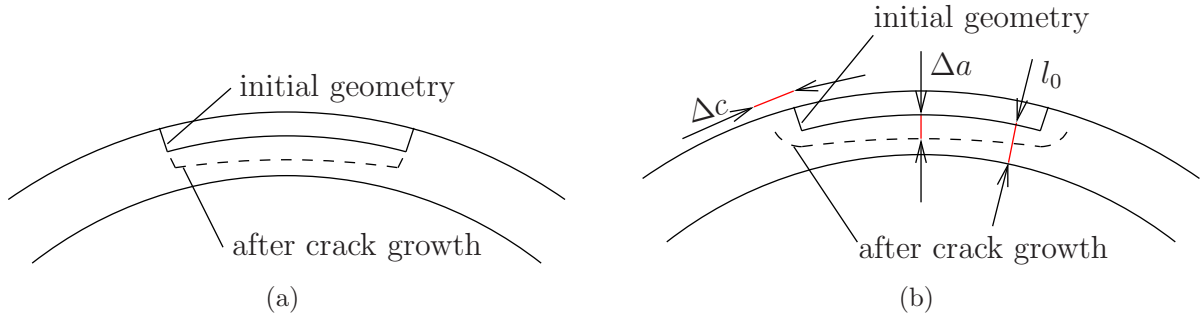


Figure 2.13: Crack growth behaviour of a surface crack subjected to loading. (a) gives a schematic view of the previous implementation where only crack growth in the thickness direction was accounted for, and (b) shows principles in the improved implementation of the crack growth.

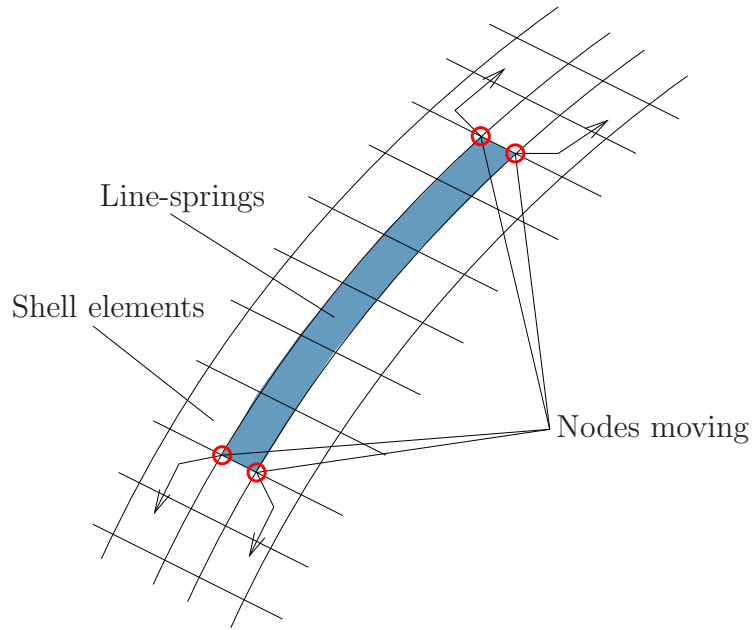


Figure 2.14: Schematic view of the method used to model circumferential crack growth.

The abscissa axis in Fig. 2.15 is the ratio of crack depth ( $a$ ) to the initial ligament ( $l$ ), where the ordinate axis is the ratio of circumferential crack growth to initial ligament. See Fig. 2.13b for detailed view of the dimensions. In Fig. 2.15 the “+” are results from 81 3D-analyses, employing the Gurson-Tvergaard damage model (see [37] for details) of pipes subjected to various internal pressure and pure tensile loading. The dashed trend line is a best fit interpolation of the points, and this curve is implemented in  $\text{LINK}_{\text{pipe}}$ , i.e. defining Eq. 2.79.

Due to difference in crack depth along the crack front, the constraint will also have influence on the circumferential crack growth. When the crack length increases, the cracked section becomes softer compared to the global geometry, hence the crack growth at the deepest point of the crack will increase faster, resulting in modification of constraint. This effect is automatically taken into account when performing constraint correction of the crack growth resistance curve for all time increments.

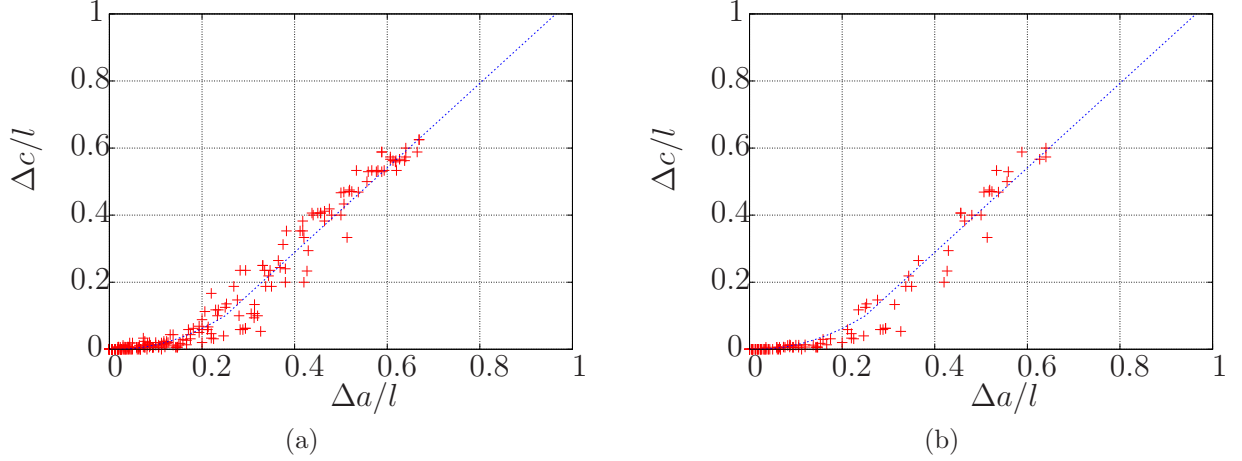


Figure 2.15: Crack growth data from 3D-analyses performed by [37] (+), and dotted line is the trend-line. (a) shows all the 81 3D-analyses and (b) shows only those with no internal pressure.  $a$  is the crack depth,  $c$  is the half crack length and  $l$  is the initial ligament size.

### 2.1.10 Residual stress

A methodology to account for residual stress in  $\text{LINK}_{\text{pipe}}$  is implemented for the line-spring element only. The residual stress reduces the elastic capacity of the cross section area, i.e. yielding occurs at loads below the yield limit compared to a corresponding structure without residual stress. The conventional approach is to apply the strain level at the onset of nominal yielding. This approach does not work for  $\text{LINK}_{\text{pipe}}$ . Therefore an alternative approach was chosen where the residual stress contributes to the crack tip opening displacement.

Relaxation of the residual stress is also accounted for using the methodology presented in section 7.3.4.2 in British standard BS7910 2005 [9].

#### 2.1.10.1 Implementation of relaxation of residual stress

Before the load incrementation initiates, the  $CTOD$  at the onset of yielding for the deepest point of the crack is computed based on geometric assumptions where only the membrane force in the ligament is taken into account.

An assumed  $CTOD$  at the onset of ligament yielding (denoted  $CTOD_{res}$ ) is found based on the crack geometry and material properties.  $CTOD_{res}$  is computed based on the assumption of a pure membrane situation (see Eq. 2.82). Based on this assumption  $CTOD_{res}$  can be computed before the load history starts.  $CTOD_{res}$  is computed the same way as the elastic  $CTOD$ , thus a stress intensity factor (see Eq. 2.30) is needed. Since the bending mode is neglected, the membrane force at crossing of the yield surface is used in the stress intensity factor.  $CTOD_{res}$  is computed as

$$\delta_{res} = d_n \frac{[K_I(N, M = 0, a, t, E, \nu)]^2}{\sigma_0 E} \quad (2.82)$$

where  $d_n$  is a scaling factor depending on the load condition and material properties (see e.g. Anderson [2]).  $a$  and  $t$  are the crack depth and wall thickness while  $N$  and  $M$  are the ligament forces.  $E$  and  $\nu$  are the elastic material properties, Young's modulus and Poisson's ratio respectively.  $\sigma_0$  is the yield stress.

The membrane force in the ligament at the onset of yielding in the line-spring element is found by computing the crossing point on the yield surface along the  $N$ -axis for the current crack depth to thickness ratio (see Berg et al. [4] for more details about the yield surface of the line-spring element). Zero bending moment in the line-spring element is chosen for simplicity since the load path for the element is unknown prior to the load incrementation. Investigations of this aspect is performed. In the application range of pipe lines, a membrane stress state in the pipe wall is dominant. An increasing membrane force in the line-spring element will result in a smaller bending moment. This bending moment can be less than zero, reducing the stress intensity factor used in the computation of the elastic  $CTOD$  (see Eqs. 2.82-2.83). The  $CTOD$ -contribution from Eq. 2.82 will decrease with increasing negative bending moment or decreasing membrane force. The simple computation with zero bending moment gives the largest (most conservative) contribution for the residual stress in  $LINK_{pipe}$ . Since only the membrane part is taken into account, the bending contribution to  $K_I$  vanishes.

$CTOD_{res}$  from Eq. 2.82 is now stored as a permanent value throughout the analysis. When it is used in the computations of the total  $CTOD$ , it is multiplied with a ratio between the residual stress ( $\sigma_{res}$ ) and the yield stress ( $\sigma_0$ ). This way it can also handle relaxation in residual stress as  $\sigma_{res}$  can decrease as plasticity evolves. The total  $CTOD$  is then expressed as

$$\delta_{tot} = \delta_{el} + \delta_{res} \frac{\sigma_{res}}{\sigma_0} + \delta_{pl} \quad (2.83)$$

$\sigma_{res}$  is computed from the nominal stress value at the maximum tension side of the pipe at a distance of one outer diameter from the crack zone. This nominal stress value is found from an integration point in a shell element for each equilibrium state throughout the analysis.

The relaxation of the residual stress,  $\sigma_{res}$ , in Eq. 2.83 follows the procedure described in Sec. 7.3.4.2 in British Standard BS7910 [9] as expressed in Eq. 2.84.

$$\sigma_{res} = \min \begin{cases} \sigma_0 \\ \sigma_0 \left( 1.4 - \frac{\sigma_{ref}}{\sigma_f} \right) \end{cases} \quad (2.84)$$

where the nominal stress value in the pipe body at maximum tension is used as  $\sigma_{ref}$ .  $\sigma_f$  is described as the mean value of the material's yield stress and the tensile strength.

A lower threshold for the relaxation of  $\sigma_{res}$  when  $\sigma_{ref}$  equals  $\sigma_f$  is also applied, giving a threshold for  $\sigma_{res}$  of  $0.4\sigma_0$ .

### 2.1.11 Different materials

A simplified approach to account for material mismatch in the line-spring finite element is implemented in  $LINK_{pipe}$ . Input data are the stress-strain curves for the different materials. Fig. 2.16 shows a schematic setup where base material, weld metal and clad material are present. It is assumed that the strain localisation in the ligament follows a  $45^\circ$  line from the crack tip towards the opposite surface.

Based on the assumptions in Fig. 2.16, a weight function is used to compute an equivalent stress-strain curve which should be assigned to the line-spring element. The weight function is expressed as

$$\sigma_{eff}(\varepsilon_{pl}) = (1 - x - y)\sigma_{BM}(\varepsilon_{pl}) + x\sigma_{WM}(\varepsilon_{pl}) + y\sigma_{clad}(\varepsilon_{pl}) \quad (2.85)$$

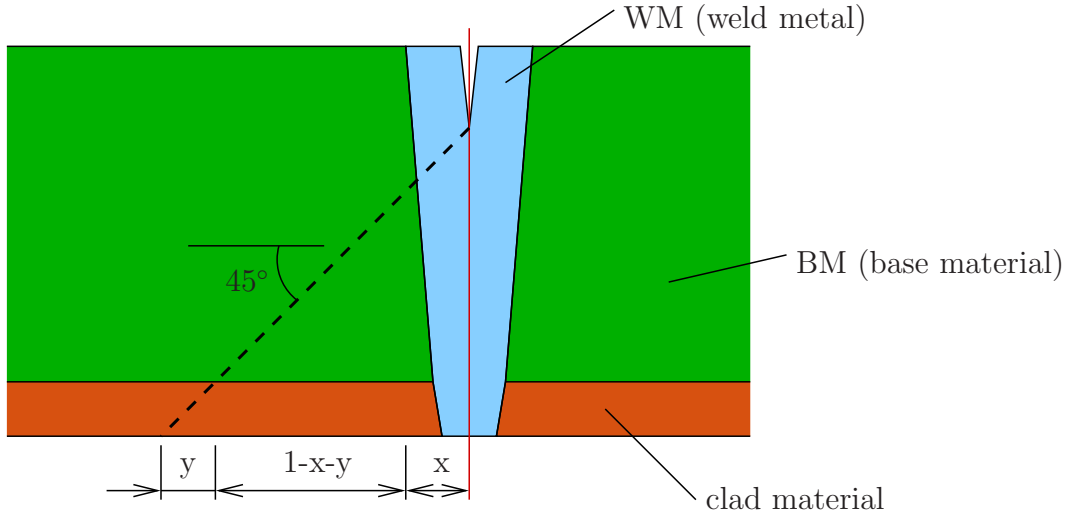


Figure 2.16: Weld geometry and different materials

### 2.1.12 Split line-spring - another mismatch approach

An extended version of the line-spring element, the so-called split “line-spring element” was implemented to account for material mismatch. The element is divided into a left and a right side where the two sides can have different material properties. An internal set of degrees of freedom must be included in the equilibrium equations in the element. The internal degrees of freedom are not exposed to the main program as they should not contribute to any energy dissipation or production. To avoid this, a static condensation is applied to remove the effect of the internal degrees of freedom.

The concept is illustrated in Fig. 2.17 where two half line-spring elements are merged into a split line-spring element.

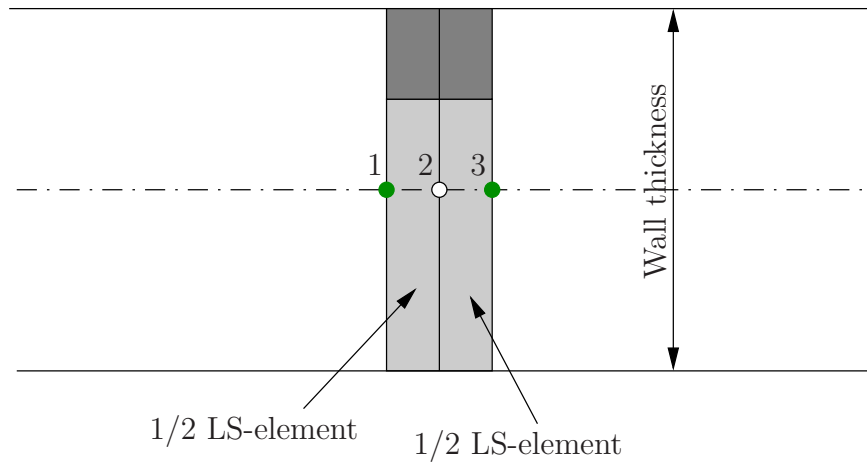


Figure 2.17: Two half line-spring elements are merged into a split line-spring element

The two external nodes in Fig. 2.17 are known to the main program as nodes from the input file, whereas node 2 is an internal node which is a local node in the element formulation. This internal node is unknown to the main program.

The total deformation to the split line-spring element is shared by the two line-spring ele-

ments in the split line-spring element. A pragmatic solution which is implemented is to let the stiffness of the two line-spring elements be of double magnitude compared to a conventional line-spring element as expressed in Eq. 2.86:

$$\begin{bmatrix} \Delta \bar{\mathbf{Q}}_1 \\ \Delta \bar{\mathbf{Q}}_2 \end{bmatrix} = 2 \begin{bmatrix} \mathbf{k}_{11} & \mathbf{k}_{12} \\ \mathbf{k}_{21} & \mathbf{k}_{22} \end{bmatrix} \begin{bmatrix} \Delta \bar{\mathbf{q}}_1 \\ \Delta \bar{\mathbf{q}}_2 \end{bmatrix} \quad (2.86)$$

In general unbalanced forces between the two internal line-spring elements will exist. Fig. 2.18 and Eq. 2.87 express the unbalance equation:

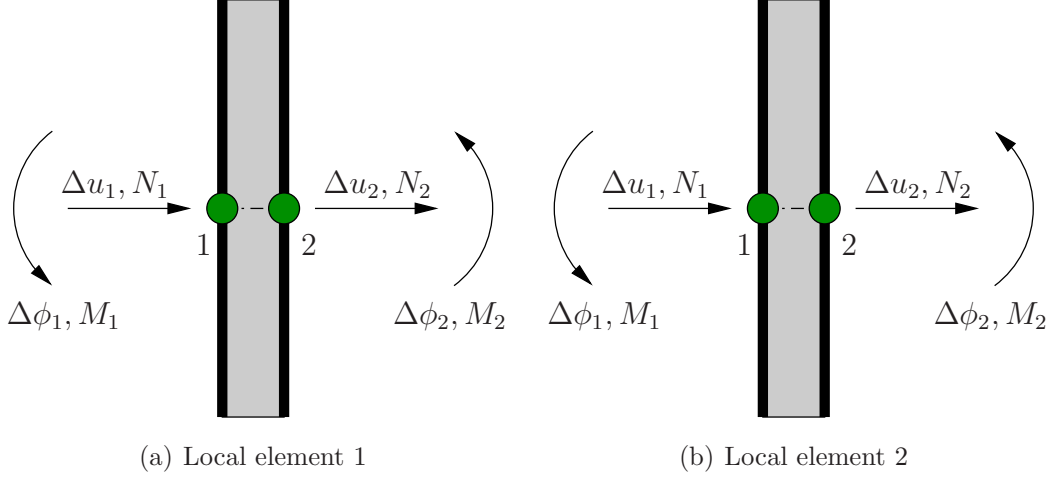


Figure 2.18: Internal and external degrees of freedom for the two line-spring elements in a split line-spring formulation

$$\Delta \bar{\mathbf{Q}}_2 = \bar{\mathbf{Q}}_{2,1} + \bar{\mathbf{Q}}_{1,2} = \begin{bmatrix} N_1 - N_2 \\ -M_1 + M_2 \end{bmatrix} \quad (2.87)$$

where  $N_1 = N_2$  and  $M_1 = M_2$  at equilibrium, giving  $\Delta \bar{\mathbf{Q}}_2 = 0$ . The indexes in Eq. 2.87 refer to both node number and element number in Fig. 2.18.  $\bar{\mathbf{Q}}_{2,1}$  refers to the forces in node 2 in local element 1.

The sum of the incremental stiffness relations for the half line-spring element 1-2 (element 1) and the half line-spring element 2-3 (element 2) gives:

$$2 \begin{bmatrix} \mathbf{k}_{11,1} & \mathbf{k}_{12,1} & \mathbf{0} \\ \mathbf{k}_{21,1} & \mathbf{k}_{22,1} + \mathbf{k}_{11,2} & \mathbf{k}_{12,2} \\ \mathbf{0} & \mathbf{k}_{21,2} & \mathbf{k}_{22,2} \end{bmatrix} \begin{bmatrix} \Delta \bar{\mathbf{q}}_1 \\ \Delta \bar{\mathbf{q}}_2 \\ \Delta \bar{\mathbf{q}}_3 \end{bmatrix} = \begin{bmatrix} \Delta \bar{\mathbf{Q}}_1 \\ \Delta \bar{\mathbf{Q}}_2 \\ \Delta \bar{\mathbf{Q}}_3 \end{bmatrix} = \begin{bmatrix} \Delta \bar{\mathbf{Q}}_{1,1} \\ -(\Delta \bar{\mathbf{Q}}_{2,1} + \Delta \bar{\mathbf{Q}}_{1,2}) \\ \Delta \bar{\mathbf{Q}}_{2,2} \end{bmatrix} \quad (2.88)$$

Static condensation is applied to eliminate the degrees of freedom in the internal node ( $\Delta \bar{\mathbf{q}}_2$ ) by refactoring the second equation in Eq. 2.88 as

$$\Delta \bar{\mathbf{q}}_2 = -(\mathbf{k}_{22,1} + \mathbf{k}_{11,2})^{-1} \left[ \frac{1}{2}(\bar{\mathbf{Q}}_{2,1} + \bar{\mathbf{Q}}_{1,2}) + \mathbf{k}_{21,1} \Delta \bar{\mathbf{q}}_1 + \mathbf{k}_{12,2} \Delta \bar{\mathbf{q}}_3 \right] \quad (2.89)$$

Using the result from Eq. 2.89, the displacements in the internal node (from Fig. 2.17) are eliminated and the equation system is expressed as

$$\begin{aligned} 2 \begin{bmatrix} \mathbf{k}_{11,1} - \mathbf{k}_{12,1}(\mathbf{k}_{22,1} + \mathbf{k}_{11,2})^{-1} \mathbf{k}_{21,1} & -\mathbf{k}_{12,1}(\mathbf{k}_{22,1} + \mathbf{k}_{11,2})^{-1} \mathbf{k}_{12,2} \\ -\mathbf{k}_{21,2}(\mathbf{k}_{22,1} + \mathbf{k}_{11,2})^{-1} \mathbf{k}_{21,1} & \mathbf{k}_{22,2} - \mathbf{k}_{21,2}(\mathbf{k}_{22,1} + \mathbf{k}_{11,2})^{-1} \mathbf{k}_{12,2} \end{bmatrix} \begin{bmatrix} \Delta \bar{\mathbf{q}}_1 \\ \Delta \bar{\mathbf{q}}_3 \end{bmatrix} \\ = \begin{bmatrix} \Delta \bar{\mathbf{Q}}_{1,1} \\ \Delta \bar{\mathbf{Q}}_{2,2} \end{bmatrix} + \begin{bmatrix} \mathbf{k}_{12,1}(\mathbf{k}_{22,1} + \mathbf{k}_{11,2})^{-1}(\bar{\mathbf{Q}}_{2,1} + \bar{\mathbf{Q}}_{1,2}) \\ \mathbf{k}_{21,2}(\mathbf{k}_{22,1} + \mathbf{k}_{11,2})^{-1}(\bar{\mathbf{Q}}_{2,1} + \bar{\mathbf{Q}}_{1,2}) \end{bmatrix} \end{aligned} \quad (2.90)$$

The crack tip opening displacement for the split line-spring will consist of two parts, one contribution from each side of the crack centerline. The contributions are summed in the result files, giving the total crack tip opening displacement in the post processors.

### 2.1.13 Embedded defects

Embedded defects in  $\text{LINK}_{pipe}$  are implemented as double surface cracks, see Fig. 2.19. The

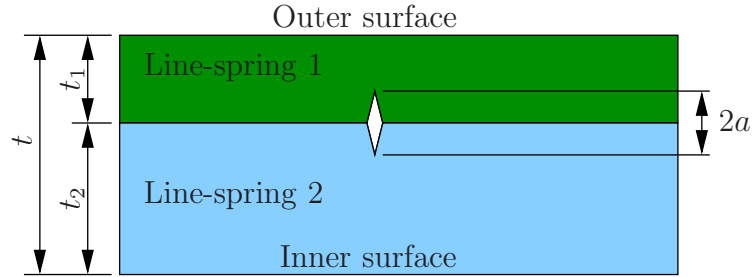


Figure 2.19: Embedded defect approach in  $\text{LINK}_{pipe}$

two line-spring elements in the formulation are two individual conventional line-spring elements. They are connected to the shell elements using linear couplings (multi point constraint) as shown in Fig. 2.20. Ductile tearing for this concept equals the sum of the ductile

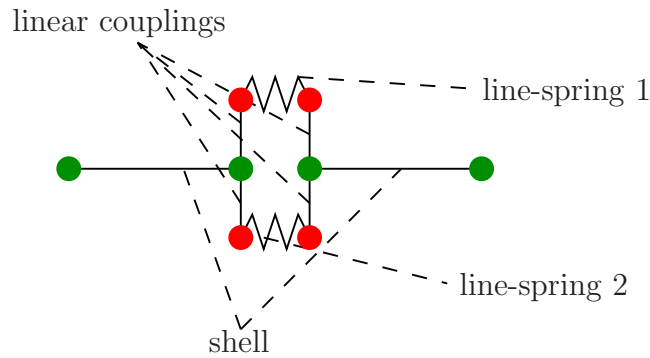


Figure 2.20: The line-spring elements are connected to the shell elements using linear couplings

crack growth from each line-spring element in the embedded pair. Each line-spring element contributes separately to the crack growth as the crack tip opening displacement will in general be different for each line-spring element in the embedded pair.

## 2.2 Shell finite element

The shell finite element used in  $\text{LINK}_{pipe}$  is an Assumed Natural Deviatoric Strains shell element denoted ANDES.

### 2.2.1 Linear shell finite element

The 4-node ANDES shell element is developed as a flat element with decoupled membrane and bending behaviour. The element stiffness for the ANDES element is the sum of the basic and higher order stiffness contributions

$$\mathbf{K} = \mathbf{K}_b + \mathbf{K}_h = \frac{1}{A} \mathbf{LCL}^T + \int_A \mathbf{B}^T \mathbf{CB} dA \quad (2.91)$$

#### 2.2.1.1 The membrane element

Nygård [30] developed a 4-node membrane element with drilling degrees of freedom based on the Free Formulation, called the FFQ element. The element gives accurate results for plane membrane problems, but is computationally expensive due to a numerical inversion of a  $12 \times 12$  matrix. The present element was developed based on the ANDES formulation in order to avoid the expensive matrix inversion.

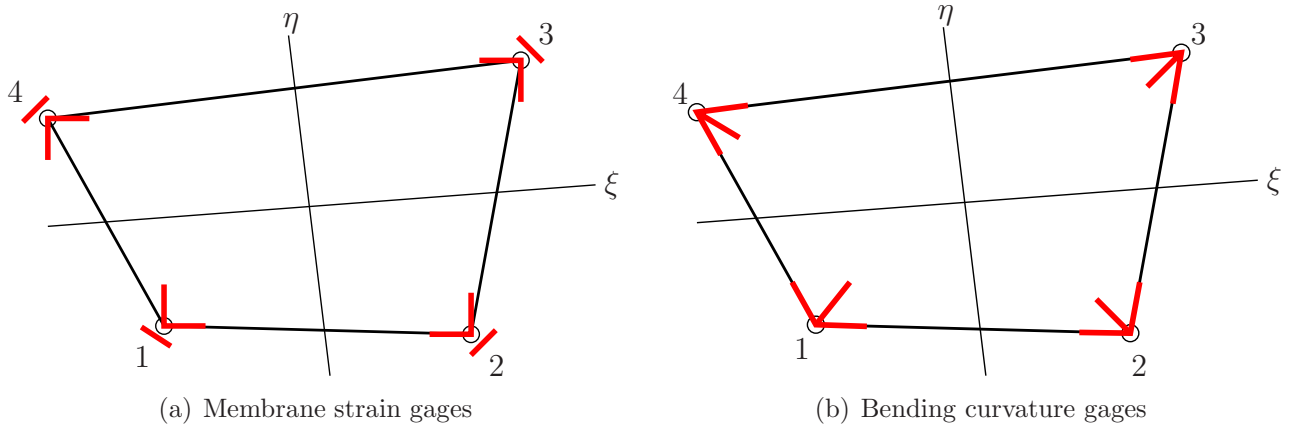


Figure 2.21: Nodal strain gages

#### Membrane basic stiffness

A very successful lumping scheme for membrane stresses was first introduced by Bergan and Felippa [6], and since used by Nygård [30] and Militello [28]. With a nodal degree of freedom ordering for  $\mathbf{v}_{mi} = [u \ v \ \theta_z]$  the lumping matrix can be written as

$$\mathbf{L} = \begin{bmatrix} \mathbf{L}_1 \\ \mathbf{L}_2 \\ \mathbf{L}_3 \\ \mathbf{L}_4 \end{bmatrix} \quad \text{where} \quad \mathbf{L}_j = \frac{1}{2} \begin{bmatrix} y_{ki} & 0 & -x_{ki} \\ 0 & -x_{ki} & y_{ki} \\ \frac{\alpha}{6}(y_{ij}^2 - y_{kj}^2) & \frac{\alpha}{6}(x_{ij}^2 - x_{kj}^2) & \frac{\alpha}{3}(x_{kj}y_{kj} - x_{ij}y_{ij}) \end{bmatrix} \quad (2.92)$$

The nodal indices  $(i, j, k, l)$  undergo cyclic permutations of  $(1, 2, 3, 4)$  in the equation above. One has also used the notation  $x_{ij} = x_i - x_j$ . Factor  $\alpha$  represents a scaling of the contributions of the drilling freedom to the normal boundary displacements, see Bergan and Felippa [6] for details.

### Membrane higher order stiffness

The distribution of higher order strain is expressed in terms of natural strain gauge readings as function of the higher order degrees of freedom

$$\tilde{\mathbf{v}}^T = [ \theta'_1 \quad \theta'_2 \quad \theta'_3 \quad \theta'_4 \quad \bar{\theta} \quad \alpha_1 \quad \alpha_2 ] \quad (2.93)$$

where  $\theta'_i$  are deviatoric nodal rotations,  $\bar{\theta}$  is mean nodal rotation, and  $\alpha_1$  and  $\alpha_2$  are higher order modes described by the translational degrees of freedom.

Strain gages are located at the nodes, in the two median direction ( $\xi$  and  $\eta$ ) as well as the direction of the diagonal through the neighbouring nodes. For node 1 the template for the strain gauge readings is

$$\mathbf{Q}_1 = \begin{bmatrix} \rho_1 \chi_{\xi|1} & \rho_2 \chi_{\xi|1} & \rho_3 \chi_{\xi|1} & \rho_4 \chi_{\xi|1} & \alpha \chi_{\xi t} & -\beta_1 \frac{\chi_{\xi|1}}{\bar{\chi}_{\xi} l_{\xi}} & 0 \\ -\rho_1 \chi_{\eta|1} & -\rho_4 \chi_{\eta|1} & -\rho_3 \chi_{\eta|1} & -\rho_2 \chi_{\eta|1} & -\alpha \chi_{\eta t} & 0 & -\beta_1 \frac{\chi_{\eta|1}}{\bar{\chi}_{\eta} l_{\eta}} \\ \rho_5 \chi_{24} & \rho_6 \chi_{24} & \rho_7 \chi_{24} & \rho_8 \chi_{24} & 0 & \beta_2 \frac{c_{24\xi}}{l_{24}} & -\beta_2 \frac{c_{24\xi}}{l_{24}} \end{bmatrix} \quad (2.94)$$

where  $c_{13\xi} = \mathbf{s}_{13}^T \mathbf{s}_{\xi}$ ,  $c_{13\eta} = \mathbf{s}_{13}^T \mathbf{s}_{\eta}$ ,  $c_{24\xi} = \mathbf{s}_{24}^T \mathbf{s}_{\xi}$  and  $c_{24\eta} = \mathbf{s}_{24}^T \mathbf{s}_{\eta}$ .

$\chi_{\xi|i} = \frac{d_{\xi|i}}{l_{\xi}}$  and  $\chi_{\eta|i} = \frac{d_{\eta|i}}{l_{\eta}}$  where  $d_{\xi|i}$  and  $d_{\eta|i}$  are distances from node  $i$  to median lines  $\xi$  and  $\eta$ .  $l_{\xi}$  and  $l_{\eta}$  are lengths of median lines  $\xi$  and  $\eta$ .  $\bar{\chi}_{\xi} = \frac{1}{4} \sum_{i=1}^4 \chi_{\xi|i}$  and  $\bar{\chi}_{\eta} = \frac{1}{4} \sum_{i=1}^4 \chi_{\eta|i}$ . E.g.  $\mathbf{s}_{13}$  is the unit direction vector along side 13,  $\mathbf{s}_{\xi}$  is unit vector in  $\xi$ -direction etc.  $\mathbf{Q}_2$ ,  $\mathbf{Q}_3$  and  $\mathbf{Q}_4$  can be established by permutations of the expression above. The Cartesian strain displacement relationship at each node is established by transformation of the strain gauge strains. Based on symbolic evaluation of pure bending of the element one has chosen the following set of parameters:  $\rho_1 = 0.1$ ,  $\rho_2 = -0.1$ ,  $\rho_3 = -0.1$ ,  $\rho_4 = 0.1$ ,  $\rho_5 = 0$ ,  $\rho_6 = 0.5$ ,  $\rho_7 = 0$ ,  $\rho_8 = -0.5$ ,  $\beta_1 = 0.6$ ,  $\beta_2 = 0$ .

#### 2.2.1.2 The bending element

The present element is a Kirchhoff type plate element utilising reference lines to model the plate bending behaviour. Hrennikoff [18] first used this concept for modelling bending of flat plates. Park and Stanley [33] used this concept for developing several plate and shell elements based on the Assumed Natural-coordinate Strains formulation, ANS.

### Bending basic stiffness

The basic stiffness for the quadrilateral bending element has been developed by extending the triangle element lumping matrices of Militello to four nodes. Militello developed expressions for both linear and quadratic normal rotation. Expression given here use the quadratic normal rotation interpolation. With a nodal degree of freedom ordering for  $\mathbf{v}_{bi} = [ w \quad \theta_x \quad \theta_y ]$



the lumping matrix can be written as

$$\mathbf{L} = \begin{bmatrix} \mathbf{L}_1 \\ \mathbf{L}_2 \\ \mathbf{L}_3 \\ \mathbf{L}_4 \end{bmatrix} \quad (2.95)$$

where

$$\mathbf{L}_j = \frac{1}{2} \begin{bmatrix} -c_{jk}s_{jk} + c_{ij}s_{ij} & c_{jk}s_{jk} - c_{ij}s_{ij} & -(s_{jk}^2 - c_{jk}^2) + (s_{ij}^2 + s_{ij}^2) \\ \frac{\alpha}{2}(s_{jk}^2 x_{jk} - s_{ij}^2 x_{ij}) & \frac{\alpha}{2}(c_{jk}^2 x_{jk} - c_{ij}^2 x_{ij}) & -s_{jk}^2 y_{jk} - s_{ij}^2 y_{ij} \\ \frac{\alpha}{2}(s_{jk}^2 y_{jk} - s_{ij}^2 y_{ij}) & \frac{\alpha}{2}(c_{jk}^2 y_{jk} - c_{ij}^2 y_{ij}) & -s_{jk}^2 x_{jk} - s_{ij}^2 x_{ij} \end{bmatrix} \quad (2.96)$$

The nodal indices  $(i, j, k, l)$  undergo cyclic permutations of  $(1, 2, 3, 4)$  in the equation above. One has also used the notation  $x_{ij} = x_i - x_j$ .  $c_{ij}$  and  $s_{ij}$  are cosine and sine of side  $ij$  angle with respect to  $x$ -axis etc. Factor  $\alpha$  represents a scaling of the contributions of the drilling freedom to the normal boundary displacements, see Bergan and Felippa [6] for details.

### Bending higher order stiffness

The higher order bending stiffness is computed as the deviatoric part of an ANS type element with nodal strain gages along element reference lines. The reference lines are the element edges and diagonals, giving a total of 12 curvature gages.

The nodal curvature of a Euler-Bernoulli beam from node  $i$  to  $j$  can be shown to be

$$\begin{bmatrix} \kappa_{ij|i} \\ \kappa_{ij|j} \end{bmatrix} = \frac{1}{l_{ij}^2} \begin{bmatrix} -6 & -4l_{ij} & 6 & -2l_{ij} \\ 6 & -2l_{ij} & -6 & 4l_{ij} \end{bmatrix} \begin{bmatrix} w_i & \theta_{ni} & w_j & \theta_{nj} \end{bmatrix}^T \quad (2.97)$$

Here,  $l_{ij}$  is length of side  $ij$ . By appropriately transforming the curvature readings from all three reference directions at a node to the Cartesian curvatures, and similarly transforming from Cartesian rotational degrees of freedom to the reference line normal rotation, one can establish the curvature relationship at a node as

$$\boldsymbol{\kappa}_i = \mathbf{B}_i \mathbf{v} \quad (2.98)$$

and the assumed curvature distribution is obtained by linear interpolation over the element domain.

The ANDES higher order bending is then computed using the deviatoric part of the curvature displacement relationship

$$\mathbf{K}_d = \int_A \mathbf{B}_d \mathbf{C}_d \mathbf{B}_d^T dA \quad \text{where} \quad \mathbf{B}_d = \mathbf{B} - \frac{1}{A} \int_A \mathbf{B} dA \quad (2.99)$$

### 2.2.2 Co-rotated shell element

Fig. 2.22 shows the two basic coordinate systems that are used. The global coordinate system is represented by unit vectors  $\mathbf{I}_1$ ,  $\mathbf{I}_2$  and  $\mathbf{I}_3$ . The co-rotated element coordinate system shared

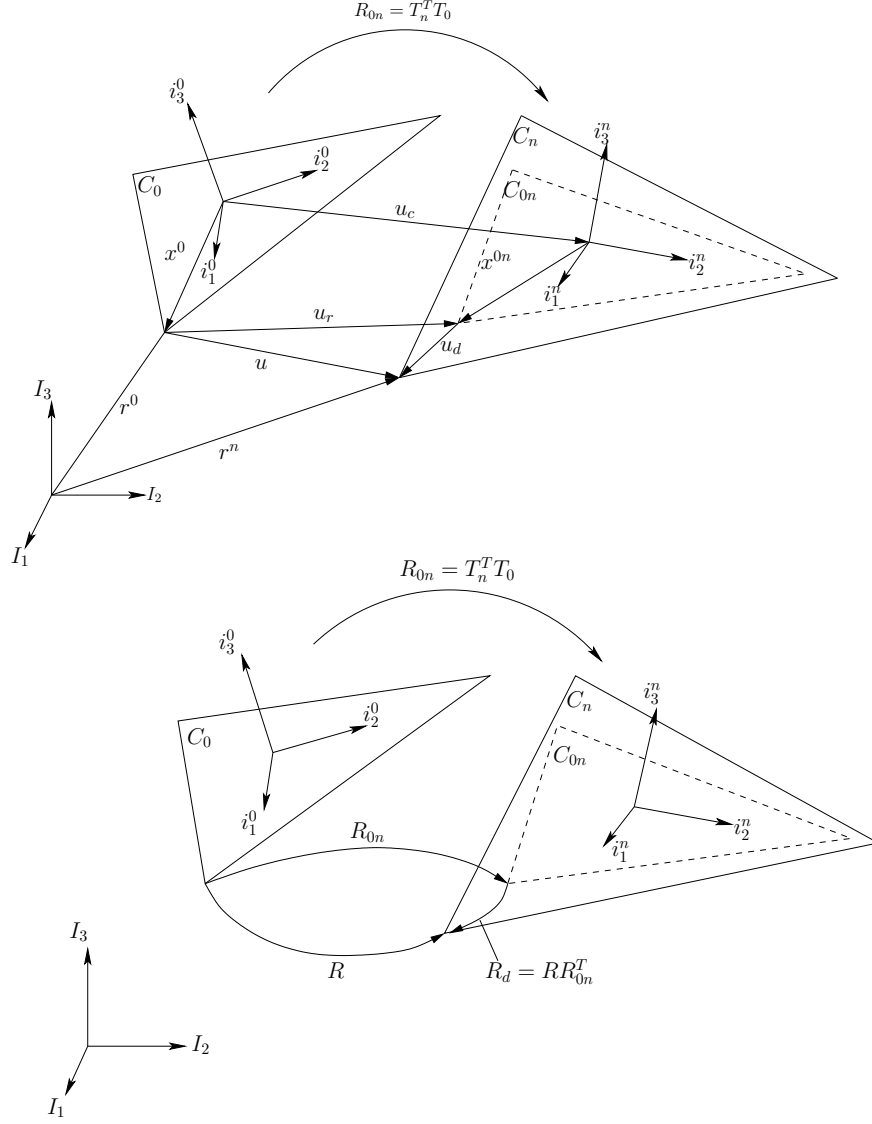


Figure 2.22: Co-rotated thin shell kinematics (a triangular element is used for illustration)

by shadow configuration  $C_{0n}$  and configuration  $C_n$  is represented by unit vectors  $\mathbf{i}_1^n$ ,  $\mathbf{i}_2^n$  and  $\mathbf{i}_3^n$ .

Vectors given in the local co-rotated element coordinate system are marked with a tilde( $\sim$ ). A vector  $\mathbf{x}$  in global coordinates is transformed into a vector  $\tilde{\mathbf{x}}$  in the local coordinate system  $0$  by

$$\tilde{\mathbf{x}} = \mathbf{T}_0 \mathbf{x} \quad \mathbf{T}_0 = \begin{bmatrix} \mathbf{i}_1^{0T} \\ \mathbf{i}_2^{0T} \\ \mathbf{i}_3^{0T} \end{bmatrix} \quad (2.100)$$

$\mathbf{T}_0$  is orthonormal. The rigid body rotation of  $\mathbf{i}_i^0$  to  $\mathbf{i}_i^n$  is given by

$$\mathbf{i}_1^n = \mathbf{R}_{0n} \mathbf{i}_1^0 \quad \mathbf{R}_{0n} = \mathbf{T}_n^T \mathbf{T}_0 \quad (2.101)$$

where  $\mathbf{R}_{0n}$  is the rigid body rotation matrix from position  $0$  to position  $n$ . The Rodrigues representation of the rotation matrix is used. The rotation matrix for a rotation  $\theta$  about an axis defined by the unit vector  $\mathbf{n}^T = [n_1 \ n_2 \ n_3]$  is written (see Nour-Omid and Rankin [29]):

$$\mathbf{R} = \mathbf{I} + \mathbf{N} \sin \theta + \mathbf{N}^2 (1 - \cos \theta) \quad (2.102)$$

$$\mathbf{N} = \mathbf{Spin}(\mathbf{n}) = \begin{bmatrix} 0 & -n_3 & n_2 \\ n_3 & 0 & -n_1 \\ -n_2 & n_1 & 0 \end{bmatrix}$$

$\mathbf{I}$  is the 3 by 3 identity matrix. Rotation of a vector  $\mathbf{r}_0$  into  $\mathbf{r}$  through an angle  $\theta$  about an axis defined by the unit vector  $\mathbf{n}$  is obtained by:

$$\mathbf{r} = \mathbf{R}\mathbf{r}_0 \quad (2.103)$$

The displacement vector is given as the difference between the position vector in configuration  $C_0$  and the position vector in configuration  $C_n$ .

$$\mathbf{u} = \mathbf{r}^n - \mathbf{r}^0 \quad (2.104)$$

The displacement vector is split into a deformational displacement vector and a rigid body displacement vector.

$$\mathbf{u} = \mathbf{u}_r + \mathbf{u}_d \quad \mathbf{u}_r = \mathbf{r}^{0n} - \mathbf{r}^0 \quad \mathbf{u}_d = \mathbf{r}^n - \mathbf{r}^{0n} \quad (2.105)$$

Introducing subscript  $c$  for the arithmetic mean of the coordinates of the points in the element, the position vectors in initial and shadow element configurations may be written as:

$$\mathbf{r}^0 = \mathbf{r}_c^0 + \mathbf{x}^0 \quad (2.106)$$

$$\mathbf{r}^{0n} = \mathbf{r}_c^{0n} + \mathbf{x}^{0n} = \mathbf{r}_c^0 + \mathbf{u}_c + \mathbf{R}_{0n}\mathbf{x}^0 \quad (2.107)$$

where  $\mathbf{x}^0$  and  $\mathbf{x}^{0n}$  are the vectors from the centroid of the element to the point being considered in the  $C_0$  configuration and the  $C_{0n}$  configuration respectively. Substitution of the expressions 2.106 and 2.107 into Eq. 2.105 yields:

$$\mathbf{u}_d = \mathbf{u} - \mathbf{u}_r = \mathbf{u} - (\mathbf{r}^{0n} - \mathbf{r}^0) = \mathbf{u} - \mathbf{u}_c - (\mathbf{R}_{0n} - \mathbf{I})\mathbf{x}^0 \quad (2.108)$$

The rotation of an element node as it moves from the initial configuration  $C_0$  to the deformed configuration  $C_n$  is described by the rotation matrix  $\mathbf{R}$ . The rotation matrix is split into a rigid body rotation  $\mathbf{R}_{0n}$  and a deformational rotation  $\mathbf{R}_d$ .

$$\mathbf{R} = \mathbf{R}_d \mathbf{R}_{0n} \quad (2.109)$$

$$\mathbf{R}_d = \mathbf{R} \mathbf{R}_{0n}^T = \mathbf{R} \mathbf{T}_0^T \mathbf{T}_n \quad (2.110)$$

The deformational rotation matrix transformed into the local coordinate system shared by configurations  $C_{0n}$  and  $C_n$  reads

$$\tilde{\mathbf{R}}_d = \mathbf{T}_n \mathbf{R}_d \mathbf{T}_n^T = \mathbf{T}_n \mathbf{R} \mathbf{T}_0^T \quad (2.111)$$

The position of an element node  $a$  with initial coordinates  $\mathbf{r}_a^0$ , is defined by the translational displacement  $\mathbf{u}_a$  and the rotational orientation  $\mathbf{R}_a$ . Together, the set  $(\mathbf{u}_a, \mathbf{R}_a)$  for  $a = 1, \dots, N$  is the nodal displacement vector  $\hat{\mathbf{v}}$ .  $\hat{\mathbf{v}}$  is interpreted as an array of numbers that defines the position of the deformed element. In order to establish the force vector and tangent stiffness for an element, the *deformational* vector for the element needs to be established. This vector is denoted  $\tilde{\mathbf{v}}_d$  and contains translational and rotational degrees of freedom for each element node ordered as

$$\tilde{\mathbf{v}}_d^T = [\tilde{\mathbf{u}}_{d1}^T \tilde{\boldsymbol{\theta}}_{d1}^T \dots \tilde{\mathbf{u}}_{dN}^T \tilde{\boldsymbol{\theta}}_{dN}^T] \quad (2.112)$$

$N$  is the number of element nodes for the element being considered.  $\tilde{\boldsymbol{\theta}}_d$  is obtained from  $\tilde{\mathbf{R}}_d$ .

### 2.2.2.1 Equilibrium and tangent stiffness

Virtual work is employed as weak form of the equilibrium equations:

$$\begin{aligned}\delta_R \tilde{\mathbf{v}}_d^T \tilde{\mathbf{f}}_e - \delta \mathbf{v}^T \mathbf{f}_{ext} &= \delta \mathbf{v}^T \left( \frac{\partial_R \mathbf{v}_d}{\partial \mathbf{v}} \right)^T \mathbf{f}_e - \mathbf{f}_{ext} = 0 \\ \Rightarrow \mathbf{f}_e &= \mathbf{T}^T \tilde{\mathbf{P}}^T \tilde{\mathbf{H}}^T \tilde{\mathbf{f}}_e = \mathbf{f}_{ext}\end{aligned}\quad (2.113)$$

The transformations are matrices accounting for large rigid body translations and rotations, and are explained briefly in the following, see [43] for details. First, the variation of the transformation matrix with respect to infinitesimal rotations about the local coordinate axes reads:

$$\delta \mathbf{T}_n = \frac{\partial \mathbf{T}_n}{\partial \tilde{\omega}_i} \delta \tilde{\omega}_i = \begin{bmatrix} 0 & \delta \tilde{\omega}_z & -\delta \tilde{\omega}_y \\ -\delta \tilde{\omega}_z & 0 & \delta \tilde{\omega}_x \\ \delta \tilde{\omega}_y & -\delta \tilde{\omega}_x & 0 \end{bmatrix} \begin{bmatrix} \mathbf{i}_1^{nT} \\ \mathbf{i}_2^{nT} \\ \mathbf{i}_3^{nT} \end{bmatrix} = -\mathbf{Spin}(\delta \tilde{\omega}) \mathbf{T}_n \quad (2.114)$$

Transformation of  $\mathbf{Spin}(\delta \tilde{\omega})$  to global coordinates reads

$$\delta \mathbf{T}_n = -\mathbf{Spin}(\delta \tilde{\omega}) \mathbf{T}_n = -\mathbf{T}_n \mathbf{Spin}(\delta \omega) \mathbf{T}_n^T \mathbf{T}_n = -\mathbf{T}_n \mathbf{Spin}(\delta \omega) \quad (2.115)$$

Secondly, the rotation matrix  $\mathbf{R}_{0n}$  rotates a vector from initial configuration to the shadow configuration, hence the variation of the rotation matrix reads

Secondly, the rotation matrix  $\mathbf{R}_{0n}$  rotates a vector from initial configuration to the shadow configuration, hence the variation of the rotation matrix reads

$$\delta \mathbf{R}_{0n} = \delta \mathbf{T}_n^T \mathbf{T}_0 + \mathbf{T}_n^T \delta \mathbf{T}_0 = \delta \mathbf{T}_n^T \mathbf{T}_0 = \mathbf{Spin}(\delta \omega) \mathbf{T}_n^T \mathbf{T}_0 = \mathbf{Spin}(\delta \omega) \mathbf{R}_{0n} \quad (2.116)$$

The variation of a vector expressed in a global frame can be expressed as

$$\delta \mathbf{x} = \delta_R \mathbf{x} + \delta \omega \times \mathbf{x} = \delta_R \mathbf{x} + \mathbf{Spin}(\delta \omega) \mathbf{x} \quad (2.117)$$

where  $\delta_R \mathbf{x}$  is the variation of the vector in the co-rotated frame, and  $\delta \omega$  is the variation of the global rotation of the frame. The variation of the *co-rotated* deformational displacement vector  $\mathbf{u}_d$  in a co-rotated frame is obtained via the variation of the global deformational displacements with respect to global  $\mathbf{v}$ , and using Eq. 2.117 to find the variation of the co-rotated deformational *displacements* with respect to global  $\mathbf{v}$ . Eq. 2.108 states that deformational displacement of an element node  $a$  is

$$\mathbf{u}_{da} = \mathbf{u}_a - \mathbf{u}_c - (\mathbf{R}_{0n} - \mathbf{I}) \mathbf{x}_a^0 = \sum_{b=1}^N \delta_{ab} \mathbf{u}_b - \sum_{b=1}^N \frac{1}{N} \mathbf{u}_b - (\mathbf{R}_{0n} - \mathbf{I}) \mathbf{x}_a^0 \quad (2.118)$$

$\mathbf{u}_c$  is the displacement vector for the element centroid, and  $\delta_{ab}$  is the Kronecker delta, hence

$$\mathbf{u}_{da} = \sum_{b=1}^N \mathbf{P}_{ab} \mathbf{u}_b - (\mathbf{R}_{0n} - \mathbf{I}) \mathbf{x}_a^0 \quad (2.119)$$

$$\mathbf{P}_{ab} = \left( \delta_{ab} - \frac{1}{N} \right) \mathbf{I} \quad (2.120)$$

The variation of global  $\mathbf{u}_{da}$  with respect to global  $\mathbf{v}$  is found as

$$\delta \mathbf{u}_{da} = \sum_{b=1}^N \mathbf{P}_{ab} \delta \mathbf{u}_b - \delta \mathbf{R}_{0n} \mathbf{x}_a^0 \quad (2.121)$$

Using Eq. 2.116 we have

$$\delta \mathbf{R}_{0n} \mathbf{x}_a^0 = \mathbf{Spin}(\delta \boldsymbol{\omega}_r) \mathbf{R}_{0n} \mathbf{x}_a^0 = \mathbf{Spin}(\delta \boldsymbol{\omega}_r) \mathbf{x}_a^{0n} = -\mathbf{Spin}(\mathbf{x}_a^{0n}) \delta \boldsymbol{\omega}_r \quad (2.122)$$

$$= -\mathbf{Spin}(\mathbf{x}_a^{0n}) \mathbf{G} \delta \mathbf{v} \quad (2.123)$$

The matrix  $\mathbf{G}$  connects the variation of the rigid body rotation of the shell element to the variation of the node displacements:

$$\delta \boldsymbol{\omega}_r = \frac{\partial \boldsymbol{\omega}_r}{\partial v_i} \delta v_i = \mathbf{G} \delta \mathbf{v} = \sum_{b=1}^N \mathbf{G}_b \delta \mathbf{v}_b \quad (2.124)$$

The matrix  $\mathbf{G}$  is an element-type dependent matrix. The variation of *global*  $\mathbf{u}_d$  with respect to global  $\mathbf{v}$  then reads

$$\delta \mathbf{u}_{da} = \sum_{b=1}^N ([\mathbf{P}_{ab} \quad \mathbf{0}] + \mathbf{Spin}(\mathbf{x}_a^{0n}) \mathbf{G}_b) \delta \mathbf{v}_b \quad (2.125)$$

$\delta \mathbf{v}_b$  is the global degrees of freedom for node  $b$ . Using the relationship  $\mathbf{u}_{da} = \mathbf{x}_a^n - \mathbf{x}_a^{0n}$ , we find that the variation of the co-rotated deformational displacement vector with respect to global degrees of freedom is given by

$$\delta_R \mathbf{u}_{da} = \delta_R \mathbf{x}_a^n - \delta_R \mathbf{x}_a^{0n} = \delta_R \mathbf{x}_a^n \quad (2.126)$$

Since  $\mathbf{x}_a^n = \mathbf{R}_{0n} \mathbf{x}_a^0 + \mathbf{u}_{da}$ , the variation of global  $\mathbf{x}_a^n$  with respect to global degrees of freedom is given by

$$\delta \mathbf{x}_a^n = \delta \mathbf{R}_{0n} \mathbf{x}_a^0 + \mathbf{R}_{0n} \delta \mathbf{x}_a^0 + \delta \mathbf{u}_{da} = \sum_{b=1}^N \mathbf{P}_{ab} \delta \mathbf{u}_b \quad (2.127)$$

Substituting  $\mathbf{x}_a^n$  for  $\mathbf{x}$  in Eq. 2.117 and solving with respect to  $\delta_R \mathbf{x}_a^n$  yields

$$\delta_R \mathbf{x}_a^n = \sum_{b=1}^N \mathbf{P}_{ab} \delta \mathbf{u}_b - \mathbf{Spin}(\delta \boldsymbol{\omega}_r) \mathbf{x}_a^n = \sum_{b=1}^N \mathbf{P}_{ab} \delta \mathbf{u}_b + \mathbf{Spin}(\mathbf{x}_a^n) \delta \boldsymbol{\omega}_r \quad (2.128)$$

$$= \sum_{b=1}^N ([\mathbf{P}_{ab} \quad \mathbf{0}] + \mathbf{Spin}(\mathbf{x}_a^n) \mathbf{G}_b) \delta \mathbf{v}_b \quad (2.129)$$

Hence, we have the variation of co-rotated deformational displacement vector with respect to global degrees of freedom  $\delta_R \mathbf{u}_{da} = \delta_R \mathbf{x}_a^n$ .

By starting with the variation of the co-rotated deformational rotations with respect to global degrees of freedom, the variation of the co-rotated deformational (finite) rotations with respect to the co-rotated deformational (infinitesimal) rotations is obtained. The derivation is based on work from Nour-Omid and Rankin [29], Simo [39] and Szwabowicz [45]:

$$\delta_R \boldsymbol{\theta}_{da} = \frac{\partial \boldsymbol{\theta}_{da}}{\partial \boldsymbol{\omega}_{da}} \delta_R \boldsymbol{\omega}_{da} = \frac{\partial (\mathbf{Axial}(\ln(\mathbf{R}_{da})))}{\partial \boldsymbol{\omega}_{da}} \delta_R \boldsymbol{\omega}_{da} = \mathbf{H}_a \delta_R \boldsymbol{\omega}_{da} \quad (2.130)$$

$$\mathbf{H}_a = \frac{\partial \boldsymbol{\theta}_a}{\partial \boldsymbol{\omega}} = \mathbf{I} - \frac{1}{2} \mathbf{Spin}(\boldsymbol{\theta}_a) + \eta \mathbf{Spin}(\boldsymbol{\theta}_a)^2 \quad (2.131)$$

$$\eta = \frac{\sin(\frac{1}{2}\theta_a) - \frac{1}{2}\theta_a \cos(\frac{1}{2}\theta_a)}{\theta_a^2 \sin(\frac{1}{2}\theta_a)} \quad \text{and} \quad \theta_a = \sqrt{\boldsymbol{\theta}_a^T \boldsymbol{\theta}_a} = \|\theta_a\| \quad (2.132)$$

$$\delta_R \boldsymbol{\omega}_{da} = \delta \boldsymbol{\omega}_a - \delta \boldsymbol{\omega}_r = \delta \boldsymbol{\omega}_a - \frac{\partial \boldsymbol{\omega}_r}{\partial v_i} \delta v_i = \delta \boldsymbol{\omega}_a - \mathbf{G}_a \delta \mathbf{v}_a \quad (2.133)$$

$\mathbf{G}$  is defined in Eq. 2.124.  $\delta_R \boldsymbol{\omega}_{da}$  may now be written as

$$\delta_R \boldsymbol{\omega}_{da} = \sum_{b=1}^N (\delta_{ab} [\mathbf{0} \quad \mathbf{I}] - \mathbf{G}_b) \delta \mathbf{v}_b \quad (2.134)$$

Introducing Eq. 2.119 into Eq. 2.130 yields the final expression for the variation of co-rotated deformational rotation with respect to global degrees of freedom.

$$\delta_R \boldsymbol{\theta}_{da} = \mathbf{H}_a \sum_{b=1}^N (\delta_{ab} [\mathbf{0} \quad \mathbf{I}] - \mathbf{G}_b) \delta \mathbf{v}_b \quad (2.135)$$

For an element with  $N$  nodes, the nodal degrees of freedom are ordered as follows

$$\mathbf{v}^T = [\mathbf{u}_1^T \quad \boldsymbol{\theta}_1^T \quad \dots \quad \mathbf{u}_N^T \quad \boldsymbol{\theta}_N^T] \quad (2.136)$$

If Eqs. 2.128 and 2.135 are ordered accordingly,  $\delta_R \mathbf{v}_d$  (containing both displacements and rotations) may be written as

$$\delta_R \mathbf{v}_d = \mathbf{H} (\mathbf{I} - \mathbf{P}_T - \mathbf{P}_R) \delta \mathbf{v} = \mathbf{H} \mathbf{P} \delta \mathbf{v} \quad (2.137)$$

Matrix  $\mathbf{P}$  is a nonlinear projector operator that filters out rigid body translation and rotation.

The variation of the co-rotated deformational displacement vector has now been found with respect to a set of global degrees of freedom. To enable use of existing linear elements put in the rotating frame, the global system is chosen to be that of the co-rotated element. Thus, Eq. 2.137 is modified to

$$\delta_R \tilde{\mathbf{v}}_d = \tilde{\mathbf{H}} \tilde{\mathbf{P}} \delta \tilde{\mathbf{v}} \quad (2.138)$$

Taking advantage of the transformation between local and global coordinate system, we have

$$\delta_R \tilde{\mathbf{v}}_d = \tilde{\mathbf{H}} \tilde{\mathbf{P}} \mathbf{T}_n \delta \mathbf{v} \quad (2.139)$$

The consistent tangent stiffness is obtained by the variation of the internal force vector  $\mathbf{f}_e$  with respect to  $\mathbf{v}$ :

$$\delta \mathbf{f}_e = \frac{\partial \mathbf{f}}{\partial \mathbf{v}} \delta \mathbf{v} = \mathbf{K}_t \delta \mathbf{v} \quad (2.140)$$

Using Eq. 2.113 for  $\mathbf{f}_e$ , Eq. 2.140 yields:

$$\delta \mathbf{f} = \delta \mathbf{T}^T \tilde{\mathbf{P}}^T \tilde{\mathbf{H}}^T \tilde{\mathbf{f}}_e + \mathbf{T}^T \delta_R \tilde{\mathbf{P}}^T \tilde{\mathbf{H}}^T \tilde{\mathbf{f}}_e + \mathbf{T}^T \tilde{\mathbf{P}}^T \delta_R \tilde{\mathbf{H}}^T \tilde{\mathbf{f}}_e + \mathbf{T}^T \tilde{\mathbf{P}}^T \tilde{\mathbf{H}}^T \delta \tilde{\mathbf{f}}_e \quad (2.141)$$

$$= (\mathbf{K}_{GR} + \mathbf{K}_{GP} + \mathbf{K}_{GM} + \mathbf{K}_{MG}) \delta \mathbf{v} = \mathbf{K}_T \delta \mathbf{v} \quad (2.142)$$

The different terms of the tangent stiffness represent rotational geometric stiffness, projection geometric stiffness, moment correction geometric stiffness, and material stiffness, respectively.

The rotational geometric stiffness arises from the variation of the transformation matrix between initial configuration  $C_0$  and shadow configuration  $C_n$ . As a rigid rotation of a stressed element rotates the stresses, the internal forces change direction to preserve equilibrium.

The equilibrium projection geometric stiffness arises from the variation of the projector matrix  $\tilde{\mathbf{P}}^T$ , and reflects the variation of the force vector due to variations in the degrees of freedom.

The moment correction geometric stiffness arises from variation of the rotation pseudo-vector Jacobian  $\tilde{\mathbf{H}}$ .

## 2.2.3 Plasticity modelling for shell element

### 2.2.3.1 Stress resultant plasticity

The shell element used together with the line-spring element in this study is a high-performance and non-conforming thin shell finite element based on assumed natural deviatoric strains, denoted ANDES. The ANDES element was initially developed by Felippa and Militello [12]. It was further extended by Skallerud and Haugen [43] to handle large rotations and inelastic behaviour. The ANDES shell finite element is derived in a co-rotated formulation which gives a stringent way of extracting only the strains and curvatures producing deformations in the element. The strains at element level is assumed to be small, but the global deformations can still be large. The derivations for the co-rotated ANDES finite element are rather lengthy and a detailed description is published by Skallerud et al. [44].

The material model is based on stress resultant plasticity. A stress resultant yield criterion derived by Ilyushin is employed and expressed as

$$\begin{aligned} f(\bar{\mathbf{n}}, \bar{\mathbf{m}}) &= \sqrt{\frac{\bar{N}}{t^2} + \frac{4s\bar{P}}{\sqrt{3}t^3} + \frac{16\bar{M}}{t^4}} - \sigma_0 = 0 \\ \bar{N} &= N_x^2 + N_y^2 - N_x N_y + 3N_{xy}^2 \\ \bar{M} &= M_x^2 + M_y^2 - M_x M_y + 3M_{xy}^2 \\ \bar{P} &= N_x M_x + N_y M_y - \frac{1}{2}N_x M_y - \frac{1}{2}N_y M_x + 3N_{xy} M_{xy} \\ s &= \frac{\bar{P}}{\|\bar{P}\|} = \pm 1 \end{aligned} \quad (2.143)$$

Writing the stress resultant vector in an integration point as  $\boldsymbol{\sigma} = [\bar{\mathbf{n}}, \bar{\mathbf{m}}]^T$ , the yield criterion from Eq. 2.143 can be expressed in quadratic form (see Matthies [26] and Ibrahimbegovic and Frey [19]) as

$$f = \boldsymbol{\sigma}^T \mathbf{A} \boldsymbol{\sigma} - \left(1 + \frac{H\varepsilon_{pl}}{\sigma_0}\right)^2 = 0 \quad (2.144)$$

$$\begin{aligned} \mathbf{A} &= \begin{bmatrix} \frac{1}{n_0^2} \bar{\mathbf{A}} & \frac{s}{2\sqrt{3}m_0 n_0} \bar{\mathbf{A}} \\ \frac{s}{2\sqrt{3}m_0 n_0} \bar{\mathbf{A}} & \frac{1}{m_0^2} \bar{\mathbf{A}} \end{bmatrix} & \bar{\mathbf{A}} &= \frac{1}{2} \begin{bmatrix} 2 & -1 & 0 \\ -1 & 2 & 0 \\ 0 & 0 & 6 \end{bmatrix} \\ m_0 &= \frac{1}{4}\sigma_0 t^2, \quad n_0 = \sigma_0 t \end{aligned} \quad (2.145)$$

Skallerud and Haugen [43] simplified the original Ilyushin yield criterion from Eq. 2.143 by setting the parameter  $s$  to zero. The yield surface is now constructed as a circle in the  $MN$  space. The Ilyushin and the simplified yield surface are plotted in Fig. 2.23. It is seen that the maximum difference is about 12% and is located where membrane force and bending moment are balanced.  $s = 0$  removes the numbers on the off-diagonal of the  $\bar{\mathbf{A}}$  matrix which also removes the corners on the Ilyushin yield surface. The simplification where  $s = 0$  is used herein. Using this stress resultant yield criterion one does not need to perform a through the thickness integration, hence the stress resultant update for the element is very fast.

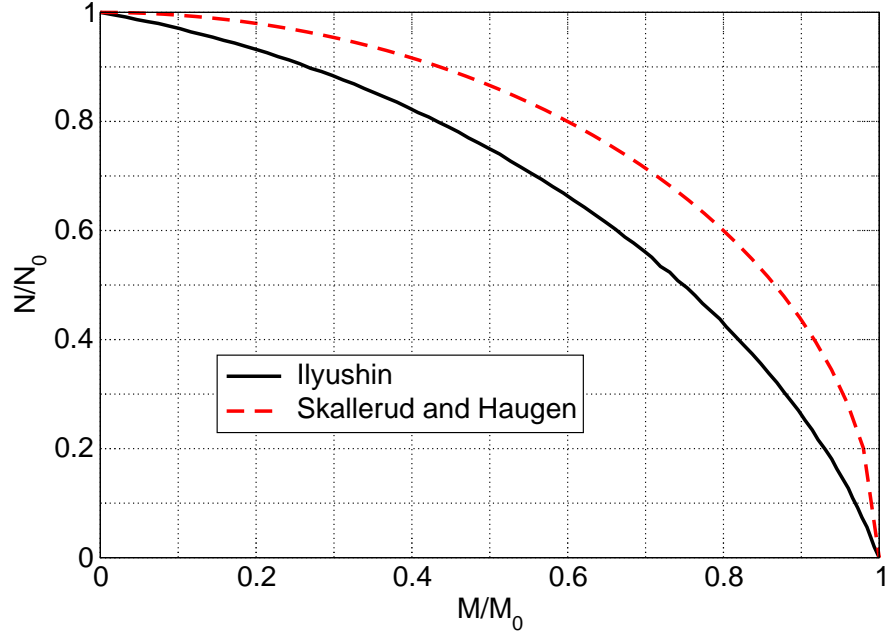


Figure 2.23: Ilyushin and simplified yield surface in the  $MN$  space [43]

Implicit backward Euler stress update scheme is being used for the stress resultant stress update in the ANDES finite element. An associated flow rule reads

$$\Delta \varepsilon_{pl,n+1} = \Delta \lambda_{n+1} \frac{\partial f}{\partial \sigma_{n+1}} = 2 \Delta \lambda_{n+1} \mathbf{A} \sigma \quad (2.146)$$

where  $\Delta \varepsilon$  are the incremental membrane and curvature strains as shown in Eq. 2.147

$$\Delta \varepsilon = \begin{bmatrix} \Delta \varepsilon_m \\ \Delta \kappa \end{bmatrix} \quad (2.147)$$

The stress resultant vectors (strains and stresses) and the equivalent scalar quantities are related through a work hardening model as shown in Eq. 2.148.

$$\sigma^T d\varepsilon = \bar{\sigma} d\varepsilon_{pl} \quad (2.148)$$

where  $\bar{\sigma} = \sqrt{\sigma^T \mathbf{A} \sigma}$ . Using the yield criterion on the form in Eq. 2.144, the flow rule from Eq. 2.146 and the work hardening model from Eq. 2.148, the equivalent plastic strain increment can be expressed as

$$d\varepsilon_{pl} = 2d\lambda \bar{\sigma} \quad (2.149)$$

A power law hardening model for the material is used:

$$\bar{\sigma} = \sigma_0 \left( \frac{\bar{\varepsilon}}{\varepsilon_0} + 1 \right)^n \quad (2.150)$$



where  $\sigma_0 = E\varepsilon_0$  and  $n$  is the hardening exponent ( $0 \leq n \leq 1$ ). The expression for the updated stress following the elastic predictor and plastic corrector approach reads

$$\boldsymbol{\sigma}_{n+1} = \boldsymbol{\sigma}_{trial} - \mathbf{C}\Delta\boldsymbol{\varepsilon}_{pl,n+1} \quad (2.151)$$

Reorganising Eq. 2.151 and substituting  $\Delta\boldsymbol{\varepsilon}_{pl,n+1}$  with the result from the flow rule in Eq. 2.146, the expression for the updated stress level is

$$\boldsymbol{\sigma}_{n+1} = [\mathbf{I} + 2\Delta\lambda_{n+1}\mathbf{CA}]\boldsymbol{\sigma}_{trial} \quad (2.152)$$

Now the yield criterion from Eq. 2.144 only depends on  $\Delta\lambda$ . Using a Newton-Raphson iteration scheme, the non-linear function  $f(\Delta\lambda_{n+1})$  can be solved to update the stresses. The consistent material tangent stiffness matrix in the integration point now reads

$$d\boldsymbol{\sigma} = \left[ \mathbf{D} - \frac{\mathbf{D}\mathbf{g}\mathbf{g}^T\mathbf{D}}{\mathbf{g}^T\mathbf{D}\mathbf{g} + \gamma} \right] d\boldsymbol{\varepsilon} = \mathbf{C}_{ct}d\boldsymbol{\varepsilon} \quad (2.153)$$

$$\gamma = \frac{2\alpha\bar{\sigma}}{1 - \alpha\frac{\Delta\lambda}{\bar{\sigma}}} \quad , \quad \alpha = \frac{2H}{\sigma_0^2}(\sigma_0 + H\varepsilon_{pl,n+1}) \quad , \quad \mathbf{g} = 2\mathbf{A}\boldsymbol{\sigma}$$

$$\mathbf{D}^{-1} = \mathbf{C}^{-1} + 2\Delta\lambda\mathbf{A} \quad (2.154)$$

The consistent tangent stiffness matrix in Eq. 2.154 is transmitted back to the main program to solve the equation system.

### 2.2.3.2 Through the thickness integration

Through the thickness integration is performed numerically in  $\text{LINK}_{pipe}$  using the Lobatto quadrature [27] with a user defined number of integration points through the thickness. It is also possible to specify two layers with different material properties through the thickness, i.e. a laminate.

A plane stress behaviour is assumed in the through the thickness integration points. A fully implicit backward Euler stress update scheme is applied here. The updated stresses are used to compute the stress resultants transmitted back to the main program.

As  $\text{LINK}_{pipe}$  is based on stress resultants, the stress distribution through the thickness of the shell element must be integrated to form the stress resultants. The consistent tangent stiffness matrices from through the thickness must also be integrated according to the same scheme.

The Kirchhoff assumption for strain distribution through the thickness is used:

$$\varepsilon_{\alpha\beta} = \varepsilon_0 + z\kappa_0 \quad (2.155)$$

where  $\varepsilon_0$  and  $\kappa_0$  are strain components in the reference plane, i.e. the plane of the nodal points (see Fig. 2.24).  $z$  is the position of an integration point relative to the reference plane. It is assumed a linear strain distribution through the thickness. The positions of the through the thickness integration points follow the Lobatto quadrature (see Michels [27]). Abscissas and the corresponding weight coefficients are tabulated in the code for a range of integration point numbers. The Lobatto quadrature is similar to Simpson's rule as they both have an integration point at the position for the most outer fibre. Fig. 2.25 shows the principles by laminating the shell thickness (see also [13]).

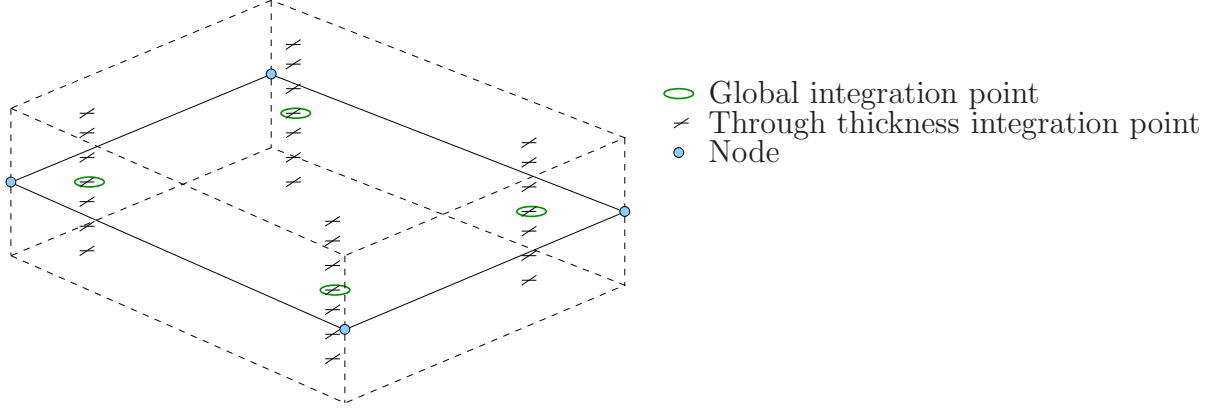


Figure 2.24: Location of the integration points through the thickness for the element

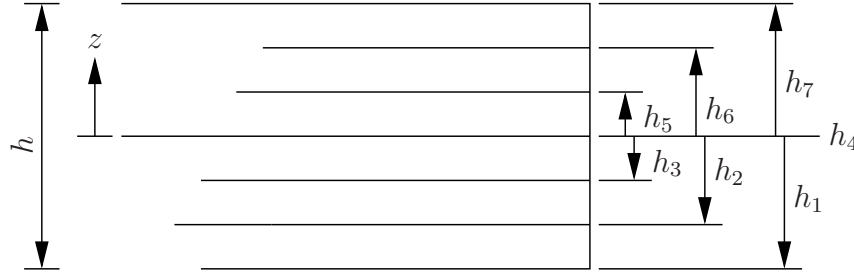


Figure 2.25: Layer nomenclature for laminate

The numerical integral from Lobatto quadrature can be approximated as

$$\int_{-t/2}^{t/2} f(z) dz = w_1 f\left(-\frac{t}{2}\right) + w_n f\left(\frac{t}{2}\right) + \sum_{i=2}^{n-1} w_i f(z_i) \quad (2.156)$$

where  $z_i$  are the positions of the integration points in Lobatto quadrature (abscissas) and  $w_i$  are the weight for the corresponding abscissa.  $f(z_i)$  are the stress values for the given positions.

The following two expressions relate the stress distribution through the thickness to the stress resultants which will be transmitted back to the main program:

$$\mathbf{N} = \int_{-t/2}^{t/2} \boldsymbol{\sigma} dh = \frac{t}{2} \int_{-1}^1 \boldsymbol{\sigma} dz \approx \frac{t}{2} \sum_{i=1}^n w_i \boldsymbol{\sigma}_i \quad (2.157)$$

$$\mathbf{M} = \int_{-t/2}^{t/2} \boldsymbol{\sigma} h dh = \frac{t}{2} \int_{-1}^1 \boldsymbol{\sigma} z dz \approx \left(\frac{t}{2}\right)^2 \sum_{i=1}^n w_i z_i \boldsymbol{\sigma}_i \quad (2.158)$$

where  $n$  is the number of through thickness integration points and  $t$  is the shell thickness.  $h$  is the distance from the mid-plane to an integration point and  $z$  is the normalised distance used in Lobatto quadrature.  $\mathbf{N}$  and  $\mathbf{M}$  are the stress resultant arrays for membrane forces and bending moments.

Construction of the stiffness matrix for the laminate is performed similarly to the stress resultants. The equation system for an integration point in the “stress resultant space” is

expressed as

$$\begin{Bmatrix} d\mathbf{N} \\ d\mathbf{M} \end{Bmatrix} = \begin{bmatrix} \mathbf{K}_{NN} & \mathbf{K}_{MN} \\ \mathbf{K}_{MN} & \mathbf{K}_{MM} \end{bmatrix} \begin{Bmatrix} d\boldsymbol{\varepsilon}^0 \\ d\boldsymbol{\kappa}^0 \end{Bmatrix} \quad (2.159)$$

Now inserting the stress matrices from the through thickness integration points as

$$d\boldsymbol{\sigma} = \mathbf{D}d\boldsymbol{\varepsilon} \quad (2.160)$$

where  $\mathbf{D}$  is the consistent tangent stiffness matrix from the through thickness integration points. The strain matrix is decomposed in a in-plane strain increment and a curvature strain increment (as shown in Eq. 2.155). The incremental stress resultants is expressed as

$$\begin{aligned} d\mathbf{N} &= \frac{t}{2} \int_{-1}^1 \mathbf{D}d\boldsymbol{\varepsilon}^0 dz + \left(\frac{t}{2}\right)^2 \int_{-1}^1 w_k \mathbf{D}z_k d\boldsymbol{\kappa}^0 dz \\ &\approx \frac{t}{2} \sum_{k=1}^n w_k \mathbf{D}^k d\boldsymbol{\varepsilon}^0 + \left(\frac{t}{2}\right)^2 \sum_{k=1}^n w_k z_k \mathbf{D}^k d\boldsymbol{\kappa}^0 \end{aligned} \quad (2.161)$$

$$\begin{aligned} d\mathbf{M} &= \left(\frac{t}{2}\right)^2 \int_{-1}^1 w_k \mathbf{D}z_k d\boldsymbol{\kappa}^0 dz + \left(\frac{t}{2}\right)^3 \int_{-1}^1 \mathbf{D}d\boldsymbol{\kappa}^0 z^2 dz \\ &\approx \left(\frac{t}{2}\right)^2 \sum_{k=1}^n w_k z_k \mathbf{D}^k d\boldsymbol{\varepsilon}^0 + \left(\frac{t}{2}\right)^3 \sum_{k=1}^n w_k z_k^2 \mathbf{D}^k d\boldsymbol{\kappa}^0 \end{aligned} \quad (2.162)$$

Now the stiffness matrix can be written as

$$\begin{bmatrix} dN_x \\ dN_y \\ dN_{xy} \\ dM_x \\ dM_y \\ dM_{xy} \end{bmatrix} = \underbrace{\begin{bmatrix} A_{11} & A_{12} & A_{13} & B_{11} & B_{12} & B_{13} \\ A_{21} & A_{22} & A_{23} & B_{21} & B_{22} & B_{23} \\ A_{31} & A_{32} & A_{33} & B_{31} & B_{32} & B_{33} \\ B_{11} & B_{12} & B_{13} & D_{11} & D_{12} & D_{13} \\ B_{21} & B_{22} & B_{23} & D_{21} & D_{22} & D_{23} \\ B_{31} & B_{32} & B_{33} & D_{31} & D_{32} & D_{33} \end{bmatrix}}_{\mathbf{K}} \begin{bmatrix} d\varepsilon_x \\ d\varepsilon_y \\ d\gamma_{xy} \\ d\kappa_x \\ d\kappa_y \\ d\kappa_{xy} \end{bmatrix} \quad (2.163)$$

where

$$A_{ij} = \left(\frac{t}{2}\right) \sum_{k=1}^n w_k C_{ij}^k \quad (2.164)$$

$$B_{ij} = \left(\frac{t}{2}\right)^2 \sum_{k=1}^n w_k z_k C_{ij}^k \quad (2.165)$$

$$D_{ij} = \left(\frac{t}{2}\right)^3 \sum_{k=1}^n w_k z_k^2 C_{ij}^k \quad (2.166)$$

where  $C_{ij}^k$  are the stiffness matrices from the through thickness integration points.

### 2.2.3.3 Stress update and isotropic strain hardening

Elastic predictor followed by a plastic corrector method according to fully implicit backward Euler is used in order to find the stress components at the end of the increment as shown in Eq. 2.167

$$\boldsymbol{\sigma}_{n+1} = \boldsymbol{\sigma}_{n+1}^{tr} - \Delta\lambda \mathbf{C}\mathbf{n}_{n+1} \quad (2.167)$$

A Newton-Raphson iteration process is used to solve the non-linear equation in Eq. 2.167. The yield function follows an isotropic plane stress von Mises formulation as

$$\begin{aligned} f &= \sigma_e - \sigma(\varepsilon_{pl}) \\ &= \sqrt{\sigma_x^2 + \sigma_y^2 - \sigma_x \sigma_y + 3\tau_{xy}^2} - \sigma(\varepsilon_{pl}) = 0 \end{aligned} \quad (2.168)$$

where  $\sigma_e$  also can be expressed in matrix form as

$$\sigma_e = \sqrt{\boldsymbol{\sigma}^T \mathbf{P} \boldsymbol{\sigma}} \quad (2.169)$$

where  $\mathbf{P}$  for isotropic von Mises material is

$$\mathbf{P} = \begin{bmatrix} 1 & -\frac{1}{2} & 0 \\ -\frac{1}{2} & 1 & 0 \\ 0 & 0 & 3 \end{bmatrix} \quad (2.170)$$

The consistent tangent stiffness matrix for an integration point is described as

$$\mathbf{C}_{cct} = \mathbf{R} - \frac{(\mathbf{n}^T \mathbf{R})^T (\mathbf{n}^T \mathbf{R})}{\mathbf{n}^T \mathbf{R} \mathbf{n} + \hat{H}} \quad (2.171)$$

$$\mathbf{R} = \left[ \mathbf{C}_{el} + \Delta \lambda \frac{\partial \mathbf{n}}{\partial \boldsymbol{\sigma}} \right]^{-1} \quad (2.172)$$

#### 2.2.3.4 Non linear kinematic hardening

In the present implementation, the material model is based on through thickness integration following the Lobatto quadrature. The Ziegler translation rule is used for a single yield surface. The memory is accounted for by keeping track of the maximum stress level experienced on the stress-strain curve. An approximation to the Masing's rule (see Masing [25]) is preserved by storing the stress level from both tension and compression for each reversed loading. This makes the present model quite similar to a two surface model where the boundary surface acts as a memory surface.

A fully implicit backward Euler stress update algorithm with the Ziegler kinematic hardening rule is implemented. The uni-axial monotonic stress-strain curve is used as input for the stress update. The curve is transmitted as points (plastic strain versus true stress). The present implementation makes use of the Ziegler hardening rule for a non-linear stress-strain curve. Since the non-linear curve is presented as a point-wise curve, linear segments are used between the points, hence a modified Ziegler kinematic hardening rule with the Masing's rule can be used.

A plane stress situation is assumed in each layer through the thickness, thus the stress space is reduced from 3D to 2D where all stress components  $\sigma_{i3}$  and  $\sigma_{3j}$  from the stress tensor vanish. The yield function is shown in Eq. 2.173.

$$f = \underbrace{\sqrt{\tilde{\sigma}_x^2 + \tilde{\sigma}_y^2 - \tilde{\sigma}_x \tilde{\sigma}_y + 3\tilde{\tau}_{xy}^2}}_{\sigma_e} - \sigma_0 = 0 \quad (2.173)$$

where  $\tilde{\sigma}$  is the normalised stress component expressed as  $\tilde{\sigma} = \sigma - \alpha$ .  $\alpha$  is the kinematic back-stress vector and  $\sigma_e$  is the effective von Mises stress.

The consistent tangent stiffness matrix is expressed in matrix notation as

$$\mathbf{C}_{ct} = \left[ \mathbf{R} - \frac{(\mathbf{n}^T \mathbf{R})^T (\mathbf{n}^T \mathbf{R})}{\mathbf{n}^T \mathbf{R} \mathbf{n} + \hat{H}} \right] \quad (2.174)$$

$$\mathbf{R} = \left[ \mathbf{C}^{-1} + \Delta\lambda \frac{\partial \mathbf{n}}{\partial \boldsymbol{\sigma}} \right]^{-1} \quad (2.175)$$

where  $\mathbf{n}$  is the normal vector to the yield surface (first derivative of the yield function).  $\hat{H}$  is the current slope of the stress-strain curve,  $\mathbf{C}$  is the elastic stiffness matrix and  $\Delta\lambda$  is the plastic multiplier. The derivations of the consistent tangent stiffness matrix for a plane stress situation with a von Mises material follows the same update scheme for both isotropic and kinematic hardening, and can be found in the literature, e.g. Crisfield [10] and Simo and Hughes [40].

More details about this implementation is presented by Berg et al. [3].

### 2.2.3.5 Different material properties through the thickness

An extension of the through the thickness integration from Sec. 2.2.3.2 is to account for different material properties through the thickness. Each ply is generally assigned different thickness and material properties. The shell thickness is the sum of the ply thicknesses. Fig. 2.26 shows a schematic view of the ply construction for two plies.

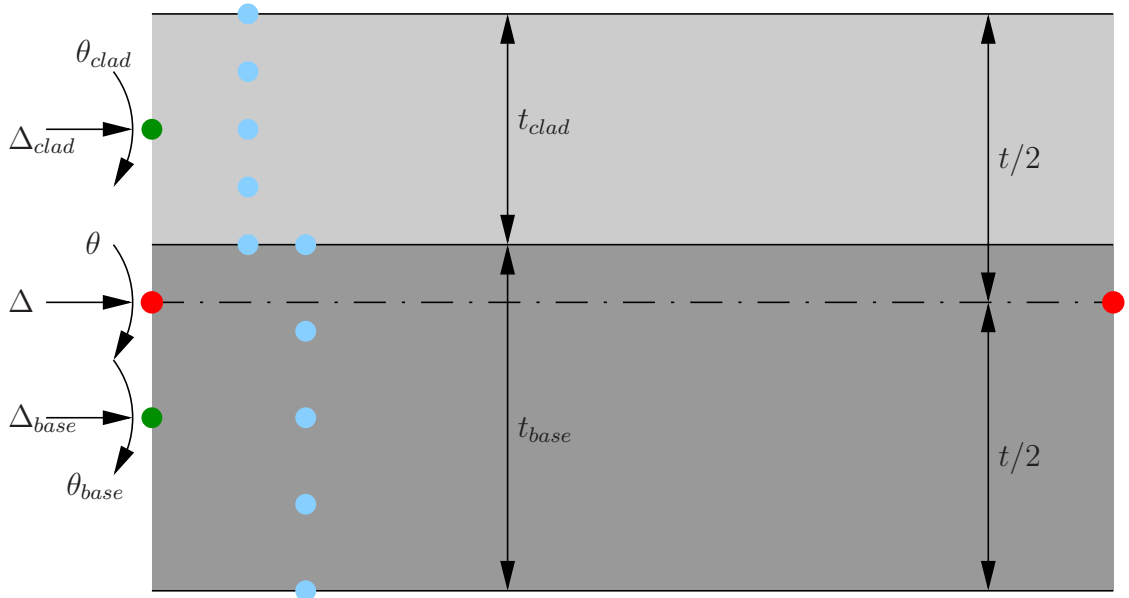


Figure 2.26: Nodal displacements/rotations from the element nodes to the through the thickness integration points. Red dots are the element integration points at mid-thickness, red dots are the centres of the different plies and the blue dots are the through the thickness integration points in the plies

The integration points through the thickness are numbered according to the system in Fig. 2.27. The position of the centre of an arbitrary ply will define the offset from the centre of the total thickness for any integration point in this ply. Integration points below the centre of the total thickness will have a negative moment arm and vice versa.

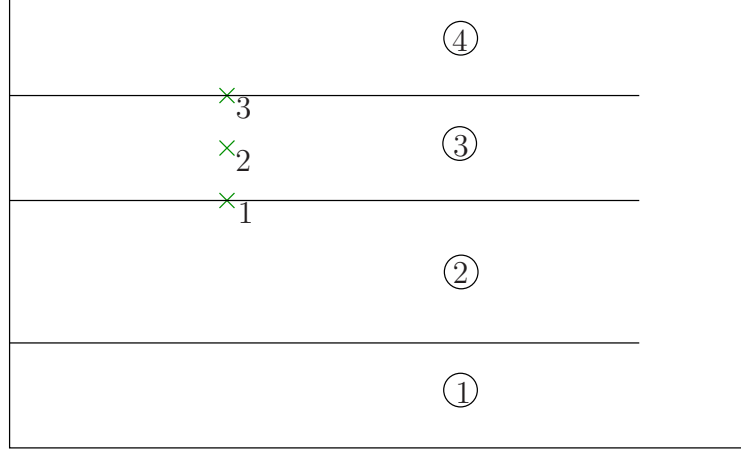


Figure 2.27: Numbering of the plies and the through the thickness integration points

The position for the centre ( $z_i^0$ ) of ply  $i$  in a laminate of  $n$  plies can be expressed as

$$z_i^0 = \frac{1}{2} \left[ t_i - \sum_{k=0}^n t_k \right] + \sum_{k=0}^{i-1} t_k \quad (2.176)$$

where the thickness of the laminate  $k = 0$  is defined as 0. Then the position of any integration point,  $j$ , in any ply,  $i$ , is defined as

$$z_j = z_i^0 + \frac{1}{2} \bar{z}_j t_i = \frac{1}{2} \left[ t_i - \sum_{k=0}^n t_k \right] + \sum_{k=0}^{n-(i-1)} t_k + \frac{1}{2} \bar{z}_j t_i \quad (2.177)$$

where  $\bar{z}_j$  is the abscissa in the Lobatto quadrature of an integration point relative to the centre of the thickness in a ply.

When the position of the integration points are known ( $z_j$ ), the strain components for the mid-thickness integration points ( $\varepsilon^0$  and  $\kappa^0$ ) can be lumped to the through the thickness integration points using the following linear expressions:

$$\varepsilon_x = \varepsilon_x^0 + \kappa_y^0 z_j \quad (2.178)$$

$$\varepsilon_y = \varepsilon_y^0 + \kappa_y^0 z_j \quad (2.179)$$

$$\gamma_{xy} = \gamma_{xy}^0 + \kappa_{xy}^0 z_j \quad (2.180)$$

This is consistent with Kirchhoff's assumption mentioned in Sec. 2.2.3.2.

### Stress resultants from the plies

For each ply, a set of stress resultants are produced based on the stress components from each integration point through the thickness of the current ply. When stress resultants are formed for all the plies, these are used to compute the equivalent stress resultants for the complete shell thickness.

The equivalent stress resultants for the total thickness can be expressed as a sum of the stress resultants from the plies. Note that each membrane stress resultant contributes to the bending stress resultants.

$$\mathbf{N}_{tot} = \sum_{k=1}^n \mathbf{N}_k \quad (2.181)$$

$$\mathbf{M}_{tot} = \sum_{k=1}^n \mathbf{M}_k + \sum_{k=1}^n \mathbf{N}_k z_k \quad (2.182)$$

where  $\mathbf{N}_k$  is the membrane stress resultant for ply number  $k$  and  $\mathbf{M}_k$  is the bending stress resultant for ply number  $k$ .  $z_k$  is the sign and distance from the centre of the shell thickness to the centre of ply number  $k$ .

The stiffness matrices for the plies are formed individually with respect to the stiffness matrices from each through the thickness integration point.  $n$   $6 \times 6$  matrices will then be formed.

A general expression for a stiffness relation for eccentric laminates is

$$\mathbf{K} = \begin{bmatrix} \mathbf{K}_{11} & \mathbf{K}_{12} + c\mathbf{K}_{11} \\ \mathbf{K}_{21} + c\mathbf{K}_{11} & \mathbf{K}_{22} + c^2\mathbf{K}_{11} \end{bmatrix} \quad (2.183)$$

where  $c$  is a symbolic expression for eccentricity.  $\mathbf{K}$  from Eq. 2.183 is a symmetric matrix. Using the  $n$  stiffness matrices from the through the thickness integration points, these can be summed term by term to build the equivalent stiffness matrix for the shell thickness as shown in Eqs. 2.184-2.186. The general form from Eq. 2.183 is here shown in detail.

$$\mathbf{K}_{11} = \sum_{p=1}^n \mathbf{K}_{11}^p \quad (2.184)$$

$$\mathbf{K}_{12} = \mathbf{K}_{21} = \sum_{p=1}^n \mathbf{K}_{12}^p + \sum_{p=1}^n z_p^0 \mathbf{K}_{11}^p \quad (2.185)$$

$$\mathbf{K}_{22} = \sum_{p=1}^n \mathbf{K}_{22}^p + \sum_{p=1}^n (z_p^0)^2 \mathbf{K}_{11}^p \quad (2.186)$$

$$(2.187)$$

where the index  $p$  is the current ply number and  $n$  is the total number of plies.  $z_p^0$  is the real position (in the range  $-t/2$  to  $t/2$ ) of the of the centre of the current ply. The terms  $K_{ij}^p$  are expressed as

$$\mathbf{K}_{11}^p = \left(\frac{t_p}{2}\right) \sum_{k=1}^m w_k C_{ij}^k \quad (2.188)$$

$$\mathbf{K}_{12}^p = \left(\frac{t_p}{2}\right)^2 \sum_{k=1}^n w_k z_k C_{ij}^k \quad (2.189)$$

$$\mathbf{K}_{22}^p = \left(\frac{t_p}{2}\right)^3 \sum_{k=1}^n w_k z_k^2 C_{ij}^k \quad (2.190)$$

The stiffness matrix construction from Eqs. 2.184-2.190 is transmitted back to the main program.

**Known limitations**

The sum of the ply thicknesses gives the shell thickness. The shell thickness for the construction should obey thin shell conditions. The current implementation is restricted to two plies through the thickness.

It is also assumed the plies to be in full contact with no relative sliding.



## 2.3 Beam finite element

The beam element in  $\text{LINK}_{pipe}$  is used to transmit forces at the ends of a pipe (see Fig. 2.28). The beam element has a tubular cross section with elastic material properties. The global coordinate system for the pipe model is also shown in Fig. 2.28. All global deformations to the pipe model is applied to the hub node in the “end wheels” (see wheel illustration in Fig. 2.28). The beam elements are the spokes in the wheel

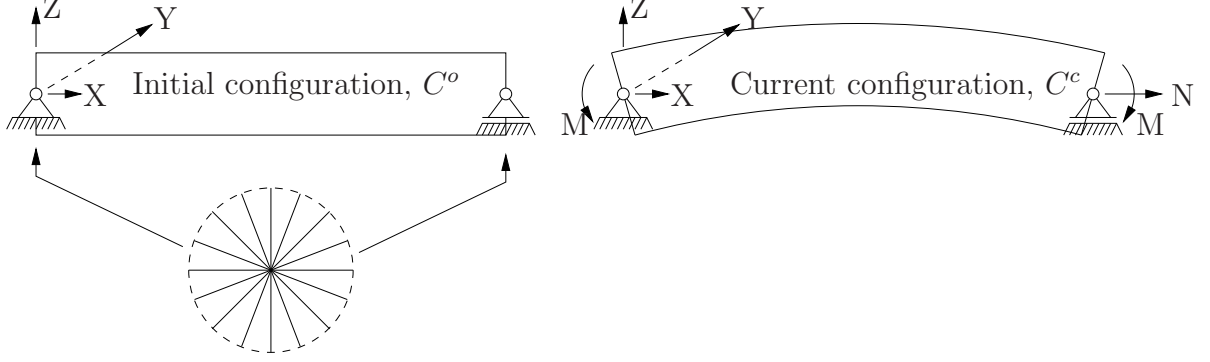


Figure 2.28: Global coordinate system and the beam elements at the pipe ends.

The 3D incremental beam stiffness relation between the current configuration ( $C^c$ ) and the next equilibrium configuration ( $C^{II}$ ) is expressed in the global coordinate system as

$$\mathbf{k}^c \Delta \mathbf{v} = \mathbf{S}_{ex}^{II} - \mathbf{S}_{in}^c \quad (2.191)$$

where

- $\mathbf{k}^c$  — linear elastic stiffness matrix of the beam ( $12 \times 12$ )
- $\Delta \mathbf{v}$  — incremental beam displacement vector
- $\mathbf{S}_{ex}^{II}$  — external beam nodal force vector
- $\mathbf{S}_{in}^c$  — internal beam nodal force vector

The bending stiffness and the torsion stiffness of the beam elements are relatively large in order to obtain a plane cross-section of the pipe at the two ends. Hence, the local displacements and rotations of a beam element are small.

Fig. 2.29 shows a typical geometry at the initial and the current configuration of a beam element.

Fig. 2.30 shows the unit vector directions at a beam node.

The current nodal global accumulated rotation vector  $\boldsymbol{\psi}^c$  may be written as

$$\boldsymbol{\psi}^c = \psi^c \mathbf{n} \quad (2.192)$$

and the rotated tangent direction is expressed as

$$\tilde{\mathbf{e}}_x^c = \mathbf{R}^c \mathbf{e}_x^o \quad (2.193)$$

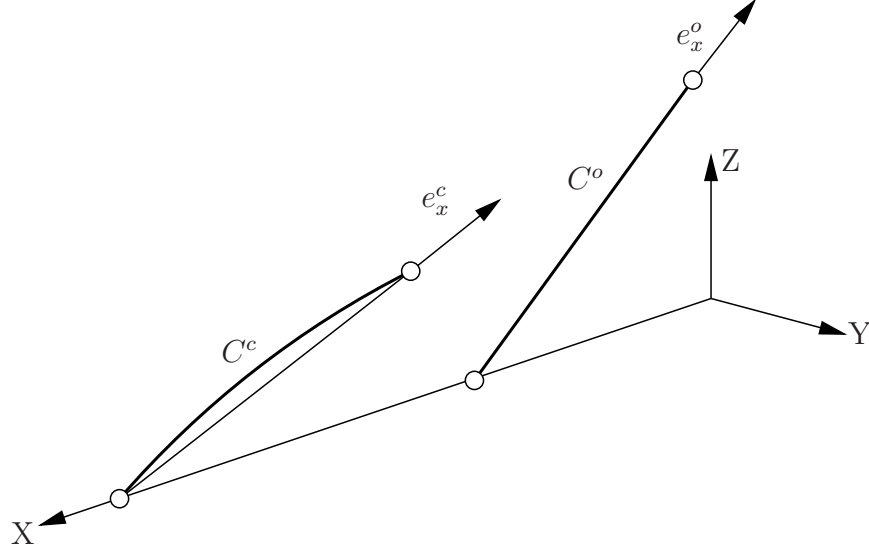
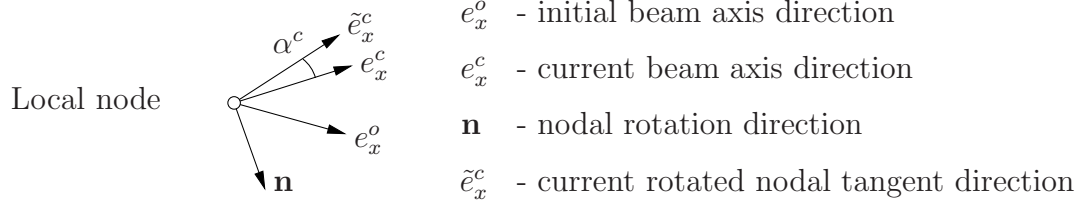
Figure 2.29: Initial configuration,  $C^o$  and current configuration,  $C^c$ 

Figure 2.30: Unit vector directions at a beam node

where the rotation matrix,  $\mathbf{R}^c$ , at configuration  $C^c$  is given by

$$\mathbf{R}^c = \begin{bmatrix} n_1^2(1-c) + c & n_1n_2(1-c) - n_3s & n_1n_3(1-c) + n_2s \\ n_2n_1(1-c) + n_3s & n_2^2(1-c) + c & n_2n_3(1-c) - n_1s \\ n_3n_1(1-c) - n_2s & n_3n_2(1-c) + n_1s & n_3^2(1-c) + c \end{bmatrix} \quad (2.194)$$

The following abbreviations were used in Eq. 2.194:

$$\begin{aligned} \mathbf{n} &= [n_1 \ n_2 \ n_3]^T \\ c &= \cos(\psi^c) \\ s &= \sin(\psi^c) \end{aligned}$$

The angle  $\alpha^c$  (in radians) from the current beam unit direction  $\mathbf{e}_x^c$  to the current rotated nodal tangent direction  $\tilde{\mathbf{e}}_x^c$  represents the bending rotation relatively to the current beam axis direction. The angle  $\alpha^c$  is found from

$$\mathbf{e}_x^c \times \tilde{\mathbf{e}}_x^c = \sin \alpha^c \mathbf{e}_{bend}^c \quad (2.195)$$

The global bending rotation vector,  $\alpha_{bend}^c$  is then

$$\alpha_{bend}^c = \alpha^c \mathbf{e}_{bend}^c = [\alpha_{1,bend}^c \ \alpha_{2,bend}^c \ \alpha_{3,bend}^c] \quad (2.196)$$

The change in the torsion rotation between node 1 and 2 for the beam is approximately given by

$$\alpha_{torsion}^c = (\psi_{node1}^c - \psi_{node2}^c) \cdot \mathbf{e}_x^o \quad (2.197)$$

since the directions of  $\tilde{\mathbf{e}}_x^c$  and  $\mathbf{e}_x^c$  are close to each other and the angle between  $\mathbf{e}_x^o$  and the rotated  $\mathbf{e}_x^o$  is constant. The global torsion rotation vector is then

$$\boldsymbol{\alpha}_{torsion}^c = \alpha_{torsion}^c \mathbf{e}_x^c = [\alpha_{1,torsion}^c \quad \alpha_{2,torsion}^c \quad \alpha_{3,torsion}^c] \quad (2.198)$$

The change in the beam length is given by  $\Delta L = L^c - L^o$  which in the global system corresponds to the following displacements in node 2:

$$\mathbf{u}_{node2}^c = \Delta L \mathbf{e}_x^c = [u_1^c \quad u_2^c \quad u_3^c] \quad (2.199)$$

Finally, the nodal forces in the global system is given by

$$\mathbf{S}_{in}^c = \mathbf{k}^c \begin{bmatrix} \mathbf{v}_{node1}^c \\ \mathbf{v}_{node2}^c \end{bmatrix} \quad (2.200)$$

where the vector of global local displacements and rotations equals

$$\mathbf{v}_{node1}^c = \begin{bmatrix} 0 \\ 0 \\ 0 \\ \alpha_{1,bend}^c \\ \alpha_{2,bend}^c \\ \alpha_{3,bend}^c \end{bmatrix} \quad \mathbf{v}_{node2}^c = \begin{bmatrix} u_1^c \\ u_2^c \\ u_3^c \\ \alpha_{1,bend}^c + \alpha_{1,torsion}^c \\ \alpha_{2,bend}^c + \alpha_{2,torsion}^c \\ \alpha_{3,bend}^c + \alpha_{3,torsion}^c \end{bmatrix} \quad (2.201)$$

The beam element has no axial stiffness. The bending stiffness,  $EI$ , is expressed using the inertia moment of a circular ring as

$$EI = E \frac{\pi (r_o^4 - r_i^4)}{4} \quad (2.202)$$

where  $r_o$  is the outer radius and  $r_i$  is the inner radius of the cross section. The material properties follow the material properties for the shell elements.

# Chapter 3

## Solution algorithm

### 3.1 Introduction

In order to treat limit points on the global response curve for the simulation (e.g. global and/or local instabilities) the usual Newton-Raphson iterations have to be modified or else divergent solutions are obtained. This can be done in a general way by means of Riks arc length method or the improved version by Fried, see Fried (1982). In effect, during the iterations both the external load level and the incremental solution vector (displacements and rotations) are adjusted. With this the external load level given by the load parameter may be reduced when limit points are passed. In the present implementation it is simplified to using a control degree of freedom that is restricted in size.

### 3.2 A load increment

The equation system to be solved at a current configuration can be expressed by

$$\mathbf{K}\Delta\mathbf{r} = \lambda\mathbf{R}_{0,ext} - \mathbf{R}_{int} \quad (3.1)$$

where

$\mathbf{K}$	incremental system stiffness matrix
$\mathbf{R}_{0,ext}$	external load vector with $\lambda = 1$
$\mathbf{R}_{int}$	internal system load vector
$\Delta\mathbf{r}$	incremental system displacement vector (to be found)
$\lambda$	load parameter (to be found)

If the external loading is non conservative then  $\mathbf{R}_{0,ext}$  is a function of the current configuration of the structure and must be updated each time the geometry is updated. For conservative external loading  $\mathbf{R}_{0,ext}$  is constant.

One of the degrees of freedom is specified and defined as a so called governing degree of freedom. Without loss of generality the first degree of freedom is the governing degree of freedom and set equal to a predefined value  $\Delta r_1$ . The value of  $\Delta r_1$  may vary from load increment to load increment but it may not change sign during the simulation. The task is now to find the value of  $\lambda$  that will give  $\Delta r_1$  as the solution of the equation system.

The equation system from Eq. 3.1 may then be written:

$$\begin{bmatrix} K_{11} & \mathbf{K}_{12} \\ \mathbf{K}_{21} & \mathbf{K}_{22} \end{bmatrix} \begin{bmatrix} \Delta r_1 \\ \Delta \mathbf{r}_2 \end{bmatrix} = \lambda \begin{bmatrix} R_{01,ext} \\ \mathbf{R}_{02,ext} \end{bmatrix} - \begin{bmatrix} R_{1,int} \\ \mathbf{R}_{2,int} \end{bmatrix} \quad (3.2)$$

The second part of the equation system from Eq. 3.1 gives:

$$\Delta \mathbf{r}_2 = \mathbf{K}_{22}^{-1} (\lambda \mathbf{R}_{02,ext} - \mathbf{R}_{2,int} - \mathbf{K}_{21} \Delta r_1) \quad (3.3)$$

The above expression for  $\Delta \mathbf{r}_2$  is inserted into the first part of the equation system and the result for the load parameter is:

$$\lambda = \frac{(\mathbf{K}_{12} \mathbf{K}_{22}^{-1} \mathbf{K}_{21} - K_{11}) \Delta r_1 + (\mathbf{K}_{12} \mathbf{K}_{22}^{-1} \mathbf{R}_{2,int} - R_{1,int})}{\mathbf{K}_{12} \mathbf{K}_{22}^{-1} \mathbf{R}_{02,ext} - R_{01,ext}} \quad (3.4)$$

This value of  $\lambda$  is now inserted into the expression for  $\Delta \mathbf{r}_2$ . Finally, the total displacement vector is updated according to:

$$r_1 = r_1 + \Delta r_1 \quad (3.5)$$

$$\mathbf{r}_2 = \mathbf{r}_2 + \Delta \mathbf{r}_2 \quad (3.6)$$

### 3.3 Equilibrium iterations

There should be no corrections to  $\Delta r_1$  during the equilibrium iterations. Hence, the updated value of the load parameter ( $\lambda$ ) and the corrections to  $\Delta \mathbf{r}_2$  are:

$$\lambda = \frac{\mathbf{K}_{12} \mathbf{K}_{22}^{-1} \mathbf{R}_{2,int} - R_{1,int}}{\mathbf{K}_{12} \mathbf{K}_{22}^{-1} \mathbf{R}_{02,ext} - R_{01,ext}} \quad (3.7)$$

$$\Delta \mathbf{r}_2 = \mathbf{K}_{22}^{-1} (\lambda \mathbf{R}_{02,ext} - \mathbf{R}_{2,int}) \quad (3.8)$$

$$\mathbf{r}_2 = \mathbf{r}_2 + \Delta \mathbf{r}_2 \quad (3.9)$$

$\mathbf{R}_{int}$  is updated during the equilibrium iterations and when the external loading is non conservative  $\mathbf{R}_{0,ext}$  is updated. In a pure Newton-Raphson iteration scheme  $\mathbf{K}$  is also updated at each iteration.

In a one-dimensional case as shown in Fig. 3.1, it follows that no iterations need to be taken.

### 3.4 How to avoid large load increments

The structural response in nonlinear geometrical and nonlinear material problems may be largely different in the linear elastic range and in the nonlinear range. It is therefore necessary to keep both the governing degree of freedom,  $\Delta r_1$ , and the increment in the load parameter,  $\Delta \lambda = \lambda^{II} - \lambda^I$ , within a predefined window as shown in Fig. 3.2.

Equilibrium is achieved at load parameter  $\lambda^I$  and the ratio of  $\Delta \lambda$  to  $\Delta r_I$  in the previous load increment is

$$s^I = \frac{\Delta \lambda^I}{\Delta r_1^I} \quad (3.10)$$

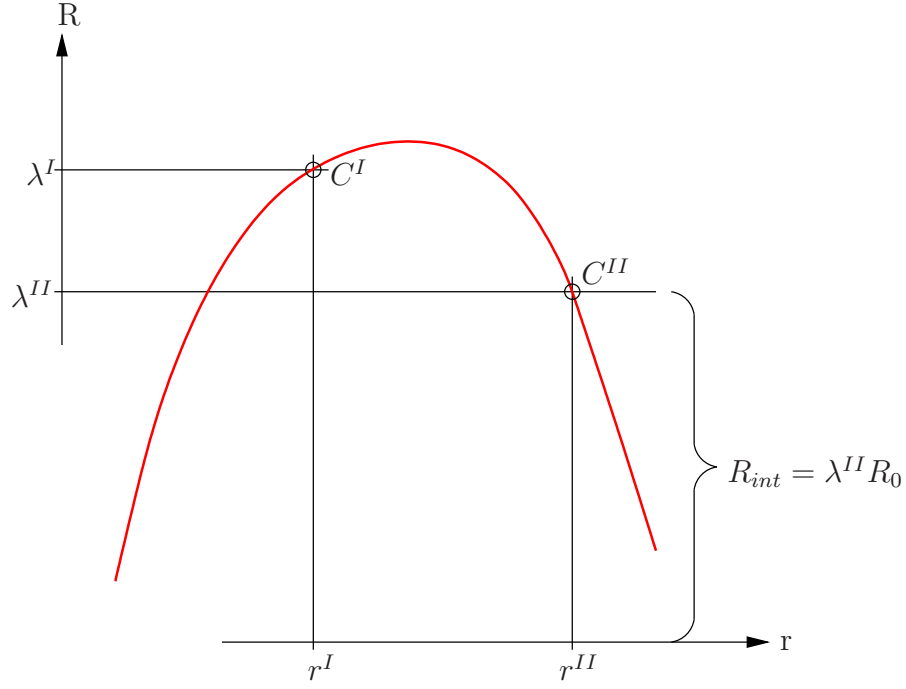


Figure 3.1: One-dimensional load-displacement curve

It is assumed that  $s^{II} \approx s^I$  and linear extrapolation will give the intersection point with the frame of the window. When the extrapolation line intersects with one of the two horizontal load level lines then the value of  $\Delta r_1$  will be smaller than  $(\Delta r_1)_{max}$ , otherwise  $\Delta r_1$  will be equal to  $(\Delta r_1)_{max}$ . Both  $(\Delta r_1)_{max}$  and  $\lambda_{max}$  should be input based on expected response of the structure. The quantity  $(\Delta r_1)_{max}$  may be multiplied by a scaling factor smaller than 1. This scaling factor may be found from the number of iteration on the previous increment

Which degree of freedom that should be the governing degree of freedom should also be carefully selected based on the expected response. The governing degree of freedom may be a nodal displacement or a rotation in a node and in a direction that will describe the nonlinear response.

The value of  $\Delta r_1$  for the first load increment may be set to a small value,  $\Delta r_{max}/20$ , to ensure linear elastic response for the first load increment.

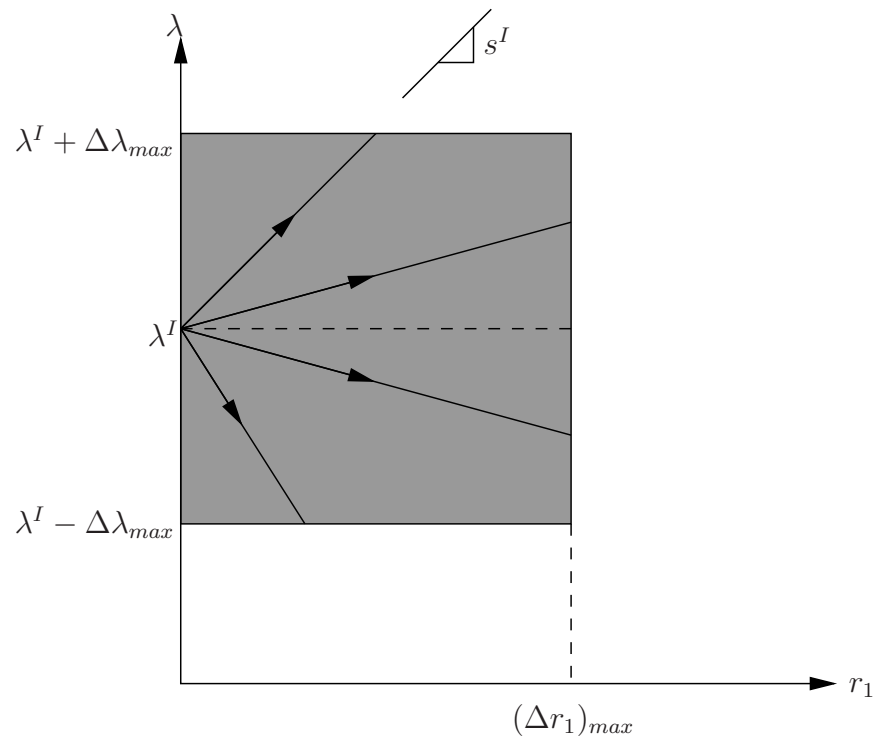


Figure 3.2: Avoid large increments

# Chapter 4

## Linear dependencies

Linear dependencies are used in  $\text{LINK}_{\text{pipe}}$  to handle geometrical discontinuities such as misalignment.

A coupling constrains a group of slave nodes to the translation and rotation of a master node. Since each slave node has a separate relationship with the master node, the coupling constraint can be considered as the combination of general master-slave constraints. These general constraints are described below.

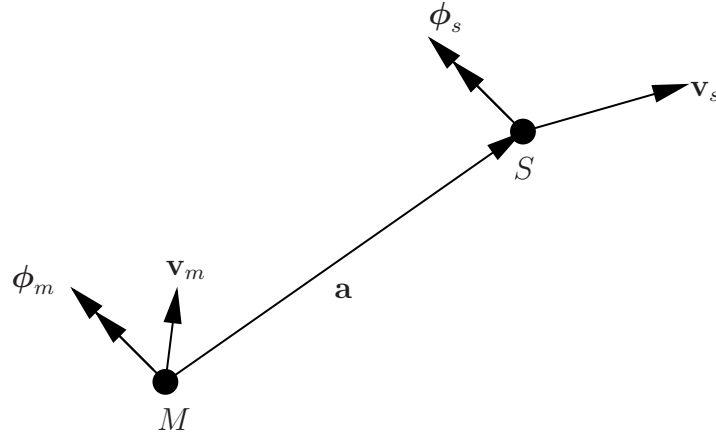


Figure 4.1: Linear dependencies

### 4.1 Rotations

The rotations in the master node will directly be reflected in the rotations in the slave nodes with the same magnitude as described in Eq. 4.1.

$$\phi_s = \phi_m \quad (4.1)$$



## 4.2 Translations

The additional internal node, described above, also reflects the motion of the slave node in the following manner. Let  $\mathbf{X}_m$  be the position of the master node and  $\mathbf{X}_s$  be the position of the slave node in the reference configuration. The reference configuration position of the slave node with respect to the master node is then

$$\mathbf{a} = \mathbf{X}_s - \mathbf{X}_m \quad (4.2)$$

In the current configuration, the position of the slave node is

$$\hat{\mathbf{x}}_s = \mathbf{x}_m + \hat{\mathbf{a}} \quad (4.3)$$

$$\hat{\mathbf{a}} = \boldsymbol{\phi}_m \times \mathbf{a} = \mathbf{A}(\mathbf{a})\boldsymbol{\phi}_m \quad (4.4)$$

where  $\mathbf{A}(\mathbf{a})$  is the rotation matrix expressed as

$$\mathbf{A}(\mathbf{a}) = \begin{bmatrix} 0 & a_3 & -a_2 \\ -a_3 & 0 & a_1 \\ a_2 & -a_1 & 0 \end{bmatrix} \quad (4.5)$$

The complete equation system for a linear dependency is then obtained as

$$\begin{bmatrix} v_1 \\ v_2 \\ v_3 \\ \phi_1 \\ \phi_2 \\ \phi_3 \end{bmatrix}_S = \begin{bmatrix} 1 & 0 & 0 & 0 & a_3 & -a_2 \\ 0 & 1 & 0 & -a_3 & 0 & a_1 \\ 0 & 0 & 1 & a_2 & -a_1 & 0 \\ 0 & 0 & 0 & 1 & 0 & 0 \\ 0 & 0 & 0 & 0 & 1 & 0 \\ 0 & 0 & 0 & 0 & 0 & 1 \end{bmatrix} \begin{bmatrix} v_1 \\ v_2 \\ v_3 \\ \phi_1 \\ \phi_2 \\ \phi_3 \end{bmatrix}_M \quad (4.6)$$

$$\begin{bmatrix} \mathbf{v}_s \\ \boldsymbol{\phi}_s \end{bmatrix} = \begin{bmatrix} \mathbf{I} & \mathbf{A} \\ \mathbf{0} & \mathbf{I} \end{bmatrix} \begin{bmatrix} \mathbf{v}_m \\ \boldsymbol{\phi}_m \end{bmatrix} \quad (4.7)$$

# Appendix A

## Connection between co-rotational degree of freedom and global degree of freedom

$$\begin{aligned}
 \begin{bmatrix} \delta_R \mathbf{u}_{d1} \\ \delta_R \boldsymbol{\theta}_{d1} \\ \delta_R \mathbf{u}_{d2} \\ \delta_R \boldsymbol{\theta}_{d2} \\ \vdots \\ \delta_R \mathbf{u}_{dN} \\ \delta_R \boldsymbol{\theta}_{dN} \end{bmatrix} &= \begin{bmatrix} \mathbf{I} & \mathbf{0} & \mathbf{0} & \mathbf{0} & \dots & \mathbf{0} & \mathbf{0} \\ \mathbf{0} & \mathbf{H}_1 & \mathbf{0} & \mathbf{0} & \dots & \mathbf{0} & \mathbf{0} \\ \mathbf{0} & \mathbf{0} & \mathbf{I} & \mathbf{0} & \dots & \mathbf{0} & \mathbf{0} \\ \mathbf{0} & \mathbf{0} & \mathbf{0} & \mathbf{H}_2 & \dots & \mathbf{0} & \mathbf{0} \\ \vdots & \vdots & \vdots & \vdots & \ddots & \vdots & \vdots \\ \mathbf{0} & \mathbf{0} & \mathbf{0} & \mathbf{0} & \dots & \mathbf{I} & \mathbf{0} \\ \mathbf{0} & \mathbf{0} & \mathbf{0} & \mathbf{0} & \dots & \mathbf{0} & \mathbf{H}_N \end{bmatrix} \cdot \left( \begin{bmatrix} \mathbf{P}_{11} & \mathbf{0} & \mathbf{P}_{12} & \mathbf{0} & \dots & \mathbf{P}_{1N} & \mathbf{0} \\ \mathbf{0} & \mathbf{I} & \mathbf{0} & \mathbf{0} & \dots & \mathbf{0} & \mathbf{0} \\ \mathbf{P}_{21} & \mathbf{0} & \mathbf{P}_{22} & \mathbf{0} & \dots & \mathbf{P}_{2N} & \mathbf{0} \\ \mathbf{0} & \mathbf{0} & \mathbf{0} & \mathbf{0} & \dots & \mathbf{0} & \mathbf{0} \\ \vdots & \vdots & \vdots & \vdots & \ddots & \vdots & \vdots \\ \mathbf{P}_{N1} & \mathbf{0} & \mathbf{P}_{N2} & \mathbf{0} & \dots & \mathbf{P}_{NN} & \mathbf{0} \\ \mathbf{0} & \mathbf{0} & \mathbf{0} & \mathbf{0} & \dots & \mathbf{0} & \mathbf{I} \end{bmatrix} \right. \\
 &+ \left. \begin{bmatrix} \text{Spin}(\mathbf{x}_1^n) \mathbf{G}_1 & \text{Spin}(\mathbf{x}_1^n) \mathbf{G}_2 & \dots & \text{Spin}(\mathbf{x}_1^n) \mathbf{G}_N \\ -\mathbf{G}_1 & -\mathbf{G}_2 & \dots & -\mathbf{G}_N \\ \text{Spin}(\mathbf{x}_2^n) \mathbf{G}_1 & \text{Spin}(\mathbf{x}_2^n) \mathbf{G}_2 & \dots & \text{Spin}(\mathbf{x}_2^n) \mathbf{G}_N \\ -\mathbf{G}_1 & -\mathbf{G}_2 & \dots & -\mathbf{G}_N \\ \vdots & \vdots & \ddots & \vdots \\ \text{Spin}(\mathbf{x}_N^n) \mathbf{G}_1 & \text{Spin}(\mathbf{x}_N^n) \mathbf{G}_2 & \dots & \text{Spin}(\mathbf{x}_N^n) \mathbf{G}_N \\ -\mathbf{G}_1 & -\mathbf{G}_2 & \dots & -\mathbf{G}_N \end{bmatrix} \right) \delta \begin{bmatrix} \mathbf{u}_{d1} \\ \boldsymbol{\theta}_{d1} \\ \mathbf{u}_{d2} \\ \boldsymbol{\theta}_{d2} \\ \vdots \\ \mathbf{u}_{dN} \\ \boldsymbol{\theta}_{dN} \end{bmatrix} \quad (\text{A.1})
 \end{aligned}$$

$$\mathbf{P}_{ab} = \left( \delta_{ab} - \frac{1}{N} \right) \mathbf{I} = \begin{cases} \mathbf{I} - \frac{1}{N} \mathbf{I} & \text{for } a = b \\ -\frac{1}{N} \mathbf{I} & \text{for } a \neq b \end{cases} \quad (\text{A.2})$$

With further simplification,  $\delta_R \mathbf{v}_d$  may be written as

$$\delta_R \mathbf{v}_d = \begin{bmatrix} \mathbf{H}_{11} & \mathbf{0} & \dots & \mathbf{0} \\ \mathbf{0} & \mathbf{H}_{22} & \dots & \mathbf{0} \\ \vdots & \vdots & \ddots & \vdots \\ \mathbf{0} & \mathbf{0} & \dots & \mathbf{H}_{NN} \end{bmatrix} \cdot \left( \begin{bmatrix} \mathbf{I} & \mathbf{0} & \dots & \mathbf{0} \\ \mathbf{0} & \mathbf{I} & \dots & \mathbf{0} \\ \vdots & \vdots & \ddots & \vdots \\ \mathbf{0} & \mathbf{0} & \dots & \mathbf{I} \end{bmatrix} \right) \quad (\text{A.3})$$

$$- \begin{bmatrix} \mathbf{P}_{T_{11}} & \mathbf{P}_{T_{12}} & \dots & \mathbf{P}_{T_{1N}} \\ \mathbf{P}_{T_{21}} & \mathbf{P}_{T_{22}} & \dots & \mathbf{P}_{T_{2N}} \\ \vdots & \vdots & \ddots & \vdots \\ \mathbf{P}_{T_{N1}} & \mathbf{P}_{T_{N2}} & \dots & \mathbf{P}_{T_{NN}} \end{bmatrix} - \begin{bmatrix} \mathbf{S}_1 \\ \mathbf{I} \\ \mathbf{S}_2 \\ \mathbf{I} \\ \vdots \\ \mathbf{S}_N \\ \mathbf{I} \end{bmatrix} \left[ \mathbf{G}_1 \quad \mathbf{G}_2 \quad \dots \quad \mathbf{G}_N \right] \delta \mathbf{v} \quad (\text{A.4})$$

(A.5)

$$= \mathbf{H}(\mathbf{I} - \mathbf{P}_T - \mathbf{P}_R) \delta \mathbf{v} = \mathbf{H} \mathbf{P} \delta \mathbf{v} \quad (\text{A.6})$$

$$\mathbf{P}_{Tab} = \begin{bmatrix} \frac{1}{N} \mathbf{I} & \mathbf{0} \\ \mathbf{0} & \mathbf{0} \end{bmatrix} \quad \text{and} \quad \mathbf{H}_{aa} = \begin{bmatrix} \mathbf{I} & \mathbf{0} \\ \mathbf{0} & \mathbf{H}_a \end{bmatrix} \quad (\text{A.7})$$

$$\mathbf{S}_a = \begin{bmatrix} -\mathbf{Spin}(\mathbf{x}_a^n) \\ \mathbf{I} \end{bmatrix} \quad (\text{A.8})$$

# Appendix B

## Consistent geometrical tangent stiffness contributions

The rotational geometric stiffness reads

$$\mathbf{E}^T \delta \mathbf{T}^T \tilde{\mathbf{P}}^T \tilde{\mathbf{H}}^T \tilde{\mathbf{f}}_e = \mathbf{E}^T \delta \mathbf{T}^T \tilde{\mathbf{f}} = \mathbf{E}^T \begin{bmatrix} \delta \mathbf{T}_n^T & \mathbf{0} & \dots & \mathbf{0} & \mathbf{0} \\ \mathbf{0} & \delta \mathbf{T}_n^T & \dots & \mathbf{0} & \mathbf{0} \\ \vdots & \vdots & \ddots & \vdots & \vdots \\ \mathbf{0} & \mathbf{0} & \dots & \delta \mathbf{T}_n^T & \mathbf{0} \\ \mathbf{0} & \mathbf{0} & \dots & \mathbf{0} & \delta \mathbf{T}_n^T \end{bmatrix} \begin{bmatrix} \tilde{\mathbf{n}}_1 \\ \tilde{\mathbf{m}}_1 \\ \vdots \\ \tilde{\mathbf{n}}_N \\ \tilde{\mathbf{m}}_N \end{bmatrix} \quad (\text{B.1})$$

$$= \mathbf{E}^T \begin{bmatrix} \delta \mathbf{T}_n^T \tilde{\mathbf{n}}_1 \\ \delta \mathbf{T}_n^T \tilde{\mathbf{m}}_1 \\ \vdots \\ \delta \mathbf{T}_n^T \tilde{\mathbf{n}}_N \\ \delta \mathbf{T}_n^T \tilde{\mathbf{m}}_N \end{bmatrix} = \mathbf{E}^T \begin{bmatrix} \mathbf{T}_n^T \text{Spin}(\delta \tilde{\omega}_r) \tilde{\mathbf{n}}_1 \\ \mathbf{T}_n^T \text{Spin}(\delta \tilde{\omega}_r) \tilde{\mathbf{m}}_1 \\ \vdots \\ \mathbf{T}_n^T \text{Spin}(\delta \tilde{\omega}_r) \tilde{\mathbf{n}}_N \\ \mathbf{T}_n^T \text{Spin}(\delta \tilde{\omega}_r) \tilde{\mathbf{m}}_N \end{bmatrix} \quad (\text{B.2})$$

$$= \mathbf{E}^T \begin{bmatrix} -\mathbf{T}_n^T \text{Spin}(\tilde{\mathbf{n}}_1) \delta \tilde{\omega}_r \\ -\mathbf{T}_n^T \text{Spin}(\tilde{\mathbf{m}}_1) \delta \tilde{\omega}_r \\ \vdots \\ -\mathbf{T}_n^T \text{Spin}(\tilde{\mathbf{n}}_N) \delta \tilde{\omega}_r \\ -\mathbf{T}_n^T \text{Spin}(\tilde{\mathbf{m}}_N) \delta \tilde{\omega}_r \end{bmatrix} = -\mathbf{E}^T \mathbf{T}^T \begin{bmatrix} \text{Spin}(\tilde{\mathbf{n}}_1) \\ \text{Spin}(\tilde{\mathbf{m}}_1) \\ \vdots \\ \text{Spin}(\tilde{\mathbf{n}}_N) \\ \text{Spin}(\tilde{\mathbf{m}}_N) \end{bmatrix} \delta \tilde{\omega}_r \quad (\text{B.3})$$

(B.4)

$$= -\mathbf{E}^T \mathbf{T}^T \tilde{\mathbf{F}}_{nm} \delta \tilde{\omega}_r = -\mathbf{E}^T \mathbf{T}^T \tilde{\mathbf{F}}_{nm} \tilde{\mathbf{G}} \mathbf{T} \mathbf{E} \delta \dot{\mathbf{v}} = \mathbf{K}_{GR} \delta \dot{\mathbf{v}} \quad (\text{B.5})$$

The following relationships were used in this derivation:

$$\delta \mathbf{T}_n^T = \mathbf{T}_n^T \text{Spin}(\delta \tilde{\omega}_r) \quad \text{Spin}(\delta \tilde{\omega}_r) \tilde{\mathbf{n}}_a = -\text{Spin}(\tilde{\mathbf{n}}_a) \delta \tilde{\omega}_r \quad \delta \tilde{\omega}_r = \tilde{\mathbf{G}} \delta \dot{\mathbf{v}} \quad (\text{B.6})$$

$$\tilde{\mathbf{F}}_{nm} = \begin{bmatrix} \text{Spin}(\tilde{\mathbf{n}}_1) \\ \text{Spin}(\tilde{\mathbf{m}}_1) \\ \vdots \\ \text{Spin}(\tilde{\mathbf{n}}_N) \\ \text{Spin}(\tilde{\mathbf{m}}_N) \end{bmatrix} \quad \text{and} \quad \tilde{\mathbf{f}} = \begin{bmatrix} \tilde{\mathbf{n}}_1 \\ \tilde{\mathbf{m}}_1 \\ \vdots \\ \tilde{\mathbf{n}}_N \\ \tilde{\mathbf{m}}_N \end{bmatrix} = \tilde{\mathbf{P}}^T \tilde{\mathbf{H}}^T \tilde{\mathbf{f}}_e \quad (\text{B.7})$$

The equilibrium projection geometric term is written

$$\begin{aligned}
 \mathbf{E}^T \mathbf{T}^T \delta_R \tilde{\mathbf{P}}^T \tilde{\mathbf{H}}^T \tilde{\mathbf{f}}_e &= \mathbf{E}^T \mathbf{T}^T \left( \delta_R \mathbf{I} - \delta_R \tilde{\mathbf{P}}_T^T - \delta_R \tilde{\mathbf{P}}_R^T \right) \tilde{\mathbf{H}}^T \tilde{\mathbf{f}}_e \\
 &= \mathbf{E}^T \mathbf{T}^T \left( -\delta_R \tilde{\mathbf{P}}_R^T \right) \tilde{\mathbf{H}}^T \tilde{\mathbf{f}}_e \\
 &= -\mathbf{E}^T \mathbf{T}^T \left( \delta_R \tilde{\mathbf{G}}^T \tilde{\mathbf{S}}^T + \tilde{\mathbf{G}}^T \delta_R \tilde{\mathbf{S}}^T \right) \tilde{\mathbf{H}}^T \tilde{\mathbf{f}}_e \\
 &= -\mathbf{E}^T \mathbf{T}^T \left( \delta_R \tilde{\mathbf{G}}^T \tilde{\mathbf{S}}^T + \tilde{\mathbf{G}}^T \delta_R \tilde{\mathbf{S}}^T \right) \left( \tilde{\mathbf{f}}_b + \tilde{\mathbf{f}}_u \right) \\
 &= -\mathbf{E}^T \mathbf{T}^T \left( \left( \delta_R \tilde{\mathbf{G}}^T \tilde{\mathbf{S}}^T + \tilde{\mathbf{G}}^T \delta_R \tilde{\mathbf{S}}^T \right) \tilde{\mathbf{f}}_b + \left( \delta_R \tilde{\mathbf{G}}^T \tilde{\mathbf{S}}^T + \tilde{\mathbf{G}}^T \delta_R \tilde{\mathbf{S}}^T \right) \tilde{\mathbf{f}}_u \right) \\
 &= -\mathbf{E}^T \mathbf{T}^T \left( \tilde{\mathbf{G}}^T \delta_R \tilde{\mathbf{S}}^T \tilde{\mathbf{f}}_b + \delta_R \tilde{\mathbf{P}}^T \tilde{\mathbf{f}}_u \right) \tag{B.8}
 \end{aligned}$$

$\tilde{\mathbf{S}}^T$  represents the rigid body rotation vectors, causing  $\tilde{\mathbf{S}}^T \tilde{\mathbf{f}}_b = \mathbf{0}$ , because balanced forces do not produce any work on a structure during rigid body displacement or rotation. Furthermore,  $\delta \tilde{\mathbf{P}}^T \tilde{\mathbf{f}}_u$  can be neglected because it will be very small when  $C_{0n}$  and  $C_n$  are close. Eq. B.8 reduces to

$$\begin{aligned}
 \mathbf{E}^T \mathbf{T}^T \delta \tilde{\mathbf{P}}^T \tilde{\mathbf{H}}^T \tilde{\mathbf{f}}_e &= -\mathbf{E}^T \mathbf{T}^T \tilde{\mathbf{G}}^T \delta \tilde{\mathbf{S}}^T \tilde{\mathbf{f}}_b \\
 &= -\mathbf{E}^T \mathbf{T}^T \tilde{\mathbf{G}}^T \sum_{a=1}^N \left[ \mathbf{Spin}(\delta_R \tilde{\mathbf{x}}_a^n) \quad \mathbf{0} \right] \begin{bmatrix} \tilde{\mathbf{n}}_a \\ \tilde{\mathbf{m}}_a \end{bmatrix} \\
 &= -\mathbf{E}^T \mathbf{T}^T \tilde{\mathbf{G}}^T \sum_{a=1}^N \mathbf{Spin}(\delta_R \tilde{\mathbf{x}}_a^n) \tilde{\mathbf{n}}_a \\
 &= \mathbf{E}^T \mathbf{T}^T \tilde{\mathbf{G}}^T \sum_{a=1}^N \mathbf{Spin}(\tilde{\mathbf{n}}_a) \delta_R \tilde{\mathbf{x}}_a^n \tag{B.9}
 \end{aligned}$$

$$= \mathbf{E}^T \mathbf{T}^T \tilde{\mathbf{G}}^T \sum_{a=1}^N \left[ \mathbf{Spin}(\tilde{\mathbf{n}}_a) \quad \mathbf{0} \right] \begin{bmatrix} \delta_R \tilde{\mathbf{u}}_{da} \\ \delta_R \tilde{\boldsymbol{\omega}}_{da} \end{bmatrix} \tag{B.10}$$

$$= -\mathbf{E}^T \mathbf{T}^T \tilde{\mathbf{G}}^T \tilde{\mathbf{F}}_n^T \delta_R \tilde{\mathbf{v}}_d = -\mathbf{E}^T \mathbf{T}^T \tilde{\mathbf{G}}^T \tilde{\mathbf{F}}_n^T \tilde{\mathbf{P}}^T \mathbf{E} \delta \dot{\mathbf{v}} = \mathbf{K}_{GP} \delta \dot{\mathbf{v}} \tag{B.11}$$

where

$$\tilde{\mathbf{F}}_n = \begin{bmatrix} \mathbf{Spin}(\tilde{\mathbf{n}}_1) \\ \mathbf{0} \\ \vdots \\ \mathbf{Spin}(\tilde{\mathbf{n}}_N) \\ \mathbf{0} \end{bmatrix} \quad \text{and} \quad \tilde{\mathbf{f}}_b = \begin{bmatrix} \tilde{\mathbf{n}}_1 \\ \tilde{\mathbf{m}}_1 \\ \vdots \\ \tilde{\mathbf{n}}_N \\ \tilde{\mathbf{m}}_N \end{bmatrix} = \tilde{\mathbf{P}}^T \tilde{\mathbf{H}}^T \tilde{\mathbf{f}}_e \tag{B.12}$$

The moment correction term is given by

$$\mathbf{E}^T \mathbf{T}^T \tilde{\mathbf{P}}^T \delta_R \tilde{\mathbf{H}}^T \tilde{\mathbf{f}}_e = \mathbf{E}^T \mathbf{T}^T \tilde{\mathbf{P}}^T \begin{bmatrix} \mathbf{0} & \mathbf{0} & \dots & \mathbf{0} & \mathbf{0} \\ \mathbf{0} & \delta_R \tilde{\mathbf{H}}_1^T & \dots & \mathbf{0} & \mathbf{0} \\ \vdots & \vdots & \ddots & \vdots & \vdots \\ \mathbf{0} & \mathbf{0} & \dots & \mathbf{0} & \mathbf{0} \\ \mathbf{0} & \mathbf{0} & \dots & \mathbf{0} & \delta_R \tilde{\mathbf{H}}_N^T \end{bmatrix} \begin{bmatrix} \tilde{\mathbf{n}}_1 \\ \tilde{\mathbf{m}}_1 \\ \vdots \\ \tilde{\mathbf{n}}_N \\ \tilde{\mathbf{m}}_N \end{bmatrix} \quad (\text{B.13})$$

$$= \mathbf{E}^T \mathbf{T}^T \tilde{\mathbf{P}}^T \begin{bmatrix} \mathbf{0} \\ \delta_R \tilde{\mathbf{H}}_1^T \tilde{\mathbf{m}}_1 \\ \vdots \\ \mathbf{0} \\ \delta_R \tilde{\mathbf{H}}_N^T \tilde{\mathbf{m}}_N \end{bmatrix} = \mathbf{E}^T \mathbf{T}^T \tilde{\mathbf{P}}^T \begin{bmatrix} \mathbf{0} \\ \tilde{\mathbf{M}}_1 \delta_R \tilde{\boldsymbol{\omega}}_{d1} \\ \vdots \\ \mathbf{0} \\ \tilde{\mathbf{M}}_N \delta_R \tilde{\boldsymbol{\omega}}_{dN} \end{bmatrix} \quad (\text{B.14})$$

$$(\text{B.15})$$

$$= \mathbf{E}^T \mathbf{T}^T \tilde{\mathbf{P}}^T \tilde{\mathbf{M}} \tilde{\mathbf{P}}^T \mathbf{E} \delta \dot{\mathbf{v}} = \mathbf{K}_{GM} \delta \dot{\mathbf{v}} \quad (\text{B.16})$$

where

$$\tilde{\mathbf{M}} = \begin{bmatrix} \mathbf{0} & \mathbf{0} & \dots & \mathbf{0} & \mathbf{0} \\ \mathbf{0} & \tilde{\mathbf{M}}_1 & \dots & \mathbf{0} & \mathbf{0} \\ \vdots & \vdots & \ddots & \vdots & \vdots \\ \mathbf{0} & \mathbf{0} & \dots & \mathbf{0} & \mathbf{0} \\ \mathbf{0} & \mathbf{0} & \dots & \mathbf{0} & \tilde{\mathbf{M}}_N \end{bmatrix} \quad (\text{B.17})$$

# Bibliography

- [1] R. A. Ainsworth and N. P. O'Dowd. A framework for including constraint effects in the failure assessment diagram approach for fracture assessment. *In: Proceedings of ASME Pressure Vessels and Piping Conference, PVP-vol.287/MD-vol. 47*, 1994.
- [2] T. L. Anderson. *Fracture mechanics - Fundamentals and Applications*. Taylor and Francis, 2005. ISBN: 978-0-8493-1656-2.
- [3] E. Berg, K. Holthe, and B. Skallerud. Cyclic plasticity modelling for andes thin shell and line-spring finite elements. *International Journal of Applied Mechanics*, 1(1):201–232, 2009.
- [4] E. Berg, B. Skallerud, and C. Thaulow. Two-parameter fracture mechanics and circumferential crack growth in surface cracked pipelines using line-spring elements. *Engineering Fracture Mechanics*, 75:17–30, 2008.
- [5] E. Berg, B. Skallerud, C. Thaulow, and K. Holthe. Using constraint correction to ductile crack growth in surface cracked shell-structures. *In proceedings: MekIT'05 Computational Mechanics, Trondheim, Norway. ISBN: 82-519-2052-3.*, pages 75–85, 2005.
- [6] P. G. Bergan and C. A. Felippa. A triangular membrane element with rotational degrees of freedom. *Computer Methods in Applied Mechanics and Engineering*, 50(1):25–69, 1985.
- [7] C. Betegon and J. W. Hancock. Two parameter characterization of elastic-plastic crack-tip fields. *Journal of Applied Mechanics*, 58:104–110, 1991.
- [8] British Standard. BS7910:1999: Incorporating Amendment No. 1. Guide on methods for assessing the acceptability of flaws in metallic structures. *British Standards Institute*, 2000. Skriv inn tekst her.
- [9] British Standard. BS7910:2005 Guide on methods for assessing the acceptability of flaws in metallic structures. *British Standards Institution*, 2007.
- [10] M. A. Crisfield. *Non-linear finite element analysis of solids and structures: Advanced topics*, volume 2. John Wiley & Sons Ltd., 1997. ISBN: 0-471-95649-X.
- [11] Z. Z. Du and J. W. Hancock. The effect of non-singular stresses on crack-tip constraint. *Journal of the Mechanics and Physics of Solids*, 39:555–567, 1991.
- [12] C. A. Felippa and C. Militello. Membrane triangles with corner drilling freedoms: II. The ANDES element. *Finite Elements in Analysis and Design*, 12:189–201, 1992.
- [13] Center for Composite Materials. User's guide for the program cmap - composite materials analysis of plates.

- [14] B. Gross and O. L. Sawley. Stress intensity factors for single edge notch specimens in bending or combined bending and tension by boundary collocation of a stress function. *NASA Technical Note D-2603*, 1965.
- [15] J. W. Hancock, W. G. Reuter, and D. M. Parks. Constraint and toughness parametrized by: T-stress. *American Society for Testing and Materials, Philadelphia*, 1171:21–40, 1993.
- [16] D. E. Hauf, D. M. Parks, and H. Lee. A modified effective crack-length formulation in elastic-plastic fracture mechanics. *Mechanics of Materials*, 20:273–289, 1995.
- [17] B. Haugen. *Buckling and stability problems for thin shell structures using high performance finite elements*. PhD thesis, Department of Aerospace Engineering Sciences, University of Colorado, Boulder, Colorado, USA, 1994.
- [18] A. Hrennikoff. Solution of problems of elasticity by a framework method. *Journal of Applied Mechanics*, 8:169–175, 1941.
- [19] Ibrahimbegovic A. and Frey F. Stress resultant elasto-plastic analysis of plates and shallow shells. *In proceedings: COMPLAS-3, Barcelona, Spain*, pages 2047–2059, 1992.
- [20] G. R. Irwin. Plastic zone near a crack and fracture toughness. *In: Proceedings of Sagamore Research Conference, Syracuse, NY, USA*, 4:63–78, 1961.
- [21] K. R. Jayadevan, E. Berg, C. Thaulow, E. Østby, and B. Skallerud. Numerical investigation of ductile tearing in surface cracked pipes using line-springs. *International Journal of Solids and Structures*, 43:2378–2397, 2006.
- [22] K. R. Jayadevan, C. Thaulow, E. Østby, E. Berg, B. Skallerud, K. Holthe, and B. Nyhus. Structural integrity of pipelines: T-stress by line-spring. *Fatigue and Fracture of Engineering Materials and Structures*, 28:467–488, 2005.
- [23] S. G. Larsson and A. J. Carlsson. Influence of non-singular stress terms and specimen geometry on small-scale yielding at crack tips in elastic-plastic materials. *Journal of the Mechanics and Physics of Solids*, 21:263–277, 1973.
- [24] H. Lee and D. M. Parks. Enhanced elastic-plastic line-spring finite element. *International Journal of Solids and Structures*, 32(16):2393–2418, 1995.
- [25] G. Masing. Eigenspannungen und Verfestigung beim Messing. *In proceedings: The 2nd International Congress for Applied Mechanics, Zürich, Switzerland*, pages 332–335, 1926.
- [26] H. Matthies. A decomposition method for integration of elastic-plastic rate problem. *International Journal for Numerical Methods in Engineering*, 28:1–11, 1989.
- [27] H. H. Michels. Abscissas and Weight Coefficients for Lobatto Quadrature. *Mathematics of Computation*, 17(83):237–244, 1963.
- [28] C. Militello. *Application of parametrized variational principles to the finite element method*. PhD thesis, Department of Aerospace Engineering Sciences, University of Colorado, Boulder, Colorado, USA, 1991.
- [29] J. C. Nour-Omid and C. C. Rankin. Finite rotation analysis and consistent linearization using projectors. *Computer Methods in Applied Mechanics and Engineering*, 93:353–384, 1991.



- [30] M. K. Nygård. *The free formulation for nonlinear finite elements with applications to shells*. PhD thesis, Div. of Structural Mechanics, Norwegian Institute of Technology, Trondheim, Norway, 1986.
- [31] B. Nyhus, Z.L. Zhang, and C. Thaulow. Normalisation of material crack resistance curves by the T-stress. *Proceedings of the 14th European Conference of Fracture, Poland*, 2002.
- [32] N. P. O'Dowd and C. F. Shih. Two-parameter fracture mechanics theory and applications. *American Society for Testing and Materials, Philadelphia*, 24(1207):21–47, 1994.
- [33] K. C. Park and G. M. Stanley. A curved  $C^0$  shell element based on assumed natural-coordinate strains. *Journal of Applied Mechanics*, 53:278–290, 1986.
- [34] D. M. Parks. The inelastic line-spring: estimates of elastic-plastic fracture mechanics parameters for surface cracked plates and shells. *Journal of Pressure Vessel Technology*, 103:246–254, 1981.
- [35] J.R. Rice. The line spring model for surface flaws. *Swedlow, J.L. (Ed.), The Surface Crack: Physical Problems and Computational Solutions. American Society of Mechanical Engineers, New York*, pages 171–185, 1972.
- [36] J.R. Rice and N. Levy. The part-through surface crack in an elastic plate. *Journal of Applied Mechanics*, 39:185–194, 1972.
- [37] A. Sandvik, E. Østby, and C. Thaulow. A probabilistic fracture mechanics model including 3D ductile tearing of bi-axially loaded pipes with surface cracks. *Accepted by Engineering Fracture Mechanics*, 2007.
- [38] T.L. Sham. The determination of the elastic  $T$ -stress using higher order weight functions. *International Journal of Fracture*, 48:81–102, 1991.
- [39] J. C. Simo. A finite strain beam formulation. the three dimensional dynamic problem. part i. *Computer Methods in Applied Mechanics and Engineering*, 49:55–70, 1985.
- [40] J.C. Simo and T.J.R. Hughes. *Computational Inelasticity*. Springer-Verlag, New York, Inc., 2000. ISBN: 0-387-97520-9.
- [41] B. Skallerud. A mixed mode I/II inelastic line spring. *International Journal of Solids and Structures*, 33(28):4143–4166, 1996.
- [42] B. Skallerud. Numerical analysis of cracked inelastic shells with large displacements or mixed mode loading. *International Journal of Solids and Structures*, 36:2259–2283, 1998.
- [43] B. Skallerud and B. Haugen. Collapse of thin shell structures - stress resultant plasticity modelling within a co-rotated ANDES finite element formulation. *International Journal for Numerical Methods in Engineering*, 46:1961–1986, 1999.
- [44] B. Skallerud, K. Holthe, and B. Haugen. Thin shell and surface crack finite elements for simulation of combined failure modes. *Computer Methods in Applied Mechanics and Engineering*, 194(21-24):2619–2640, 2005.
- [45] M. L. Szwabowicz. Variational formulation in the geometrically non-linear thin elastic shell theory. *International Journal of Solids and Structures*, 22:1161–1175, 1986.

- 
- [46] H. Tada, P.C. Paris, and G.R. Irwin. The stress analysis of cracks handbook. *Fracture Proof Design, Saint Louis, Montana, USA*, 1985.
  - [47] C. Thaulow, E. Østby, B. Nyhus, Z. L. Zhang, and B. Skallerud. Constraint correction of high strength steel. selection of test specimens and application of direct calculations. *Engineering Fracture Mechanics*, 71:2417–2433, 2004.
  - [48] Y.-Y. Wang and D. M. Parks. Evaluation of the elastic T-stress in surface-cracked plates using the line-spring method. *International Journal of Fracture*, 56:25–40, 1992.
  - [49] C. S. White and D. M. Parks. Elastic-plastic line-spring finite elements for surface-cracked plates and shells. *Journal of Pressure Vessel Technology*, 104:287–292, 1982.